IACMI/R003-2019/3.11

Thermoplastic Composite Parts Manufacturing Enabling High Volumes, Low Cost, Reduced Weight with Design Flexibility – Phase 2

Author: Lee Silverman
Michael Bogdanor
Robert Davies

Date:

Final Technical Report
003-2019-3.11

Approved for Public Release.
Distribution is Unlimited.

The Institute for iacmi Advanced Composites Manufacturing Innovation
THE COMPOSITES INSTITUTE
U.S. DEPARTMENT OF ENERGY

Thermoplastic Composites Parts Manufacturing Enabling High Volumes, Low Cost, Reduced Weight with Design Flexibility – Phase 2

Principal Investigator: Lee Silverman

Organization: E.I. DuPont de Nemours and Company, Inc.

Address: Powder Mill Road, Building 323/306B, Wilmington, DE

Phone: (302) 695-4350

Email: lee.a.silverman@dupont.com

Co-authors:

- Michael Bodganor, Purdue University College of Engineering, Composites Manufacturing and Simulation Center, West Lafayette, Indiana, 47906
- Robert Davies, Fibrtec Inc., Atlanta, Texas, 75551
- Jacob Dickinson DuPont Company, DuPont Performance Materials, Wilmington, Delaware, 19803

Date Published: (October 2, 2019)

Prepared by:
Institute for Advanced Composites Manufacturing Innovation
Knoxville, TN 37932
Managed by Collaborative Composite Solutions, Inc.
For the
U.S. DEPARTMENT OF ENERGY
Under contract DE- EE0006926

Project Period:
(09/2017 – 02/2019)

Approved For Public Release

TABLE OF CONTENTS

1 LISTS

1.1 List of Acronyms

ADC	Automated Dynamics Corporation
AFP	Automated Fiber Placement
CF	Carbon Fiber
CFRP	Continuous Fiber Reinforced Polymer
COM	Cost of Manufacture
CPV	
DMA	
IACMI	Institute for Advanced Composites Manufacturing Innovation
LCA	Lower Control Arm
NNS	Near Net Shape
PA	Polyamide
PTFE	Polytetrafluoroethylene
RFF	Rapid Fabric Formation
UD	Unidirectional

1.2 List of Figures

1.3 List of Tables

1.4 List of Appendices

1.5 Acknowledgements

The information, data, or work presented herein was funded in part by the Office of Energy Efficiency and Renewable Energy (EERE), U.S. Department of Energy, under Award DE-EE0006926

The authors would like to acknowledge the work of many team members that made this work possible, from project guidance, to administration, to execution. This extended and talented team included:

DuPont: Doug Anton, Janet Sawgle, Mary Strzlecky, Mark Weinberg, Bryan Sauer, Tao Huang, Tim Harper, Ryan Martin, Charles Woodward, and Zachary Dilworth.

Fibrtec: Penelope Salmons

Ford Motor Company: Xiaoming Chen, David Wagner

Purdue: R. Byron Pipes, David Kim, Himal Agrawal, Nathan Sharp, and Joshua Dustin

IACMI: Dale Brosius, Lisa Fitzgerald, Erin Brophy, John Unser, and John Hopkins

Department of Energy: Kelly Visconti

Thank you all for your diligent and inspired efforts.

2 EXECUTIVE SUMMARY

The deliverable of this IACMI PHASE II project is an innovative thermoplastic composite parts manufacturing process that addressed some of the most challenging aspects for commercial adoption in high volume market applications with requisite design flexibility while lowering cost and weight. The collaborative 15-month joint effort built upon the collective collateral value that was validated in PHASE I, as well as the synergies of a cross- functional team members comprised & lead by DuPont, Fibrtec & Purdue. Specifically, Fibrtec's uniquely flexible coated tow (FibrFlex®) with DuPont's Rapid Fabric Formation (RFF) technology and a proprietary DuPont polyamide resin, were used to create near net shapes, while Purdue developed new simulation tools to predict the behavior of material system preforms in molding processes. These were ultimately deployed for the manufacturing with "informed" performance of industrially-interesting CFRP parts. Experiments, modeling, and simulations have shown that this process/materials combination offers advantages for producing lower cost continuous fiber reinforced polymer (CFRP) materials that drape well during molding while maintaining outstanding physical properties. This newly deployed process is ideally suitable for adoption in the automotive and other higher volume industries because of the associated cost savings due to reduction of waste and embodied energy. Furthermore, it overcomes the drawbacks of the prevalent two other typically deployed processes; the slow speed and expensive part formation associated with the usage of the stiff and brittle UD tapes, or the release of short conductive carbon fiber strands into the environment associated by the alternate layering of fiber woven fabric with resin film.

3 INTRODUCTION

Continuous carbon fiber composites can be divided into two broad classes based on their polymer matrix chemistries; thermosets and thermoplastics. Each material system has its strengths, and the system that is chosen for a specific use depends on the detailed requirements of the particular application being considered. For example, thermoset composites are capable of Class A surfaces but have limited shelf life, require refrigeration, are not readily recyclable, and can require an extended time in the mold to complete the polymerization process to the point where they are stiff enough to be unmolded. Thermoplastic composites, on the other hand, generally have rougher surfaces unless overmolded in a subsequent process step, but can be thermally stamped in high rate processes relative to thermoset molding. In addition, the thermoplastic stamping process is reminiscent of a metal stamping process with which the automotive industry is already quite comfortable.

Both composite systems have the unique combination of high strength and stiffness with low density, typical of continuous carbon fiber systems, which makes them ideal for reducing weight in vehicles, enabling among other things an increase in fuel efficiency. Their largest drawback, which is currently preventing wider commercial application, is a high cost relative to the weight saved. This high cost is due to both raw materials and fabrication. While the price of the carbon fiber itself is being addressed in separate IACMI projects, this program addresses the downstream fabrication cost of the composite parts.

There are several legacy manufacturing techniques for continuous carbon fiber based thermoplastic composite fabric preforms, again, each having its own strengths and weaknesses, three of which are depicted in Figure 1. In this Figure, black areas represent carbon fiber, blue is polymer, and white is void. As defined for the Figure, the x direction is in the plane of the Figure, while y is perpendicular to the plane of the Figure. The first technique is based on woven fabrics of carbon fiber tows, interleaving these fabrics with thermoplastic resin films as shown in Figure 1b, and subsequently heating and compressing the preforms into a well-consolidated composite. Materials aside, one of the biggest costs of this technique is in the weaving of the carbon fiber tows. The stiff carbon fibers can easily break during weaving, releasing short carbon fibers into the local environment. This conductive high aspect ratio debris can easily short out electrical equipment near the loom, and therefore the looms and nearby equipment need to be electrically isolated. Furthermore, the fiber properties also require that the looms be operated at relatively slow speeds, roughly one third the speed at which glass fiber-based fabric is made, adding additional capital related costs to the manufacturing process. This is also true for carbon fiber fabric co-woven with polymer filaments and combinations of woven carbon fiber and polymer powder. An additional potential drawback for processes based on woven fabric is the fabric's relative inability to conform to sharp corners and deep draws when molded. This occurs due to the "shear locking" of the fabric, leading to wrinkles and other fiber miss-orientation effects in the molded part.

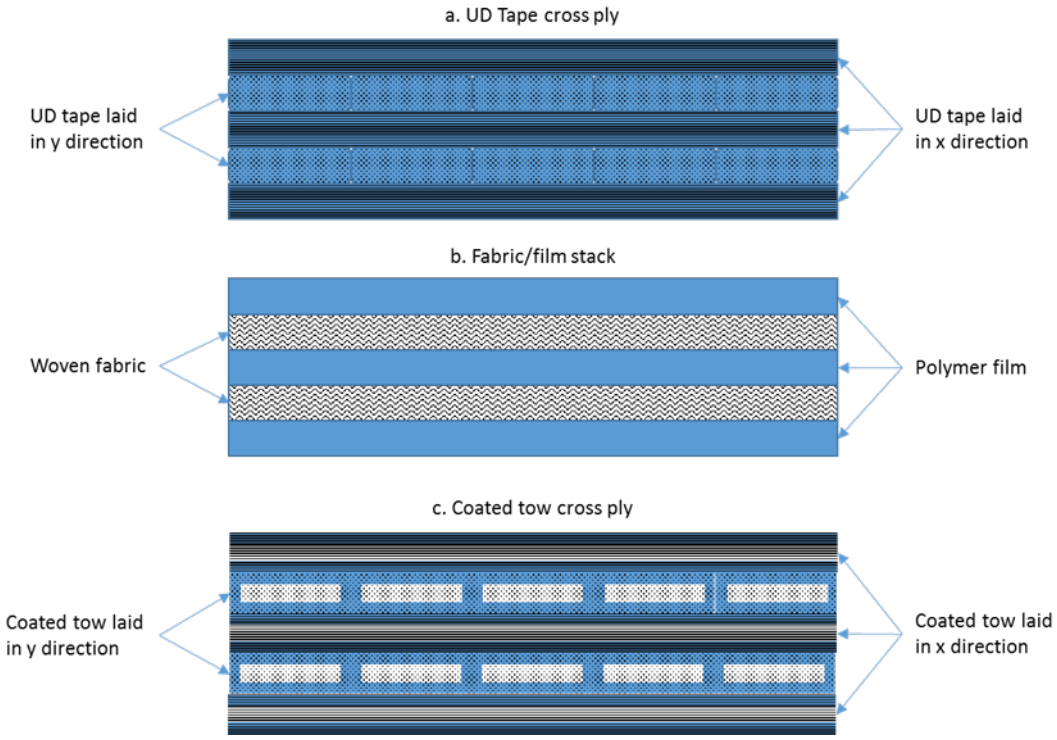

Figure 1. Schematic of preform cross-sections showing a) UD tapes, b) fabric/film stacks, and c) coated tow.

Weaving processes generally create rectangular fabrics from which the fabric layers required for the preforms must be cut. While this is acceptable for final composite parts that are substantially flat and rectangular in shape, it leads to significant trim waste when a non-rectangular part is desired. Since carbon fiber is the most expensive component of the fabricated composite part, the

discarded expensive fabric is reflected in the high cost of manufacture of the finished composite.

Another general technique for preform fabrication uses prefabricated low-void UD tape, as depicted in Figure 1a. These tapes are woven or placed and tacked to form a preform, which is then rapidly consolidated, perhaps via hot stamping into the final composite part in a heated press. A major issue with this process is the handling of the UD tapes because they are stiff and brittle, and therefore can fracture when bent to tight radii at room temperature. The stiffness makes fabric formation from tapes a slow and expensive process. It should not be lost on the reader that the tape fabrication process, usually by pultrusion, is slow with a low corresponding capital productivity.

The objective of this program was to reduce the cost of manufacture (COM) of carbon fiber CFRP composites by using a near net shape process (NNS) such as automated fiber placement (AFP) on a relatively inexpensive, partially impregnated, carbon fiber/polymer tow-preg, hereafter referred to as coated tow. The coated tows are easily manipulated, and the resulting pseudo-fabrics are easily draped and conform easily during molding without shear locking. With this strategy, it should be able to use the expensive carbon fiber only where it is required, reduce the carbon fiber waste by up to 30%, and create fiber preforms that predictably drape during compression prior to molding.

In addition, the embodied energy was studied by Brosius and Deo[2]. The report summarizing the findings is presented separately, and shows that the embodied energy was reduced by over 40 percent using this processing scheme.

The combination of these materials and process schemes will therefore lead to a decrease in cost for carbon fiber composite structures, making them more amenable for adoption in the automotive and other industries, reduce embodied energy, and directly lead to a creation of jobs in the industry.

Phase 1 of this program, completed in March of 2017 and reported on previously[3], presented the physical properties of the RFF non-crimp fabric and the consolidated parts made therefrom. These data were used to create models and simulations that validated that the drape would be superior to traditional twill fabrics, without sacrificing any of the mechanical properties of the finished part. In addition, a techno-economic analysis was performed to show that the reduction of waste carbon fiber would be responsible for up to a 30% cost savings over woven fabric-based processes.

Phase 2 of this program, reported here, is dedicated to the production and characterization of industrially-interesting parts made from the RFF, their characterization, and an estimate of the cost of the laydown system that would create the fabrics.

4 BACKGROUND

The project was broken into several steps, and culminated in the fabrication of parts that demonstrated the beneficial properties of an RFF process based on coated tow.

Over the course of this program, many things were learned that led to redirections of the program. For example, when originally designed, this program was targeted to produce parts in the form of lower control arms (LCAs), similar to those used in the Ford Fusion. The Ford Motor Company was part of the program and shared much information with the remainder of the team regarding the design and load characteristics of the LCA. After the characterization of consolidated RFF plaques, the physical space around the front wheel, i.e. the design envelope for the LCA, was used to create an LCA design. After topology optimization, the resulting LCA was only slightly less massive than the cast aluminum part that it was to replace. The two primary reasons for this are that the current aluminum part is very well optimized for the application, and that the design space is too constrained to allow efficient use of the carbon fiber composite. As a result, the CFRP part became a "piece of black metal", i.e. it looked roughly the same as the part that it was designed to replace, only at a much higher cost.

Due to the unsuitability of the LCA as a target part, the Team worked with Ford to identify a part that might take the place of the LCA that was possible to produce within the program time and budget constraints. When a suitable part was not identified, the Team chose two alternate parts: the first being a military laptop case to demonstrate the draping advantages of RFF, and an automotive seatback to demonstrate the large area capability of the technology. It is these parts that are reflected in the program structure listed below.

Program Structure

The program is structured to develop parts that show the benefits of an NNS RFF. This structure is reflected in the following list (briefly stated):

1. Design, formulate, and produce a suitable polymer matrix material.
2. Produce polyamide-coated carbon fiber tows for test panels
3. Produce composites panels for property measurement then measure them
4. Complete design of lower control arm composite
5. Target part identified and mold located
6. Produce coated tow required for identified parts
7. Create a CT/RFF lay-up via a mostly automated process
8. Obtain a cost estimate of a commercial scale CT/RFF equipment
9. Using modeling/simulation to optimize preform layup.
10. Fabricate and characterize parts

5 RESULTS AND DISCUSSION

5.1 Polymer Matrix Development

The process by which the tow is coated is similar in many respects to pultrusion, with the exception that the contact time between the polymer and the carbon fiber is intentionally kept short so that the polymer does not completely impregnate the carbon fiber tow. In pultrusion, the carbon fiber tows are spread into a thin ribbon, and subsequently exposed to a molten polymer at relatively low shear rates. In the current process, while tow impregnation is not desired during tow-coating, it is still required during molding. This suggests that the polymer properties

required for tape formation should be like those needed for coated-tow fabrication. To enable full impregnation of the carbon fiber bundles during molding, the viscosity of the polymer must be low, and it must wet the fiber very well. While wetting is mostly controlled by the sizing on the carbon fiber, the viscosity of thermoplastics is usually controlled by tuning the polymer molecular weight. In this case, a low molecular weight is preferred. Having a low viscosity matrix is an attractive feature for thermoset materials, and is the primary reason that thermosets are currently widely adopted for CFRP applications.

Unfortunately, the toughness of a thermoplastic polymer is also directly related to its molecular weight, and in this case a low molecular weight is not desired to get a high toughness matrix. This is in direct conflict with the requirements for impregnation. Polymer impregnation is made even more difficult in that carbon fibers are very small in diameter (7 microns), and are available in relatively large numbers within each tow (12k filaments is about the minimum number of filaments per tow). The team therefore needed to design a polyamide-based matrix polymer with a composition that provides the proper balance of toughness and viscosity that will both satisfy the end use and enable the production of high quality tape that will be useful in the AFP.

Finally, the polymer must be able to survive the tape making process with a minimum of degradation so as not to compromise the properties of the UD tape. This entails having sufficient thermal, hydrolytic, and oxidative stability. The proprietary polyamide blend developed by DuPont accomplishes these objectives.

As stated previously, development of suitable mechanical properties in the composites layers of CPV's requires that the carbon fiber be used efficiently. This in turn requires that the carbon fiber be completely wet out by the polymer matrix. The process of wetting out requires that the polymer matrix be of low viscosity and low wetting angle on the fiber. The data shown for this formulation were produced from polymer blends that were processed in 26mm and 30mm Coperion twin-screw extruders and quenched in water baths prior to pelletization into ¼ inch lengths. The materials were then dried overnight for at least 12 hours at 90C and sealed in metalized plastic bags to await testing.

The DuPont-proprietary polymer developed for this program is based on Nylon 6,6 that has been extensively formulated for the sole purpose of being used with continuous carbon fiber. Prior to the rheology experiments, DSC was performed at 10 degrees per minute in sealed aluminum pans. The data are shown in Figure 2.

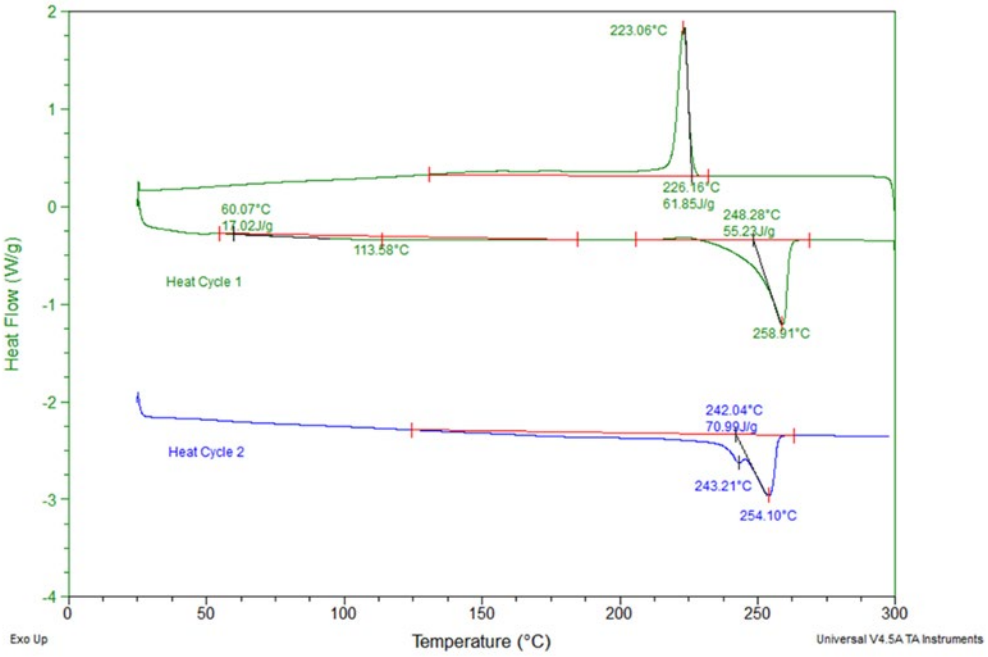

Figure 2. DSC of polymer formulation.

DSC data shows the peak in the melting exotherm to be at 259C, with melting completed by 260C. Crystallization on cooling begins at 226C and peaks at 223C. On the second heating cycle, melting is once again completed by 260C.

Based on the DSC data, the melt flow index of the blend is shown in Figure 3. These measurements were made using the capillary geometry described in ASTM D 1238, with extrudate being collected for 30 seconds with extrapolation to 10 minutes. Relative to unformulated Nylon 6,6, the blend used in this work has a melt flow index roughly ten times higher than Nylon 6,6 at 275C, indicating that it will penetrate carbon fiber bundles at a much higher rate than the unformulated polymer.

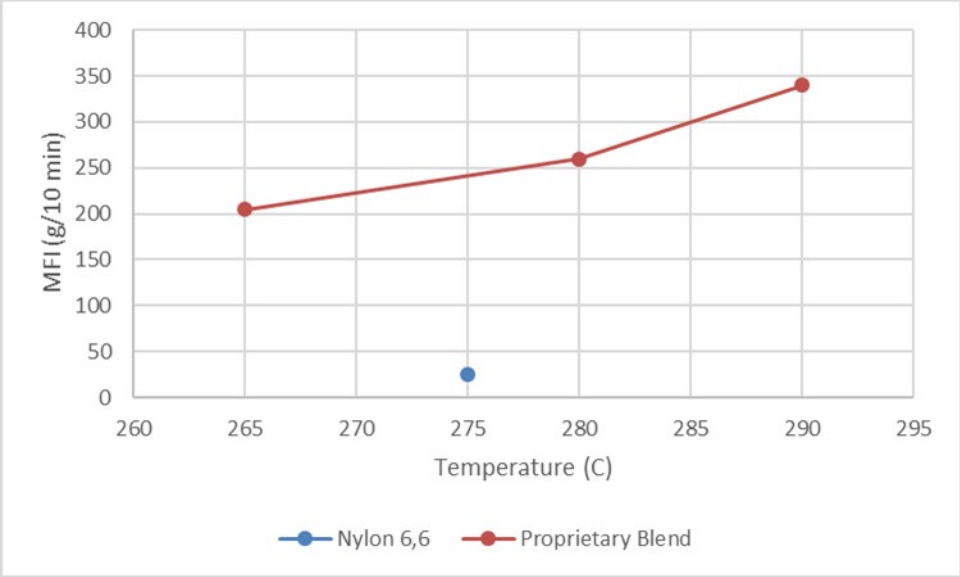

Figure 3. Melt flow index of proprietary blend compared to Nylon 6,6 using ASTM D 1238.

The shear rate dependence is shown in Figure 4. The data was acquired with a capillary rheometer using the method described in ASTM D 3835-16. This data confirms that the viscosity decreases as the temperature increases, as expected from the melt flow index data. It can also be seen that the material is shear thinning, with the amount of shear thinning decreasing with increasing temperature. Finally, it appears that the material is approaching a Newtonian Plateau at the highest temperature tested. All of these observations are consistent with the Team's expectations based on knowledge of the formulation.

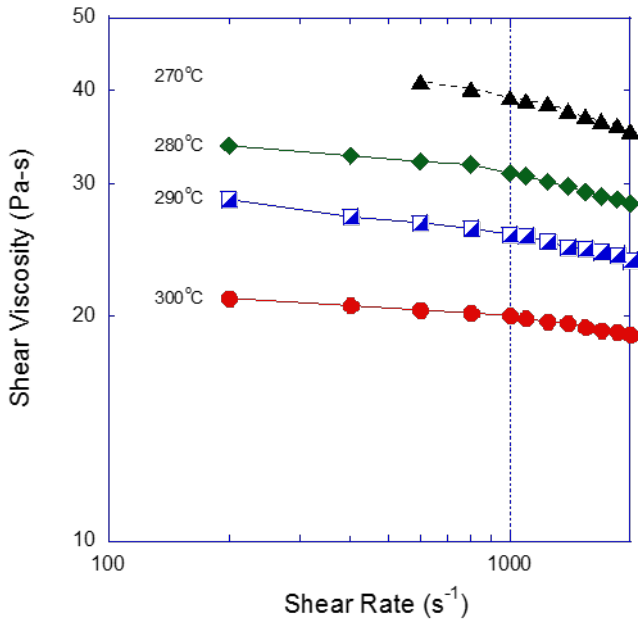

Figure 4. Shear rate dependence of matrix polymer using ASTM D 3835-16.

The molecular weight of the polymer was tested using size exclusion chromatography (SEC) at various stages in the process, as shown in Figure 5.

Figure 5. Molecular weight distribution of matrix polymer as compounded (blue), after tape fabrication (black), and after AFP ring fabrication (red). Internal Nylon 6,6 standard shown in green.

5.2 Production of polyamide-coated carbon fiber tow

Creating a fully consolidated composite from the fiber and polymer components is the crux of the composite-making process, all starting with a carbon fiber/polymer preform. There are many competing technologies to produce thermoplastic composite carbon fiber preforms, each having a characteristic length scale associated with the distance over which the polymer must travel to produce a fully dense composite. On one end of the preform formation spectrum is fully impregnated void-free thermoplastic unidirectional tape, while the other end of the spectrum is represented by stacks of woven fabric interleaved with polymer film. Void free tape formation is very time and energy intensive because the high viscosity thermoplastic polymer is required to impregnate the fiber tows to eliminate porosity. The resulting tape is very stiff and does not conform well to molds at room temperature. On the other hand, fabric/film layup formation is fast and inexpensive because there is no impregnation in the early part this process, and the drape of the dry fabric makes mold filling much easier, with the exception of areas where there is the potential for shear locking.

The time spent making the materials for the initial fiber/polymer construct is compensated by the amount of time that it takes for the consolidation part of the process. Using a void-free UD tape, the polymer does not need to move very far for the part to achieve full density during consolidation; the tapes need only be bonded together. This makes the densification of the part fast. Conversely, in the case of fabric/film stacks, the polymer must flow from the interlayer film all the way to the center of the tows in the woven fabric layer during consolidation, a process that takes a considerable amount of time.

The tow coating manufacturing process is faster than UD tape making, the tooling cost is lower, and it offers substantial automation potential making it ideal for mass production. The thermoplastic polymer/tow of choice for this project was Fibrflex® coated carbon fiber tow. FibrFlex® is Fibrtec's core family of products, and it can be made over a broad range of polymer chemistries and polymer/fiber ratios. It is uniquely flexible and yarn-like, and it readily adapts to the shape of a mold, where in the presence of heat and pressure it is converted into a low-void part.

FibrFlex® represents an intermediate case in the spectrum between fabric/film stacks and UD tapes. Because the tows are not completely impregnated, the tow coating process is faster and less capital-intensive than tape-making. As such, the production cost of FibrFlex® should fall between tapes and interleaved stacks. In addition, because each tow is coated, the polymer needs to flow less distance during consolidation than interleaved fabrics and films. And as such, the consolidation times/costs should also be between tapes and interleaved stacks. This, along with its enhanced draping characteristics, gives FibrFlex an advantage over fabric stack because FibrFlex® can be preformed to near-net shape in Advanced Fiber Placement machines and subsequently deep-draw molded, eliminating the large amount of potential waste generated when using fabric sheets.

5.3 Manual production of composite panels for property measurements

Prior to any design process, a detailed study must be done that covers the properties of the materials to be used. A list of properties required for the part design and simulation was developed by the Team and appears as Table 1.

Table 1. List of properties required and proposed samples for measurement. The subscript accompanying the layup geometry represents the number of single or pairs of fabrics that were used for the preform.

Purpose	Property	Purpose	Layup	Desired Thickness [in]	Width [in]	Length [in]	Samples	Tabs	Standard
UD Characterization	E_{11}	Tensile modulus in the fiber direction	$[0]_8$	0.05	0.5	10	10	Y	ASTM D 3039
	X_{11}	Tensile strength in the fiber direction	$[0/90]_{2s}$	0.05	1	10	5	N	ASTM D 3039
	E_{22}/X_{22T}	Tensile modulus and strength transverse to the fiber	$[90]_{16}$	0.1	0.5	10	5	Y	ASTM D 3039
	G_{12}/X_{12}	Shear modulus and strength	$[45/-45]_{2s}$	0.05	1	10	5	N	ASTM D 3518
	E_{11c}	Compression modulus in the fiber direction	$[0]_{16}$	0.1	0.5	3.18	5	N	ASTMD 638
	X_{11c}	Compression strength in the fiber direction	$[0/90]_{4s}$	0.1	0.5	3.18	5	N	ASTMD 638
	E_{22c}/X_{22c}	Compression modulus and strength transverse to the fiber	$[90]_{16}$	0.1	0.5	3.18	5	N	ASTMD 638
RFF Validation	E_{11}/X_{11T}	RFF tensile modulus and strength	$[0]_4$	0.05	0.5	10	10	N	ASTM D 3039
	E_{11C}/X_{11C}	RFF compression modulus and strength	$[0]_8$	0.1	0.5	10	5	N	ASTM D 638
	G_{12}/X_{12}	RFF shear modulus and strength	$[45/-45]_s$	0.05	1	10	5	N	ASTM D 3518
	E_{11}/X_{11T}	RFF Laminate tensile modulus and strength	$[0/45]_s$	0.05	0.5	10	5	N	ASTM D 3039
	E_{11C}/X_{11C}	RFF Laminate compression modulus and strength	$[0/45]_{2s}$	0.1	0.5	10	5	N	ASTM D 638
	G_{13}/X_{13}	Interlaminar Shear	$[0]_{64}$	0.8	0.1	3	5	N	ASTM D 5379
	G_{IC}	Interlaminar Mode I Fracture Toughness	$[0]_{12}$	0.15	1	6	5	Y	ASTM D5528
	G_{IIC}	Interlaminar Mode II Fracture Toughness	$[0]_{12}$	0.15	1	8	5	N	ASTM D7905

The proposed tests and samples are divided into two categories. In the first, the samples tested provided property values for input to the Purdue Team's modeling and simulation software. In the second category, the tested properties were compared to the software's predictions to validate

the microstructure and construction models.

Unidirectional bars for the E_{11} measurement were fabricated at Fibrtec's facility in Atlanta, TX. The Team molded 2"x 12" x. 050" UD plates in a steel mold with gage stops in place to regulate the thickness. The coated tow was placed in the mold and the top was placed on it and secured. The assembly was heated in an oven to 295C. It was transferred to a cooling press, pressed to the gage stops, and left to cool. After demolding the parts were sent to the Purdue Team for cutting and characterization.

At DuPont, RFF panels were laid up manually as a twelve-inch square. Each panel was designed to be four tows per unit cell pattern, with one unit cell per inch. To begin the process, a paper guide was printed with the required tow placement pattern. Four fully impregnated half-inch wide UD tapes of the same PA/CF composition were attached to one another at the ends to act as a frame around the panel perimeter. Coated-tows were subsequently applied in the requisite pattern and attached to the UD tape frame by tacking them to the frame with a heated soldering iron. The attachment process was repeated in the required pattern described in an earlier report[3] until the RFF was completed.

Depending on the required thickness of the finished plaque, the required number of RFF panels was laid up as a preform; the post-consolidation thickness of the pressed plaques was roughly 1mm for a stack of 4 RFF layers. To begin the consolidation process, two stainless steel plates, one eighth inch thick, were coated with Frekote NC55 mold release. On top of one of the steel plates, a 3 mil thick Kevlar® paper frame was placed. The Kevlar® paper frame is a 13 inch square with a 10 inch square hole cut in the middle. The purpose of the Kevlar® paper is to provide nominal resistance to polymer squeeze-out during the pressing process. The required number of RFF layers is then placed on top of the paper frame, with the preform centered over the hole. The preform is then topped with another Kevlar® paper frame and the final steel plate. An exception to this process was provided for the G_{IC} and G_{IIC} measurements, where a skived Teflon® PTFE film was inserted at the midpoint of the stack, extending halfway into the preform. The preform was consolidated with the PTFE film in place, thereby creating the starter-crack for the toughness measurement.

The press used for this process is a Dr. Collin P 300 P/M. The platens were preheated to 330C. Once heated, the bottom platen was lowered, the preform stack was inserted, and the automated cycle was started. During the cycle, the bottom platen was raised to reach the final pressure of 250 psi. The experimental material/steel plates were held under pressure for 15 seconds, after which the temperature setpoint was lowered to 320C and the pressure maintained for an additional 165 seconds. To finish the cycle, the pressure was released, the heated platens were separated, replaced by water-cooled platens, and pressed at 250 psi pressure for 120 seconds. The cooled stack was finally removed from the press and opened, revealing the finished plaque.

The process used for the fracture toughness samples was modified somewhat. The temperatures of the first two steps were lowered by 20C, and the pressure of each of the steps was reduced to 200 psi.

Subsequent to plaque fabrication, the experimental materials were sent to the Purdue Team for

cutting to the proper dimensions (shown in Table 1) and testing.

5.4 Characterization of composite plaques

Mechanical characterization of the samples produced in Table 1 was performed at the Indiana Manufacturing Institute at Purdue University. A summary of the results from these experiments is provided in Table 2.

Table 2. Summary of Experimental Mechanical Properties for Coated Tow and RFF composites

Material	Layup	% Vol.	ASTM Standard	Property	Avg.	Units	St. Dev.	Min	Max
UD	[0]8	47	ASTM D3039	E_1	108	GPa	6.28	102	122
UD	[0]8	50		E_1	120		5.41	112	129
UD	[0]8	53		E_1	120		2.49	118	126
UD	[0]8	47		X_1	1520	MPa	202	1200	1840
UD	[0]8	50		X_1	1810		101	1650	1980
UD	[0]8	53		X_1	1510		91.1	1350	1680
UD	[0,90]2s	47		E_1	56	GPa	2.32	53.3	59.3
UD	[0,90]2s	50		E_1	60		1.11	58.9	61.5
UD	[0,90]2s	53		E_1	60		1.94	58.6	63.1
UD	[0,90]2s	47		X_1	897	MPa	29.0	874	930
UD	[0,90]2s	50		X_1	901		51.9	850	981
UD	[0,90]2s	53		X_1	961		38.0	918	997
RFF	[0]4	50		E_{1T}	61.5	GPa	6.64	48.3	59.4
RFF	[0]4	50		X_{1T}	851	MPa	158	618	1080
RFF	[0]8	50	ASTM D3410	E_{1C}	54.6	GPa	5.78	47.6	63.1
RFF	[0]8	50		X_{1C}	253	MPa	39.4	196	341
RFF	[±45]4	50	ASTM D3518	G_{12}	1.38	GPa	0.062	1.28	1.47
RFF	[±45]4	50		X_{12}	103	MPa	4.30	95.1	108
RFF	[0]12	50	ASTM 5528	G_{IC}	1180	J/m^2	306	855	1440
RFF	[0]12	50	ASTM D7905	G_{IIC}	2320		332	1980	2760
RFF[0/45]	[0]4	50	ASTM D3039	E_1	48.5	GPa	2.83	44.2	51.8
RFF[0/45]	[0]4	50		X_1	572	MPa	78.8	397	674

The experimental results for the unidirectional aligned plates is compared against the theoretical performance of the composite in Figure 6. The theoretical material properties are determined using Mori Tanaka homogenization of a cylindrical carbon fiber inclusion inside the polyamide matrix. The matrix is assumed to have a Young's modulus of 2500MPa and a Poisson ratio of 0.3, which are typical of a polyamide resin. The carbon fiber is a 700-34 grade PAN-based fiber with Longitudinal Young's modulus of 234GPa (34Msi) and tensile strength of 4830MPa (700ksi), as reported on the material data sheet. The remaining four properties that define the transversely isotropic elastic response of the carbon fiber are assumed based on typical property relationships for carbon fibers. The transverse Young's modulus is taken to be 12.5GPa, shear modulus is 25GPa, transverse Poisson ratio is 0.291, and in-plane Poisson ratio is 0.206. The theoretical mean line in Figure 6 is generated by computing the Mori Tanaka homogenized

longitudinal modulus of the composite for varying fiber volume fractions. The 95% confidence bound region is generated assuming a coefficient of variation of 4% for the longitudinal modulus of the carbon fibers themselves and computing the homogenized properties of the resulting composite. The experimental results from the UD plates are in line with the theoretical stiffness values.

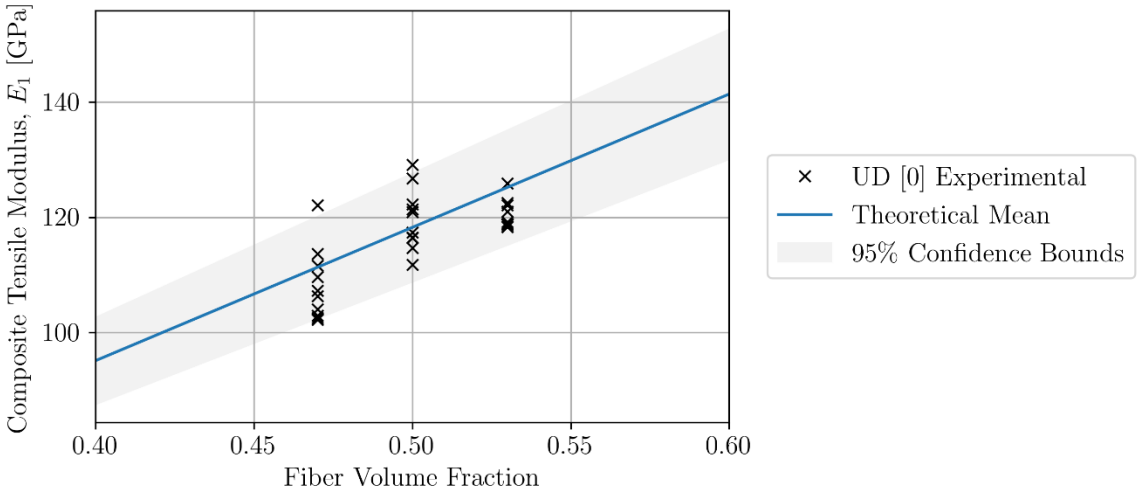

Figure 6. Experimental and theoretical tensile modulus for unidirectional plaques pressed from coated tows.

The longitudinal modulus from the experiments increases as the fiber volume fraction increases from 47% to 50%, but the 50% and 53% mean properties are equivalent. While this could be an indication of a processing induced effect in the manufacture of the coated tows or resulting plates, it is worth noting the theoretical bounds on the longitudinal modulus for the three grades of composite used in this study have a significant overlap. The apparent equivalence between the 50% and 53% grades could also be attributed to a statistical effect from natural variability in fiber stiffness and volume fraction variation.

The longitudinal strength of the UD plates as measured is significantly lower than theoretical strength of the composite based on a rule of mixtures approximation of the strength as the product of the fiber volume fraction and reported fiber strength. The theoretical strength, using a fiber strength of 4830MPa, is 2270, 2410, and 2560MPa for the 47, 50, and 53% grades, respectively. The experimental values of 1520, 1810, and 1510MPa, are 33%, 25%, and 41% lower than their respective theoretical values. There is also a decrease in mean strength from the 50% to 53% grades. Unidirectional tensile strength tests are notorious for underperforming theoretical strength values. Small deviations from a strictly longitudinal fiber direction from coupon misalignment, fiber misalignment in processing, or fiber waviness, and can all contribute to lower than expected strength values, especially considering the “weakest link” nature of failure in this configuration.

The experimental longitudinal modulus of a plate manufactured from layers of coated tows oriented in a $[0, 90]_{2S}$ configuration is compared against the theoretical stiffness of this construction in Figure 7. Mori Tanaka homogenization is again used to compute the transversely isotropic homogenized stiffness of the coated tows and associated plies, and classical laminate analysis is used to compute the resulting laminate stiffness. In this case, the experimental observed values are slightly lower than the theoretical mean values by 3.5%, 2.5%, and 7.6% for

the 47, 50, and 53% grades, respectively. The values from the individual tests tend to fall within the lower half of the 95% confidence bounds.

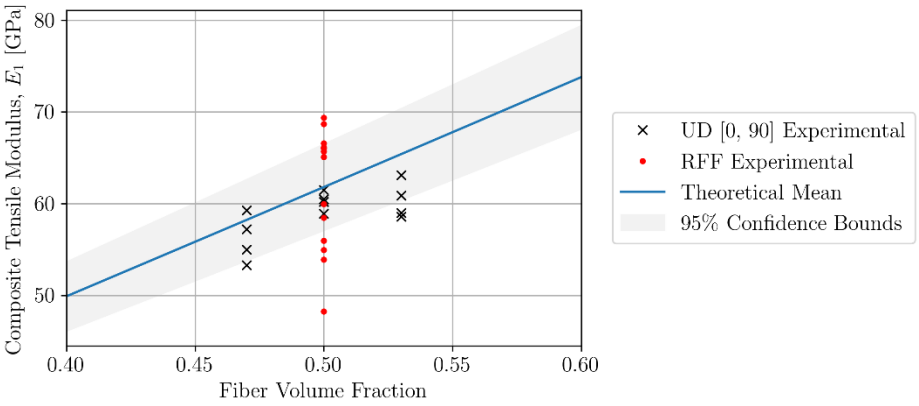

Figure 7. Experimental and theoretical tensile modulus for [0, 90]$_{2s}$ plaques pressed from coated tows.

The RFF panels used in the characterization and subsequent design efforts used the 50% fiber volume fraction grade coated tows in its construction with a 4x4 RFF unit cell, primarily at orthogonal orientations. The mean experimental stiffness of the RFF coupons in tension is 61.5GPa, compared with 60.0GPa for the [0, 90]$_{2S}$ plates with 50% fiber volume fraction. These two configurations have the same fiber volume fraction and same percentage of fibers aligned in the longitudinal and transverse directions, with the difference being that the fibers in the RFF construction will change elevation within the depth of the laminate from the RFF pattern. It would be expected that the undulations of the fibers in the RFF would degrade the stiffness, but from the experimental results, this does not appear to have a significant effect.

The first order theoretical strength of the [0, 90]$_{2S}$ and RFF plates can be approximated by multiplying the fiber volume fraction, percent of fibers oriented in the longitudinal direction, and the strength of the constituent fibers. A comparison of this theoretical strength against the strength of the [0, 90]$_{2S}$ plates made from laminated unidirectional tows and using RFF fabrics is shown in Figure 8. A 7% coefficient of variation in fiber strength is used to generate the 95% confidence bounds. The mean experimental strengths of these orthogonal fiber configurations are 21, 25, and 25% of the theoretical strength for the 47, 50, and 53% fiber volume fraction [0, 90]$_{2S}$ plates. The mean strength of the RFF coupons is 29% of the theoretical strength, with a coefficient of variation of 17.8% in the experiments, which is quite high. This indicates significant variability in the strength of the RFF plates. To put the strength of the RFF plates in context of other lightweight material alternatives, the mean RFF strength of 851MPa is nearly three times the ultimate strength of aluminum (300MPa) and nearly four times the tensile strength of magnesium (230MPa).

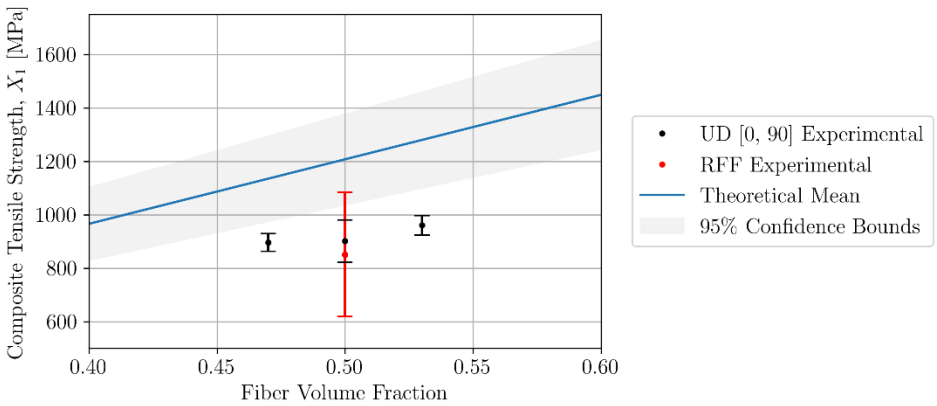

Figure 8. Composite strength of $[0, 90]_{2S}$ and RFF plates compared with theoretical strength predictions.

The mean experimental shear modulus of the RFF plates cut into coupons with a nominal ±45° tow orientation is 1.38GPa with a coefficient of variation of 4.5% using the chord shear modulus of elasticity method as defined in the ASTM D3518 standard between 2000 and 6000με. The theoretical in-plane shear modulus of the RFF using the mesoscale model of the finite element as shown in Figure 9 with a 4x4 unit cell and the nominal elastic properties used above is 2.64GPa.

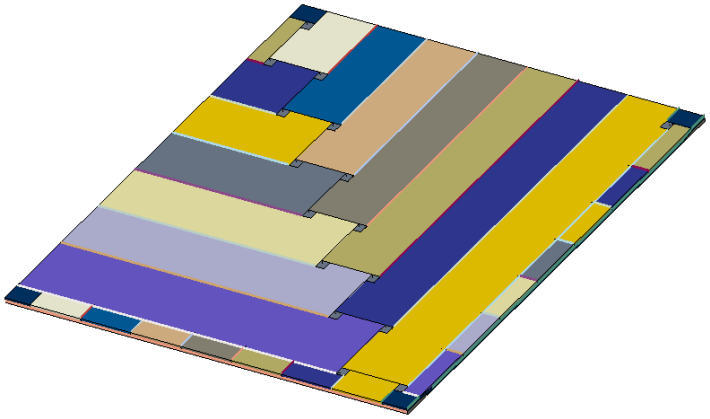

Figure 9. Finite element model for mesostructure of the RFF construction with 8x8 unit cell.

The likely cause of the discrepancy between the theoretical and measured moduli is the highly nonlinear stress-strain response of the resin. This nonlinearity is observed in the stress-strain curves of the $[45, -45]_{2S}$ coupons shown in Figure 10. The theoretical and measured shear moduli are included in the figure to provide a reference for comparison. Figure 11 shows a closer magnification of the shear stress-strain response indicating that the theoretical value of 2.6GPa does capture the initial behavior of the curve, but as non-linearity sets in in the material, inelastic strain effects result in a much lower effective shear modulus. The effect of matrix effective modulus on the effective in-plane shear modulus of the RFF is shown in Figure 12. It is noted that while the orthogonal configuration of tows does yield a composite with high shear compliance, the incorporation of off-axis tows can significantly limit this impact.

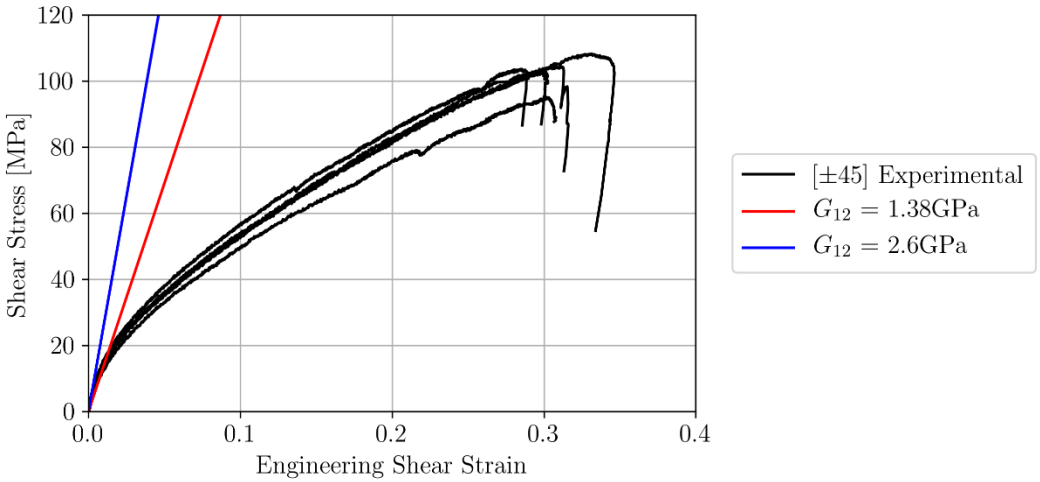

Figure 10. Engineering shear strain vs. shear stress curves for the [+45,-45]$_{2S}$ RFF coupons.

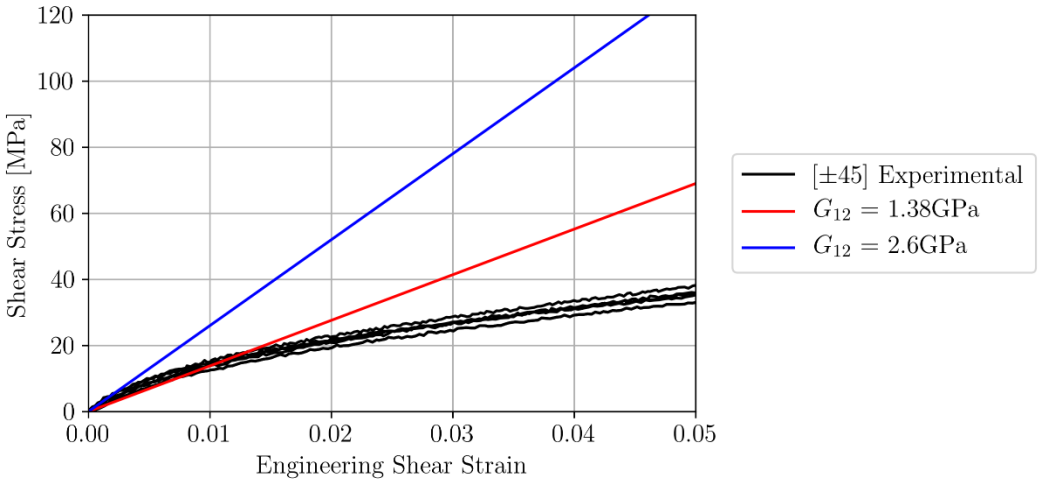

Figure 11. Small strain range of the engineering shear strain vs. shear stress curves for the [+45,-45]2S RFF coupons.

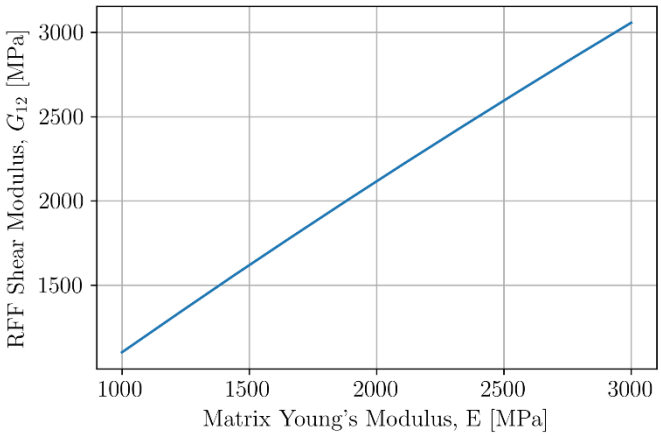

Figure 12. Impact of effective matrix modulus on RFF in-plane shear modulus.

A more detailed account of the characterization tools, methods, and results are included in Appendix 1 of this report.

5.5 Design Lower Control Arm

The initial demonstration part identified to target in this program was the Lower Control Arm (LCA) for the Ford Fusion. This part was down-selected from a number of potential automotive components based on a number of selection criteria, including a relatively simple geometry, medium part size, performance being stiffness and/or strength-critical, no crash safety requirements, and one that the assembled team can offer design support on. Additionally, in order to focus the design effort on the application of the RFF fabric, the design of the LCA in this program was limited to designs that use only the RFF fabric, and not hybrid technologies such as hybrid injection molding, hybrid compression molding, or local tape reinforcement. Two existing LCA designs were available for comparison - one stamped steel construction and one cast aluminum, shown in Figure 13. The aluminum part design weighs 2.52 kg and the steel design weighs 2.93kg. The design team for this effort included representatives from DuPont, Fibrtec, Ford, and Purdue.

a) 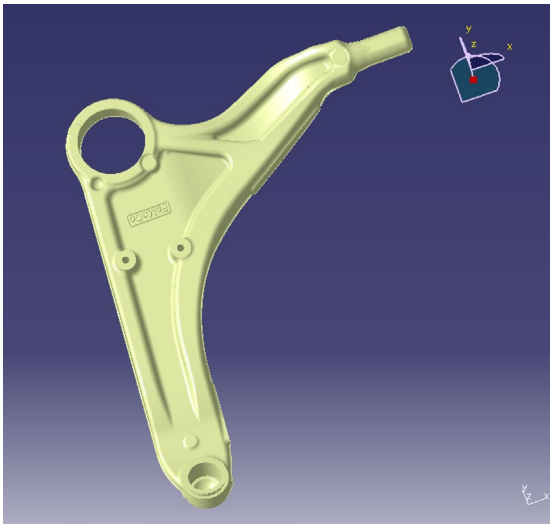 b) 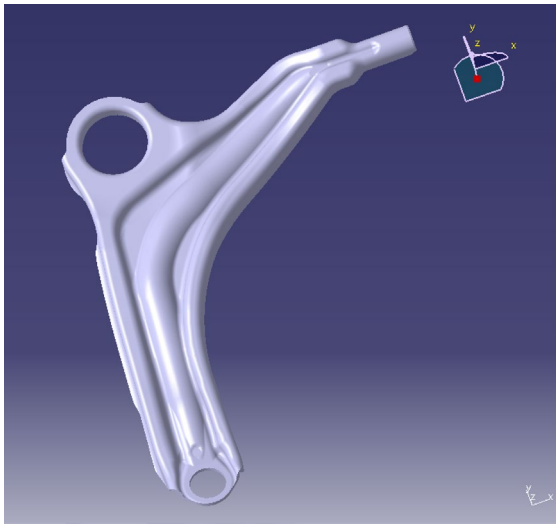

Figure 13. Metal LCA designs for a) cast aluminum and b) stamped steel.

The broad design methodology adopted for developing the composite LCA design was as follows:

1. Develop the consistent FEA modeling approach for both the metal and composite designs.
2. Verify the FEA approach with the current metal designs against design requirements.
3. Perform topology optimization for the control arm with relaxed assembly interference constraints.
4. Adjust the composite design space for interferences from nearby components in the assembly.
5. Refine the composite LCA model to meet design requirements and design space by optimizing thickness, ply orientations, and/or cross-section geometry.
6. Assess the feasibility of the composite LCA design.

5.5.1 FEA Modeling Approach

The LCA has three connection points to integrate the part into the vehicle structure. While the design of these connections is critical for final part design, the focus of the design effort for this program was the bulk design for the part with idealized connection points initially. The preliminary design requirements for the control arm included criteria for part stiffness, strength, and fatigue life. Based on previous experience from similar parts, the design process began with identifying a construction that would meet the stiffness requirements first, and then afterwards the strength and fatigue requirements would be addressed. The stress analysis for evaluating the baseline performance of the metal designs and designing the composite LCA was performed using Abaqus from Dassault Systemes. Topology optimization and parametric optimization of the composite designs were performed using Tosca and Isight, respectively, which are also from Dassault Systemes and utilize the Abaqus FEA solver.

The stiffness requirements, shown in Figure 14, consist of separate loading cases for fore/aft loading (X-direction) and inward/outward lateral loading (Y-direction). The loads are applied at the location of the ball joint connection at the wheel (bottom of the image in Figure 14) and pin supports are applied at the indicated triangles for the hoop bushing (top left) and hydrobushing (top right) that connect the LCA to the vehicle frame. A rotational constraint is applied about the x-axis for the support at the hoop bushing as well. For each load case, the point load is applied in the required direction and the resulting stiffness, K_x or K_y, is determined by dividing the applied force by the imparted displacement in the direction of the applied force.

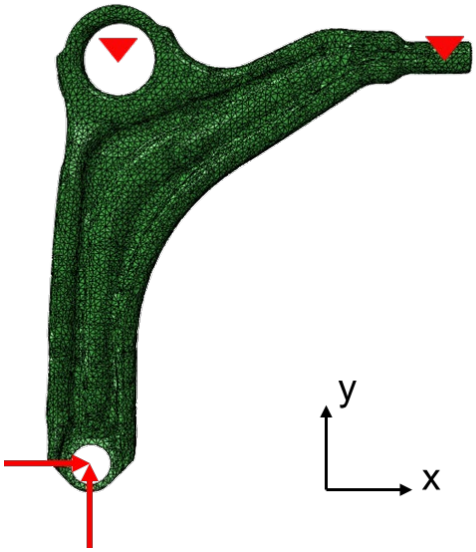

Figure 14. Loading diagram for LCA stiffness requirements.

In order to model the load and boundary conditions in the FEA, a region of nodes near each of the three points of interest were defined in the model to idealize the load distribution provided by the connection and minimize stress concentration effects in the analysis. These nodes are tied to a single reference point through a multi-point constraint (MPC) which associates the averaged displacement of the defined nodes in the FE mesh to the reference point displacement. The load and boundary conditions are applied to the reference points and transferred to the LCA through the MPC.

Shell elements were used in the finite element model for the stamped steel and the RFF parts. Figure 15 shows the stamped shape of the steel LCA with a thickness of 4mm. The baseline steel model is comprised of 20497 S3R elements; the iterations for the RFF construction utilize a similar mesh characteristic size. The cast aluminum part contains a more complex geometry as seen in Figure 15b and requires a solid element mesh. 135767 quadratic tetrahedral C3D10 elements are used in the FEA model for the cast aluminum part.

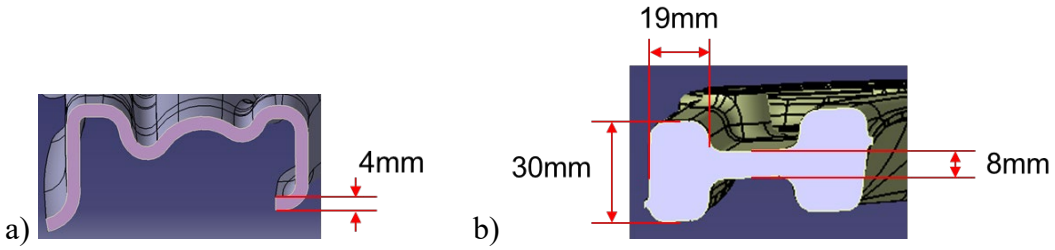

Figure 15. Cross section of the LCA between the hoop bushing and ball joint for the a) stamped steel construction and b) cast aluminum construction.

5.5.2 FEA Verification with Metal Designs

The FEA modeling approach for the LCA is verified by comparing the stiffness of the steel and aluminum parts through the displaced shape of the model under the applied design loads. The stiffness of the part under separate x- and y-loading is determined by applying the design load to the ball joint reference point equal to the design stiffness value. If the structural stiffness of the part is identical to the design stiffness, the resulting displacement at the reference point in the loading direction will be equal to one. Displacement above one indicates that the part stiffness is under the design requirement; displacement below one indicates greater stiffness than the design requirement. The displaced shape for the steel construction under x- and y-loading is shown in Figure 16. The displacement at the reference node under x-loading for the steel model is 1.11, indicating a part stiffness of 90% of the target design value for the x-direction and the displacement under y-loading is 0.89, for a stiffness 112% of the design value.

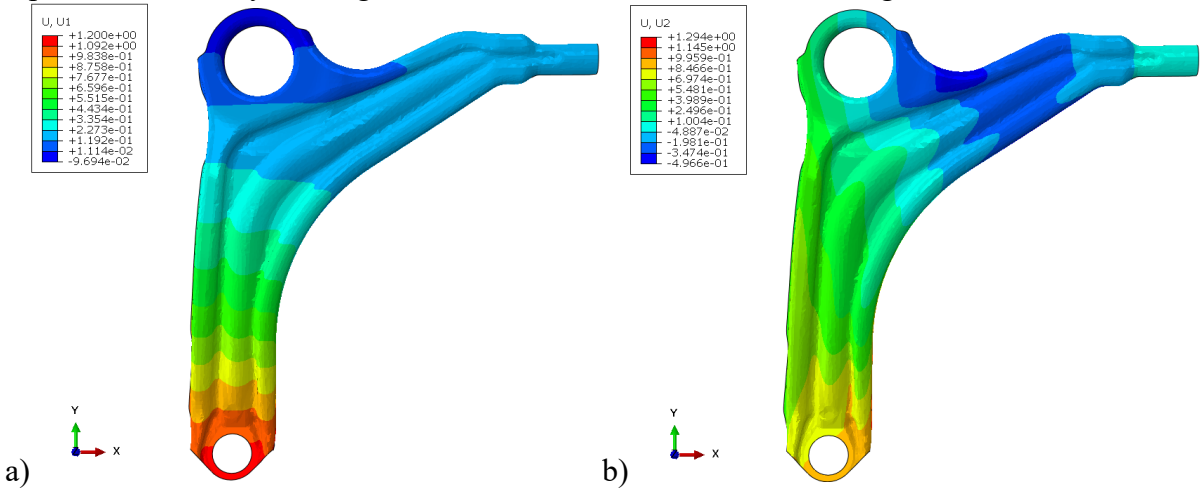

Figure 16. Displacement of the stamped steel geometry under target design load a) in the x-direction with x-load and b) in the y-direction with the y-load.

The displaced shapes for the aluminum construction are shown in Figure 17. The displacement at the reference node under x-loading is 1.04, indicating a part stiffness 96% of the design target value and the displacement under y-loading is 1.03 for a part stiffness 97% of the target design

value. The part stiffness for three out of the four cases are slightly under the target stiffness values, but each value is at least 90% of the target value, indicating that the modeling approach and boundary conditions are representative of the design intent for the part.

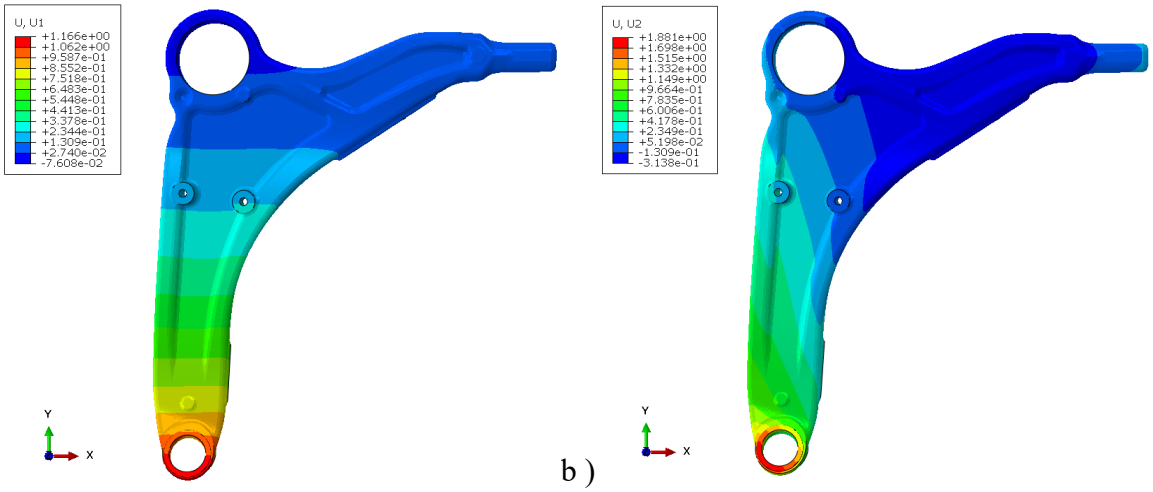

Figure 17. Displacement of the cast aluminum geometry under target design load a) in the x-direction with x-load and b) in the y-direction with the y-load.

5.5.3 Initial Composite Part Topology Optimization

To begin the composite design process, topology optimization was used on the overall shape of the LCA to evaluate optimal placement of material to meet the structural requirements of the part. The mechanical properties of the composite used in the initial optimization process were taken from experimental testing performed prior to the characterization work performed in this phase of the project and are provided in Table 3.

Table 3. Initial RFF mechanical properties for topology optimization.

Property	Value	Property	Value	Property	Value
E1	52 GPa	ν_{12}	0.025	G_{12}	2.2 GPa
E2	52 GPa	ν_{13}	0.381	G_{13}	1.9 GPa
E3	5.1 GPa	ν_{23}	0.381	G_{23}	1.9 GPa

During the early portion of this design effort, the consensus amongst the design team was that the true design space for the LCA was larger than the envelope used by the steel and aluminum versions of the part. To gain further understanding on the load paths in the part, the initial topology optimization exercise started with a flat rectangular area containing the loading and support points for the LCA with the stiffness loads in the X and Y directions applied, as shown in Figure 18a. The topology optimization algorithm applied in Tosca works by maximizing the stiffness of the part while keeping mass under a specified target value by applying a density penalty to the elements in the model accompanied by an associated reduction in stiffness. In this way, the elements that contribute most to the stiffness are retained and the non-critical elements are removed by reducing their density to zero. The initial run of the topology optimization yields the area shown in Figure 18b. The gap in the top right of the area is an artifact of the density reduction threshold used to display the optimization result and highlights the fact that the topology optimization is a useful tool for driving design direction for the part but does require

post-processing to yield a physically meaningful result.

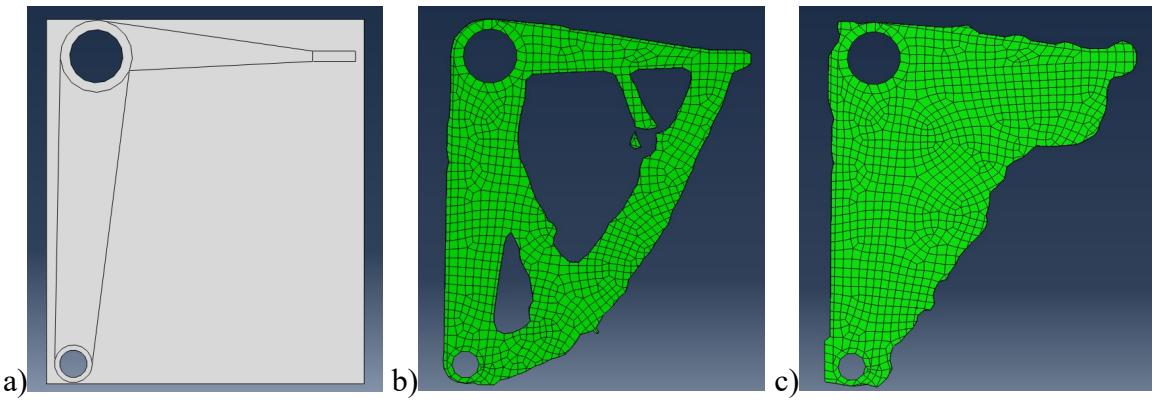

Figure 18. Topology optimization geometries used for 2D representation of the LCA with a) initial geometry, b) preliminary topology optimization, and c) optimized topology with no interior holes.

One physical constraint from the RFF manufacturing process is that the interior holes in the part are not ideal from a production standpoint, as this would require additional manufacturing steps to remove and result in a large amount of scrap. To account for this, the topology optimization algorithm was adjusted using an option disallow interior holes in the final geometry. This result is shown in Figure 18c where the material tends to a triangular shape connecting the three loading and support points. This result is consistent with what would be expected from engineering intuition. Superimposing the outline of the steel LCA over this result shows that the optimization result occupies more space than existing design in the X-Y plane.

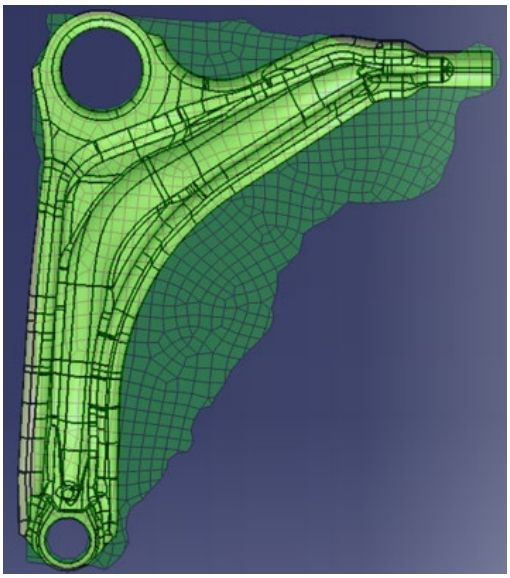

Figure 19. Superposition of the steel LCA outline over the 2D rough optimization for the composite LCA.

5.5.4 Composite Part Design Space Interferences and 3D Topology Optimization

After further consideration of the design requirements for the LCA, it was determined that the open design space did not provide a realistic set of constraints for the part, and the design space interferences were readjusted. The primary source of interferences for the LCA is from the movement of the wheel (attached at the ball joint). In coordination with designers at Ford, the wheel movement envelope around the LCA was determined. This interference is shown in Figure

20. Considering the new design envelope and the three-dimensional positioning of the connection points, a three dimensional design envelope for the composite LCA was generated as shown in Figure 20b.

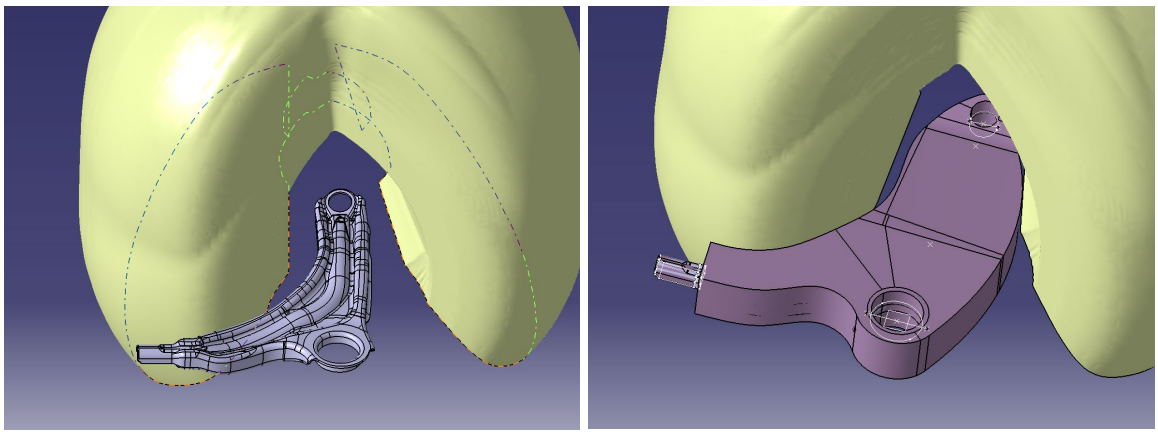

Figure 20. a) Steel LCA construction with wheel movement envelope and b) Composite LCA design space.

Performing a topology optimization on the bulk design volume shown in Figure 20b yields the rough optimized geometry in Figure 21 using the material properties from Table 3 with local material orientation equivalent to the global axes. One of the challenges in using topology optimization with composite materials and in composite sheet forming processes is that the topology optimization software does not include draping and forming effects in the model. Because of this, the fiber orientations and resulting mechanical properties in the optimization model can diverge significantly from the expected orientation state in the part. This effect further establishes that the optimization result is a first pass solution to where material is needed in general and requires significant modifications. Considering the interpretation required for the optimization result regardless of the optimization constraints, the model was run with as few geometry constraints as possible. This results in a model with material primarily along the edges of the design space with some minimal connecting elements in the middle. This type of construction is visible in the metal cross sections in Figure 15 where the aluminum cross section forms an I-shape and the stamped steel forms a C-channel shape to resist the bending moment about the Z-axis imparted by the loading in the X-direction.

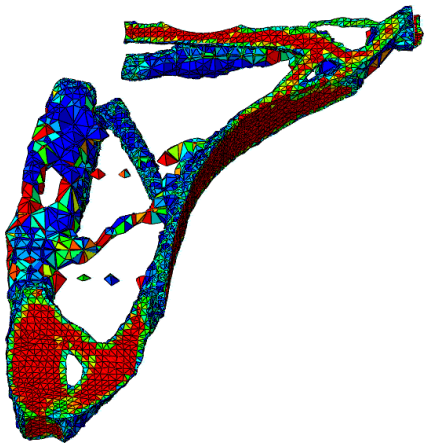

Figure 21. Rough topology optimization using LCA design space constrained by wheel movement envelope.

5.5.5 RFF LCA Design

In consideration of manufacturing limitations and program goals for this research project, the design of the RFF version for the LCA was based on a single stack, or laminate, of RFF sheets made from orthogonally aligned coated tows. Individual sheets in the laminate could be rotated in relation to one another, but all plies were limited to the [0, 90] RFF configuration. Advanced design concepts such as variable stacking sequences over the design area, non-orthogonal crossover angles, or local coated tow reinforcement were not included in the initial design.

Based on the processing similarity between steel stamping and the compression molding process for the RFF, the initial design of the composite LCA was based on the stamped steel part, Figure 22. At this stage of the design, the mechanical properties of the RFF from initial experimental measurements were used as the basis for the orthotropic properties of the RFF material with 50% fiber volume fraction and the orthogonal tow arrangement. The properties used for the RFF LCA design are presented in Table 4.

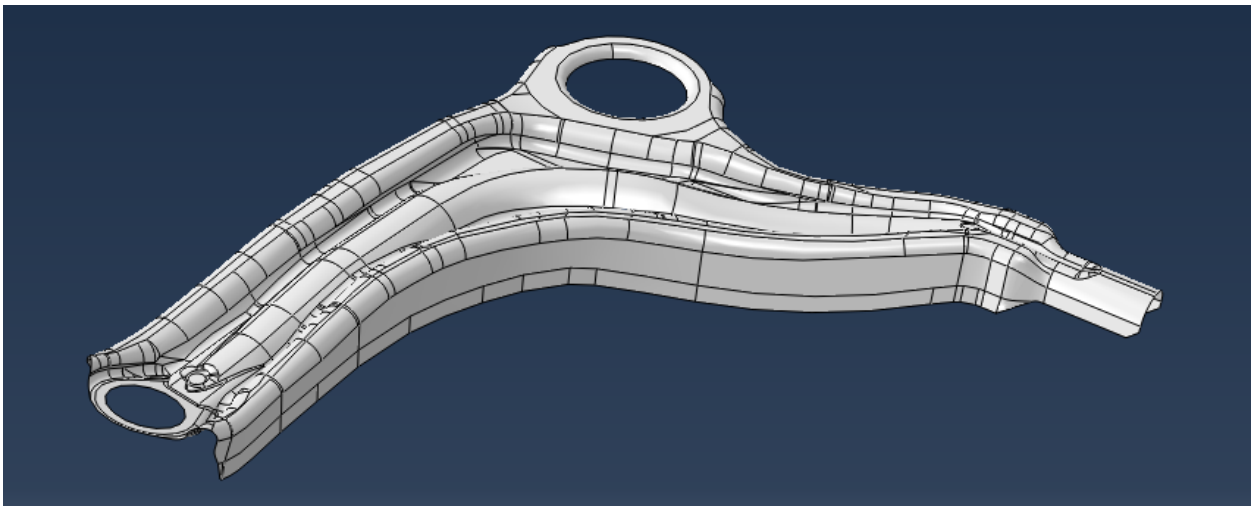

Figure 22. Initial RFF Geometry.

Table 4. RFF mechanical properties for 3D design.

Property	Value	Property	Value	Property	Value
E1	58.7 GPa	ν_{12}	0.029	G_{12}	2.82 GPa
E2	58.7 GPa	ν_{13}	0.31	G_{13}	2.43 GPa
E3	5.1 GPa	ν_{23}	0.31	G_{23}	2.43 GPa

Using the contoured surface in Figure 22 with the constraint of having a single stacking sequence throughout the part with layers of the orthogonal RFF, the degrees of freedom for optimization are the number of plies in the laminate and the local orientation of those plies. The effect of local orientation on the effective orthotropic moduli of a single ply is shown in Figure 23. Due to the low shear modulus of the RFF, as the material rotates away from the 0- and 90-degree orientations, the Young's moduli of the RFF is significantly penalized. The result is that plies that are not aligned with their local X and Y axes close to the global X and Y axes do not

contribute greatly to the global stiffness of the part in the Y load case. Some off-axis plies are necessary in the construction to provide stability, but most RFF plies are oriented with the global X-Y axes.

In order the meet the stiffness requirements, the optimal laminate is 19mm thick, or 68 plies at a ply thickness of 0.28mm and has a mass of 2.3kg, with a stacking sequence of $[0_{19}, 45_{15}]_s$. Molding a part of this size would be very challenging. A few of the technical challenges include geometrical issues from the difference in internal to external radii where the flanges of the LCA turn down, the significant loft, or increased pre-consolidated thickness, of the RFF, and the application of pressure on the near-vertical sides of the LCA. The low through-thickness thermal conductivity of the material also significantly increases the time required to melt the polymer in the middle of the laminate and process the part.

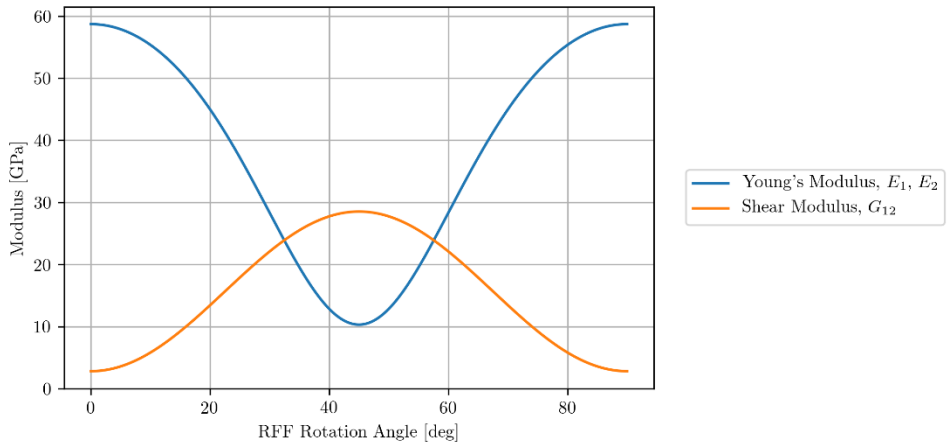

Figure 23. Effect of local ply orientation on effective moduli in the laminate axes.

The results of the RFF LCA preliminary design indicate that manufacturing the LCA with the initial constraints is not feasible. If the constraint that the laminate must be the same throughout the part is relaxed, there is some further opportunity to reduce the mass of the part by dropping some of the plies in the region of the LCA between the hoop bushing and the hydro-bushing. To investigate the optimization of the design with non-uniform stacking sequences, the LCA was split into two regions as in Figure 24. Utilizing this configuration, the mass of the part is reduced to 2.2kg with the upper region being 16.8mm thick and the lower region 18.8mm thick. The marginal reduction in mass from this approach still faces the same manufacturing challenges as the consistent part thickness with the added challenge of designing a tool to accommodate the transition region between part thicknesses.

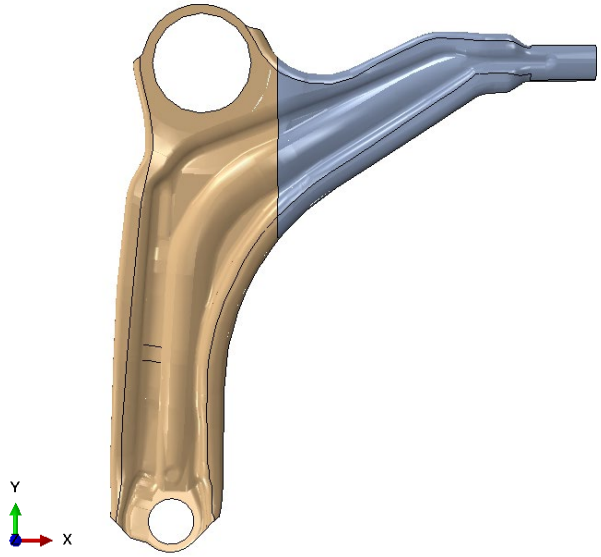

Figure 24. Line separating the two laminate regions for the RFF LCA.

The final opportunity for reducing part mass investigated in this report is the incorporation of layers in the laminate containing fully aligned coated tows, i.e. unidirectional layers. This could be achieved physically through prepreg tape, pre-formed bundles of tows, or through tacking additional coated tows to the RFF pattern beyond the fundamental unit cell. The result is that more fibers can be aligned in the critical direction governing part stiffness between the ball joint and the hoop bushing in the global Y direction.

To investigate the configuration with unidirectional tows, the LCA model for the RFF was further partitioned as in Figure 25 to enable the alignment of fibers with the flanges of the part. In this case, the design included layers of RFF material aligned with the global X-Y axes of the model and oriented at 45 degree angle in plane on the top and bottom of the stacking sequence for the part with the unidirectional material between the layers for a $\left[0_x^{RFF}, 45_y^{RFF}, 0_z^{UNI}\right]_s$ stacking sequence where the 0 or 45 indicate the in-plane rotation of the ply with respect to the local laminate orientation, the superscript *RFF* or *UNI* indicates the configuration of the layer, x, y, and z denote the number of plies in the particular layer, and the *s* indicates that the stacking sequence is symmetric. The local orientations are shown in Figure 25 with green arrows. The assumption in the design is that the unidirectional material will be able to be steered along the flanges as required. With this configuration, the optimal stacking sequence from the preliminary analysis for regions A, D, and E was determined to be $[0_4^{RFF}, 45_7^{RFF}, 0_{18}^{UNI}]_s$ and for B and C $[0_4^{RFF}, 45_7^{RFF}, 0_{14}^{UNI}]_s$. This results in a 1.87kg part.

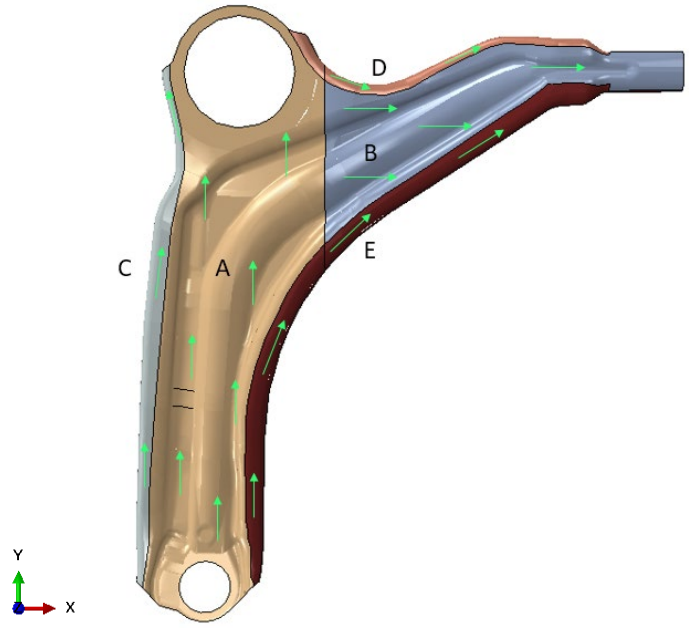

Figure 25. Added regions for unidirectionally aligned tows in the flanges.

5.5.6 Composite LCA Design Feasibility

The design optimization efforts in the previous section have shown that a lightweight LCA with the CT and RFF material system is theoretically possible, achieving a 25% mass reduction for the design iteration with locally placed unidirectional material compared to the 2.5kg aluminum design. In addition, the geometry of the LCA design does contain complex geometry that could demonstrate the favorability of the RFF as compared to traditional woven fabrics. Figure 26 shows the draping contours for LCA with the yellow regions indicating shear angles greater than 15 degrees and red indicating shear angles greater than 30 degrees. Traditional woven fabrics will wrinkle in these regions, whereas the early testing of the RFF has indicated that it will not be as susceptible to wrinkling at these shearing angles.

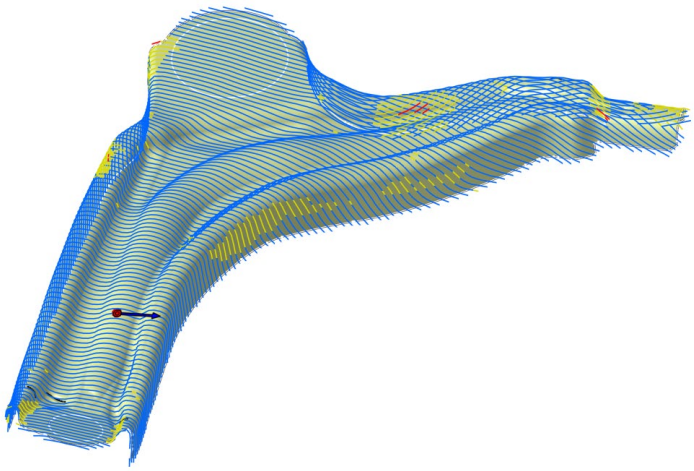

Figure 26. Shearing angle for fabric draping over LCA design with yellow >15deg and red >30deg.

While the design does highlight the drapability of RFF and a preliminary design with mass reduction has been developed, the manufacturing challenges associated with making a part

16mm thick with significant curvature have led the project team to decide that manufacturing the LCA is not advisable within the scope of this project. While the LCA considered in this project does not appear to be feasible with the RFF material alone, there are still potential applications for LCA design on vehicles with lighter loading requirements and/or larger design envelopes. Additionally, the RFF material system is a potential candidate for hybrid molding technologies where the RFF can provide aligned stiffness in the form of organo-sheets while utilizing short fiber injection or compression molding to yield complex geometries with ribs and reduced width web sections to improve stiffness to mass of the part.

5.6 Production of RFF with Automated Fiber Placement

A total of 8 kg of carbon-fiber coated-tow were supplied to Automated Dynamics, Niskayuna, NY (ADC) for the creation of the RFF panels via Automated Fiber Placement. According to ADC, "Automated Fiber Placement (AFP) is one of the most advanced methods for fabricating composite structures. This method is used almost exclusively with continuous fiber reinforced tape and can be used with thermoset and thermoplastic materials. As an Additive Manufacturing process, our robotic AFP systems place composite material and build a structure one ply at a time. This method allows the fabrication of highly customized parts as each ply can be placed at different angles to best carry the required loads."

For this program, the AFP approach taken was very much like the manual build process described above, the only exception being that the coated-tow was sealed to the UD tape frame via laser bonding as in Figure 27. A more comprehensive description of the AFP process used to make RFF fabrics is discussed elsewhere[3]. For the purposes of this demonstration, only one coated tow was applied during every pass of the AFP deposition head. This was done to eliminate tooling costs that would be required for redesigning the robot so that multiple tows could be applied simultaneously, which would reduce the processing time significantly.

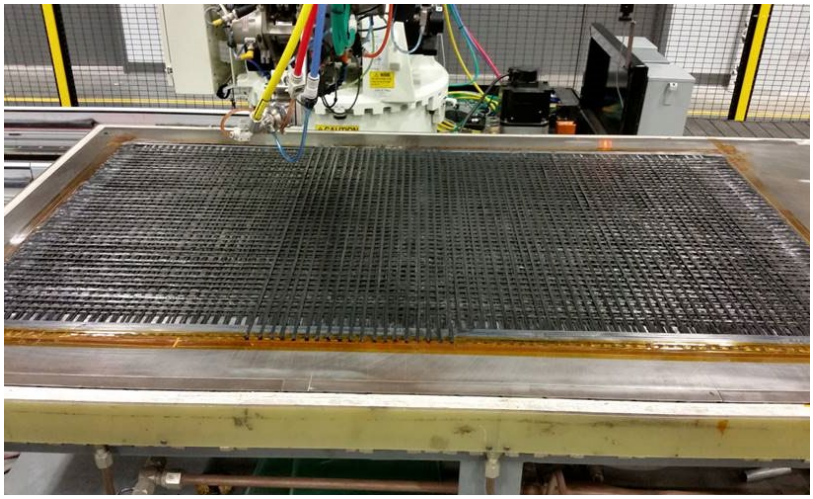

Figure 27. RFF panel during fabrication at ADC.

5.7 Fabrication of Manta laptop case

Two preforms for the Manta laptop case were fabricated, one from woven 2x2 twill fabric and one using RFF. Both preforms were made from Fibrflex as described in Section 5.2 and 5.3. The Fibrflex material chosen for this work was 50 volume percent carbon fiber. The pick count for

the warp and fill was 5x5 of the twill fabric providing a fiber areal weight of 328 gsm. The preform measured 12 x 14 inches and three plies were used. The unconsolidated 3 ply Twill preform was 2.2mm thick and the net molded wall thickness was 1.14mm. The RFF preform was 4-5mm thick with 1.14mm molded wall thickness.

The process to mold the part was a simple compression method. An aluminum mold for a military ruggedized tablet computer (Manta) was used. It was chosen because of its availability, and due to its complex topological features, which are challenging for a continuous fiber composite material. The preform was placed over the core side of the room-temperature mold and centered using the guide pins as shown in Figure 28. The cavity side was place on top and pre-compressed with less than 5 psi pressure to insure intimacy of the preform and mold surface. The exposed perimeter of the mold assembly exposing the preform was wrapped in foil to protect the fabric from extended elevated temperature exposure of the circulating oven used. A Blue M Oven (model DC-256G) was set to 482°C and preheated. The mold assembly was placed in the oven with a thermocouple inserted in a thermowell in the mold side. When the mold reached 283°C the oven set point was reduced to 400°C and a dwell timer was set for 10 minutes. At the end of the dwell period, the mold was removed from the oven and moved to a 40-ton press with platens at ambient temperature. Within the second press, the mold was placed on a 6mm thick mica plate, and one of the same size was placed on top of the mold prior to closing the press to ensure uniform cooling of the aluminum mold from the top to bottom. The mold was closed to mold stops and pressure was set to a minimum with enough to maintain full closure. After the mold cooled to 190°C it was removed from the press and the mold halves separated and the part removed as shown in Figure 29 and Figure 30. The procedure was the same for both parts produced.

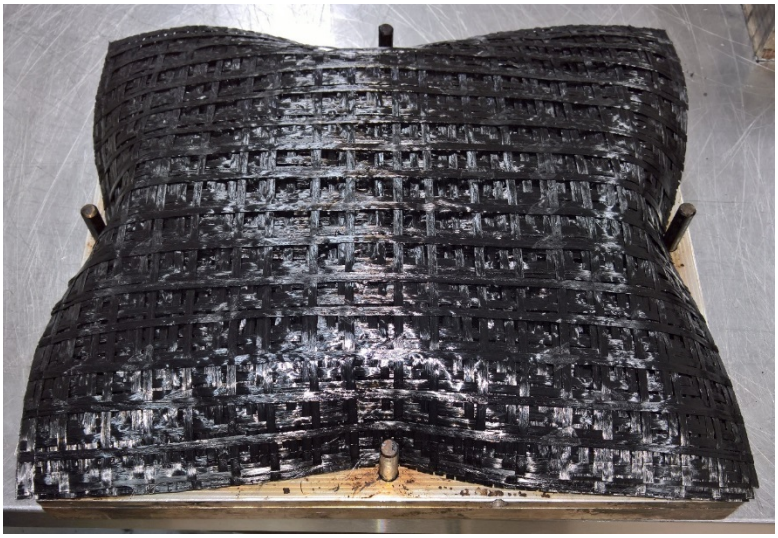

Figure 28. RFF laid over lower portion of Manta mold.

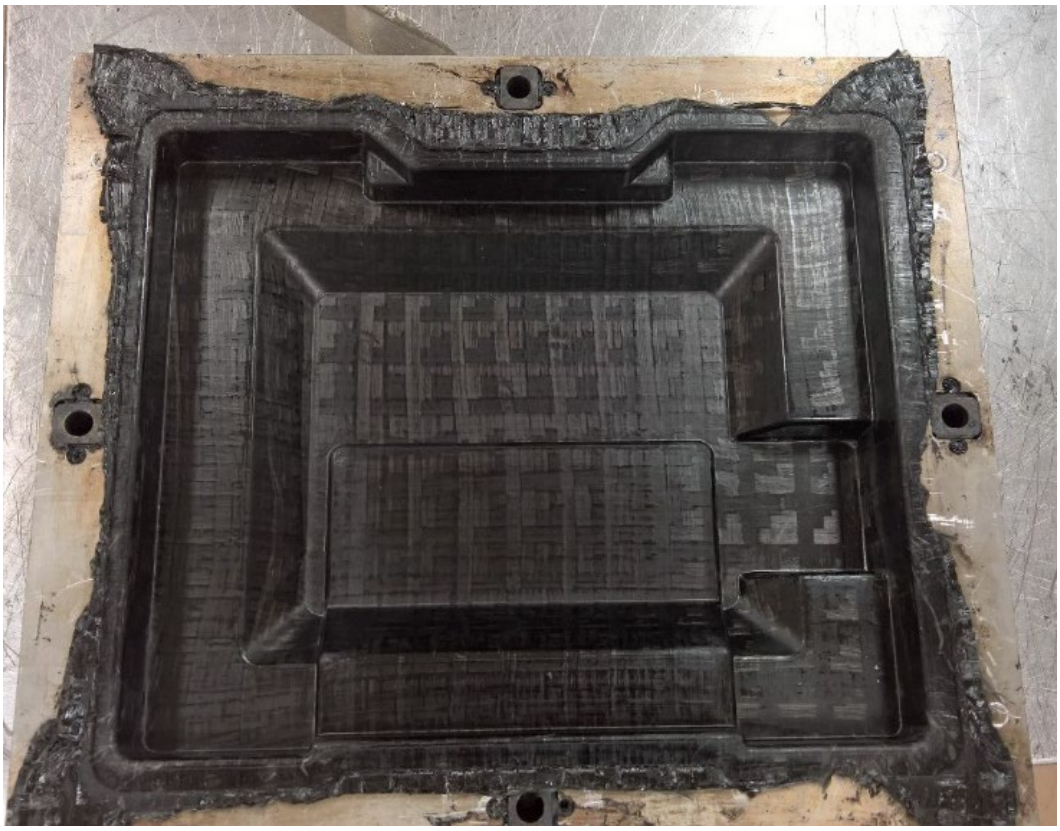

Figure 29. Molded Manta case in female mold section.

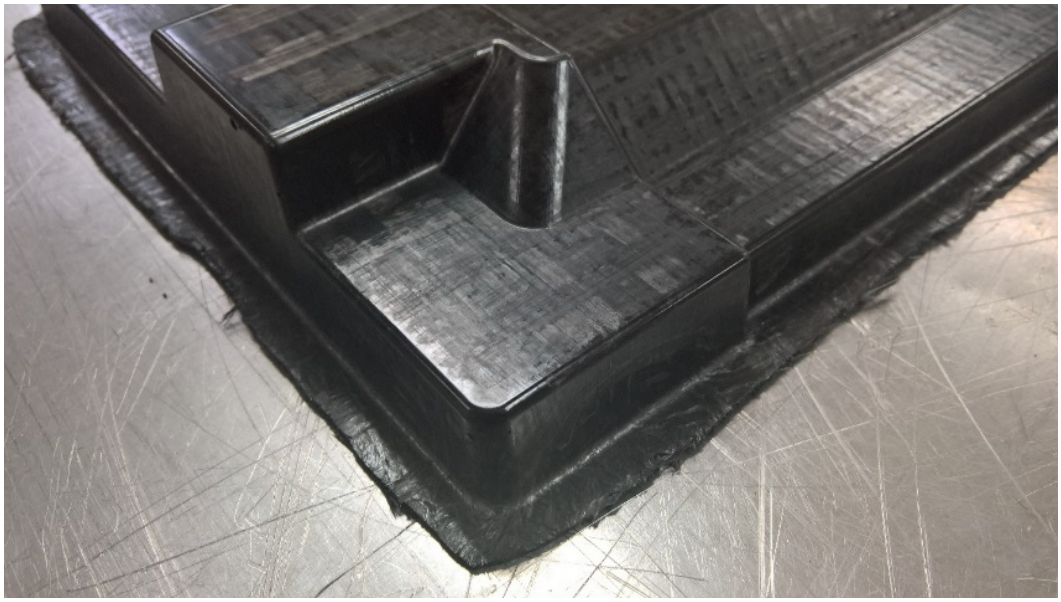

Figure 30. Demolded Manta case showing detail of corners.

5.8 Characterization of Manta laptop case

The complex geometry of the Manta laptop case provides a number of useful features for comparing the drapability of the RFF with the 2x2 twill and validating the simulation approaches for modeling the draping and forming of the RFF. There are two general modeling approaches

for predicting the fiber orientations and shearing angles of the sheet materials, geometric analysis and physics-based simulation. The geometry based analysis for this investigation was performed using the CAD software, CATIA V5-6R2017 from Dassault Systemes. CATIA provides several methods within its Composites Design workbench for analyzing the producibility of continuous fiber composites including the ability of the 2D preforms to conform to the given 3D surface and the resulting fiber orientations following the draping. In the geometric approach, the contours describing the fiber orientation are followed along the surface of the tool based on a predefined seed point and "rosette", or local axes with respect to the surface. This method does not account for the stiffness of the sheet material being draped or the manufacturing process used to conform the sheet to the tool surface. Figure 31 demonstrates the range of results predicted from this approach for varying seed points over the surface. The contour lines in the images correspond to the orientation following a single fiber or tow in the sheet. Blue regions indicate shearing angles between the warp and weft tows less than 15 degrees, yellow is between 15 and 30 degrees and red regions indicate shearing angles above 30 degrees. The results from the geometric analysis are dependent on the selection of the seed point, which is analogous to the first point of contact and constraint between the sheet and the tool.

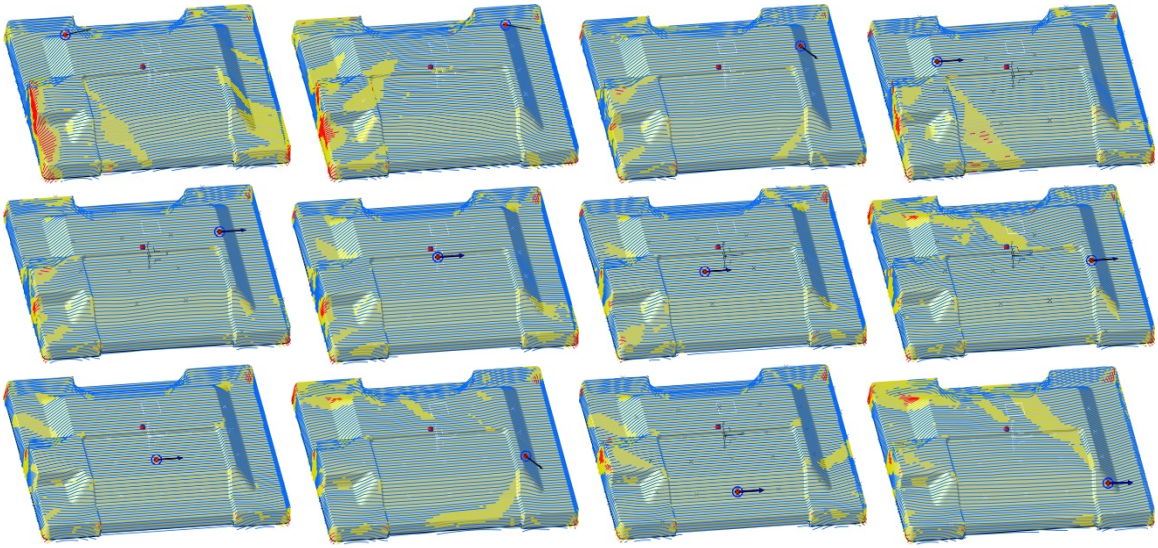

Figure 31. Manta lap top case fiber draping contour lines for varying seed points from CATIA drapability analysis.

As a first order analysis, the geometry based draping predictions are useful for identify regions in the geometry which are susceptible to deformations. Figure 32 illustrates a region in the geometry where multiple, counteracting right angle bends are present in the geometry. The geometry prediction from multiple seed points shows high shearing and deformation will occur in this region. This is observed in the manufacturing with both the RFF material (Figure 32b) and 2x2 twill (Figure 32c). It is important to note that both materials must deform to accommodate the complex geometry, however the mechanisms of this deformation are different between the RFF and twill. In the case of the RFF, the tows are permitted to slide relative to one another and a more gradual curve is present in the tows running horizontally with respect to the page. In the case of the twill, the mechanical interlocking produces more exaggerated kinking in the tows, as well as significant "opening" of the unit cell where large gaps develop between adjacent tows.

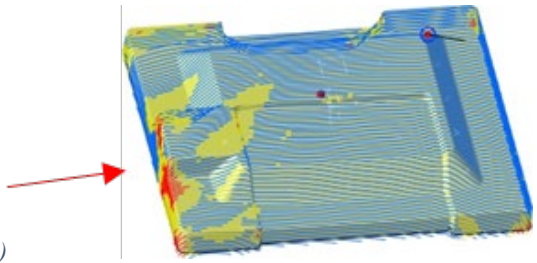

a)

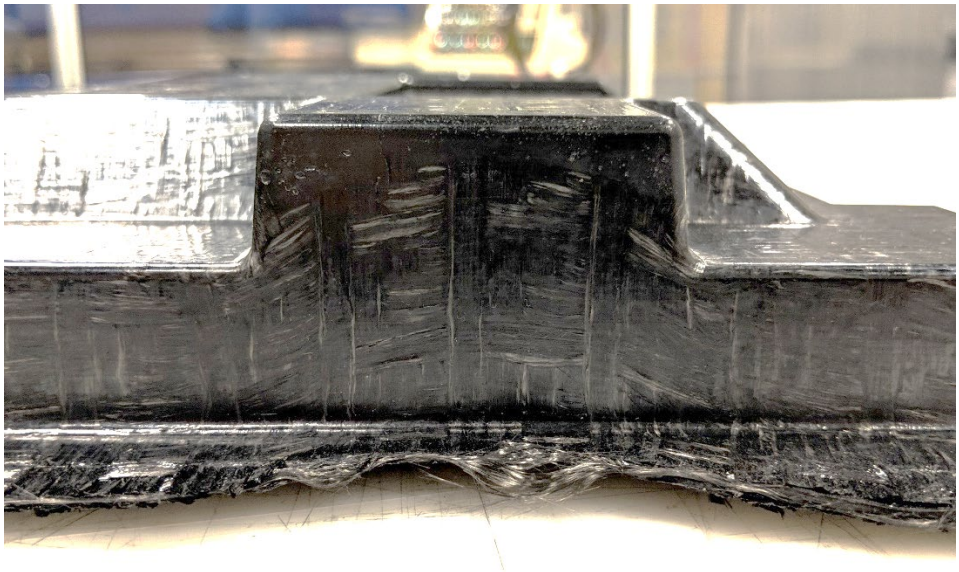

b)

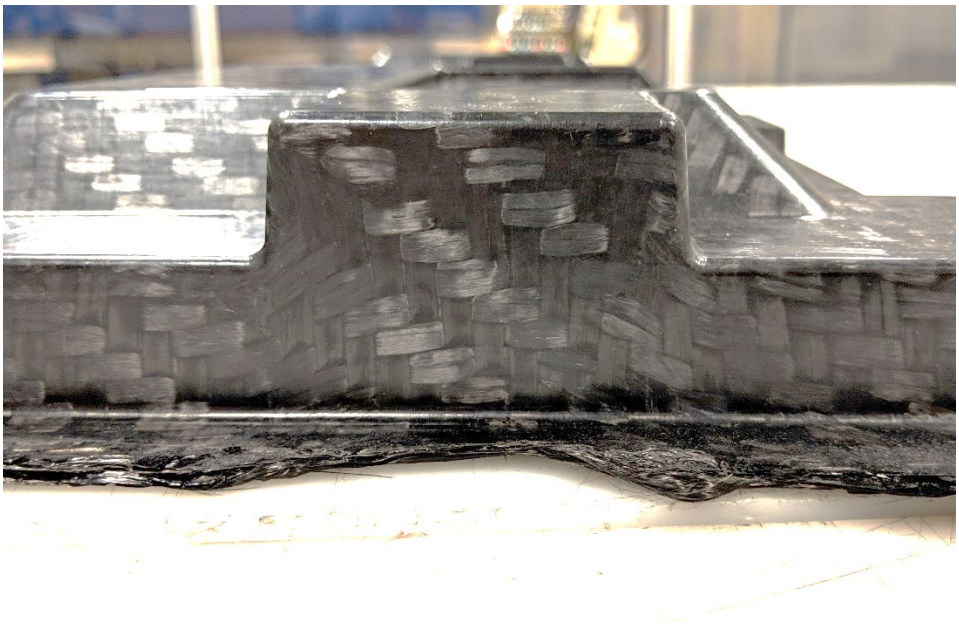

c)

Figure 32. Region of high predicted shearing from a) CATIA analysis and as manufactured with b) RF and c) 2x2 twill.

The geometric draping analysis can also produce erroneous results depending on the seed point as in Figure 33. With the seed point in Figure 33a, a high degree of deformation would be

anticipated in the offset region at the top center of the image, whereas Figure 33b does not predict this behavior. The manufactured specimens in Figure 33c and Figure 33d for both the RFF and 2x2 twill display only minimal deformation in this region. The challenging task for the engineer, from both a design and manufacturing standpoint, with this type of analysis is to be able to predict which of these two cases will be correct. The discrepancy between seed points is in part because the geometric analysis does directly account for the mechanical deformation of the sheet as it drapes and can thus miss out on physical phenomena that impact the draping and forming process.

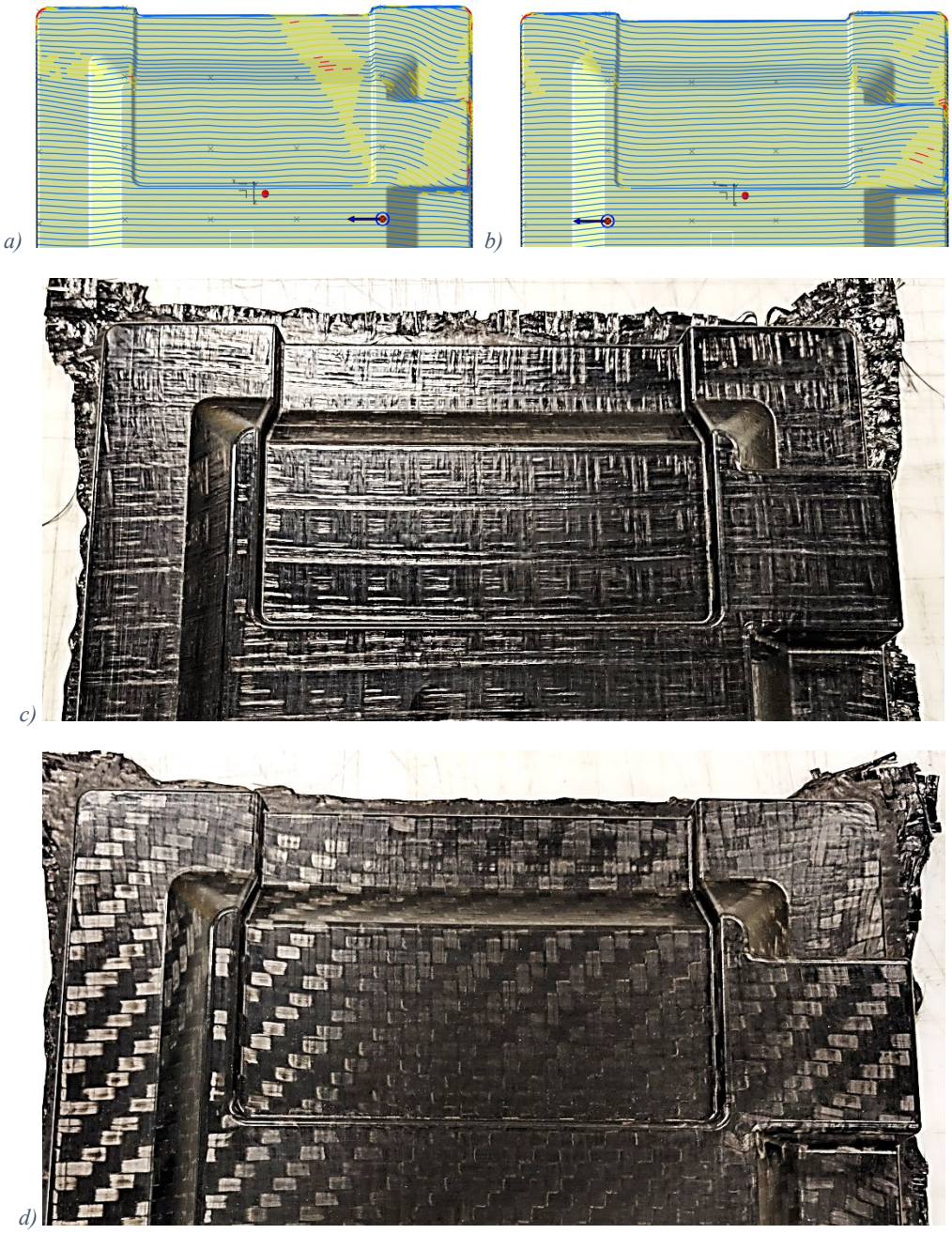

Figure 33. Comparison of seed point results from a,b) CATIA analysis and as manufactured with c) RFF and d) 2x2 twill

To account for the higher order phenomena that govern the forming process, particularly compression molding, a physics-based, finite element simulation is required. In this case, PAM-FORM from ESI Group is implemented to simulate the compression molding process. PAM-FORM is an explicit FEM solver, part of the PAM-COMPOSITES suite of software tools designed for composites manufacturing simulation. It relies on the same explicit solver as PAM-CRASH which has extensive use in the automotive industry for crash and impact simulations. The sheet forming process relies on much of the same physics modeling tools as high-speed impact simulation, e.g. contact modeling, large deformations, and energy control. PAM-FORM also includes support for the material behavior of composite sheet products, including the relationship between shearing angle and shear stiffness, thickness change in the material due to shearing, and material anisotropy. More details on the simulation of draping processes with PAM-FORM can be found in the report for Phase I of this project.

To simulate the compression molding process described in Section 5.7, the PAM-FORM model was created with tooling surfaces for the male and female surfaces of the compression tool and three RFF sheets placed between the tool surfaces to be molded. The female tool was held in place and a closing velocity was imparted on the male tool until the mold was completely closed. The set up for the simulation is shown in Figure 34. The material properties for the RFF blanks used in the analysis were taken from the characterization performed in Phase I using picture frame shearing, fabric bending, DMA analysis, and friction tests discussed in the Phase I report.

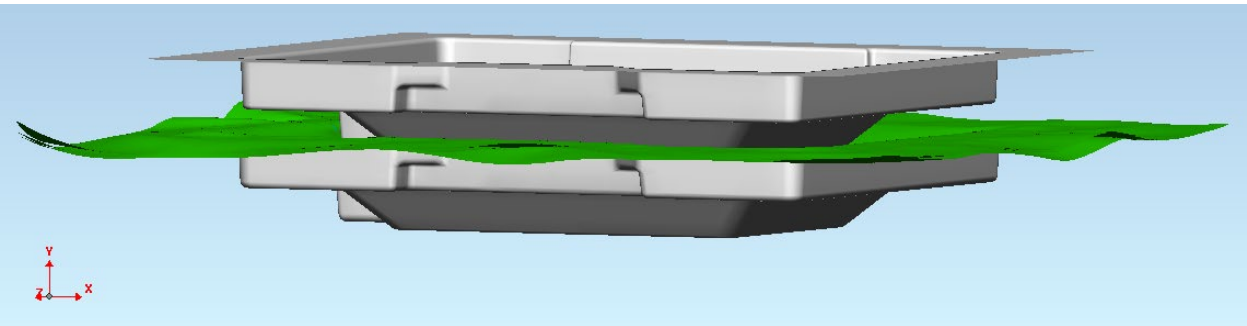

Figure 34. PAM-FORM model for Manta lap top case molding.

The predicted shearing angle and fiber directions from the physics-based analysis from PAM-FORM shown in Figure 35 highlights the same region as Figure 33. The physics-based approach in PAM-FORM does not predict that there will be significant shearing in the top center section of the geometry. This is more consistent with the observed behavior from the molding trials.

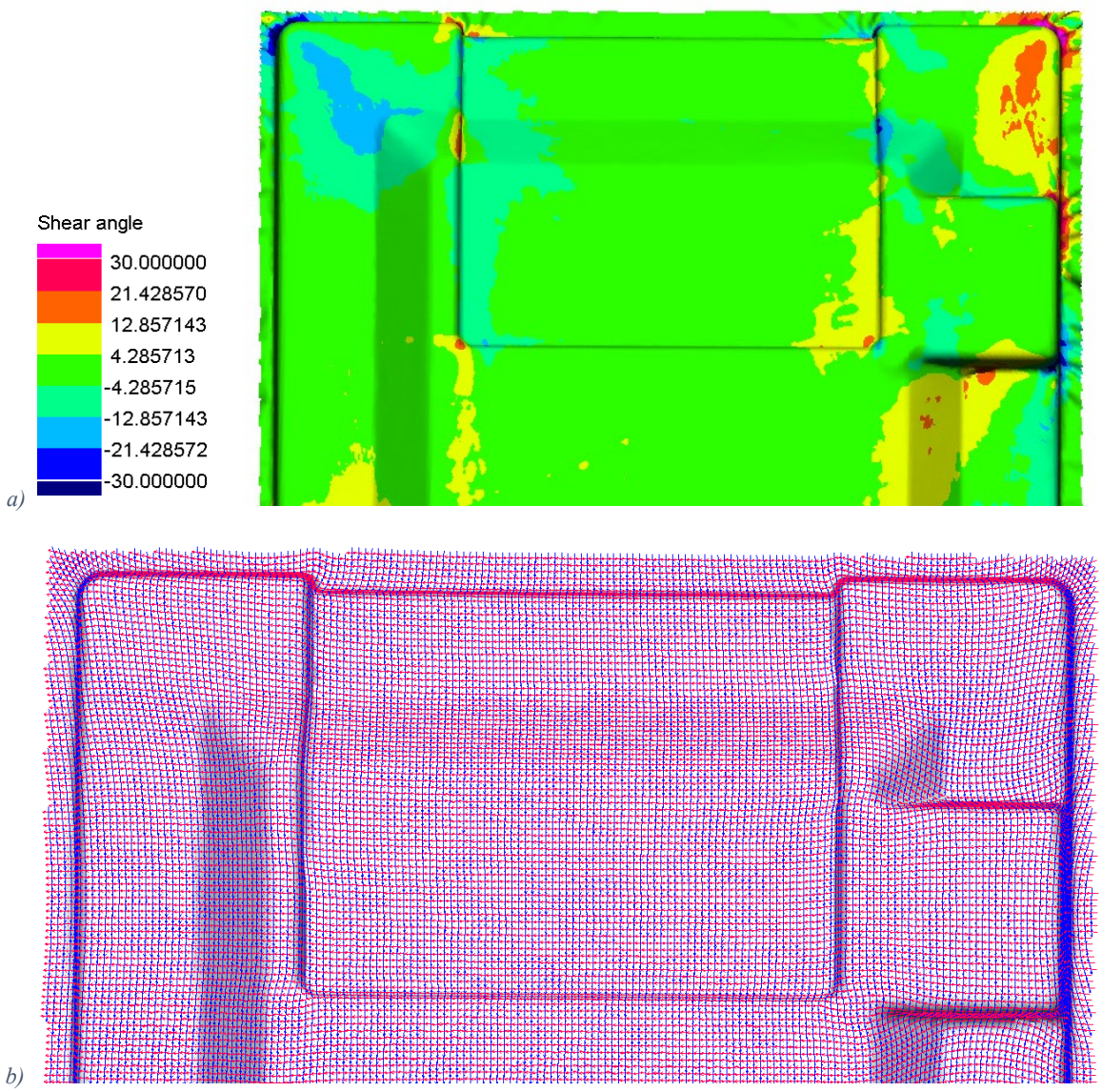

Figure 35. PAM-FORM prediction of a) shearing angle and b) fiber directions in Manta case region shown in Figure 33. Areas in Figure 35a shown in yellow and red should be used as a guide to find disturbed areas in Figure 35b.

Exploring further regions of the geometry shows good agreement between the fiber orientation predicted in the PAM-FORM analysis with the as-manufactured results. Figure 36 shows a corner region in the Manta case where three right angle curves meet at the exterior corner of the case and are located near a change in overall part depth. The tows must rotate significantly to accommodate this complex geometry. Figure 36c and d show the predicted fiber directions and shear angles from the PAM-FORM analysis. The shear angle at this location would cause the twill fabric to wrinkle and require significant deformation of the fabric and localized force application in the compression molding operation to close the two-sided tool. This could cause damage to the tool and result in failure initiation locations in the resultant part. The RFF also must undergo local fiber rotation to accommodate the curvature of the geometry, however, its construction does not have the propensity to wrinkle and should lead to a reduction in the localized force and out of plane sheet deformation. This is one of the proposed benefits of the

RFF process.

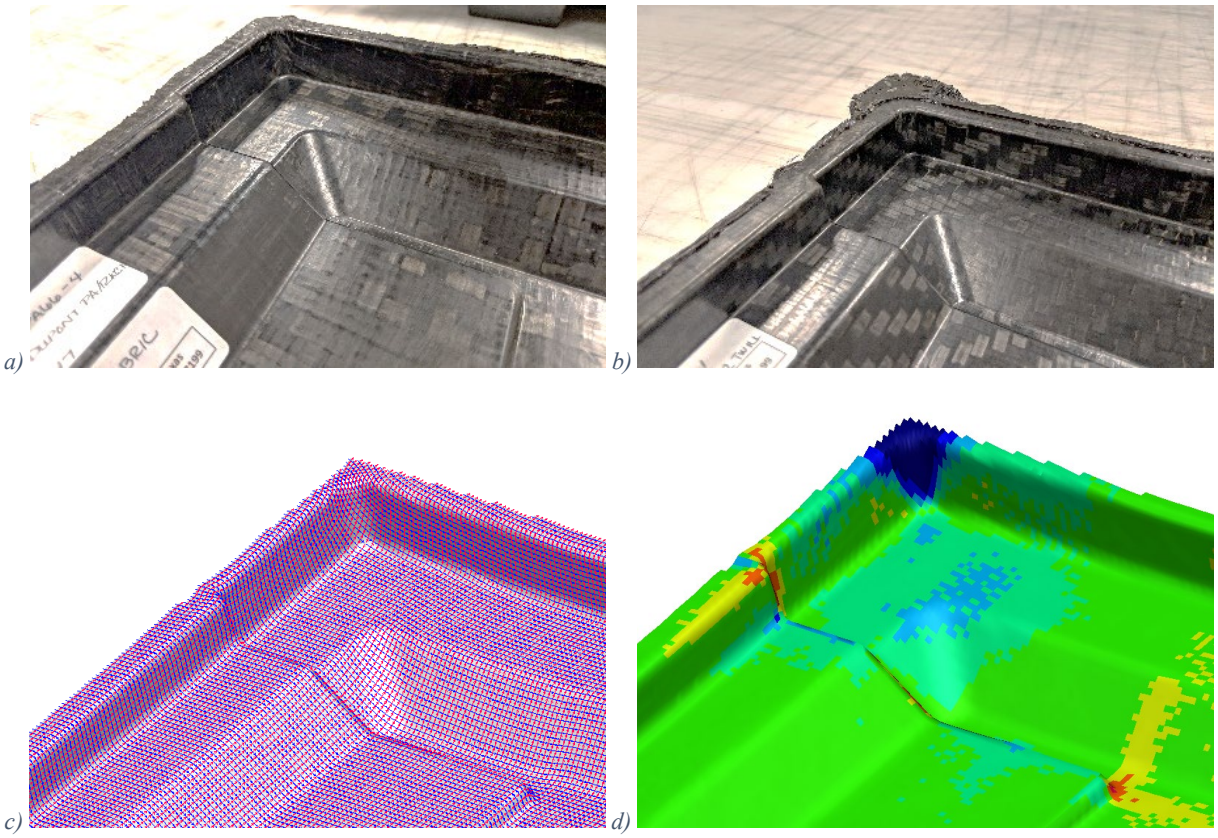

Figure 36. Rotations of tows near Manta case walls at the change in part depth for a) RFF and b) twill fabric with predicted c) fiber direction and shear angle PAM-FORM analysis. Yellow and red colorations indicate areas of higher tow rotation, and should be used as a guide to find disturbed areas in Figure 36c.

Figure 37 shows the region in the Manta case where the vertical wall in the part has a local change in height. In the RFF and the 2x2 twill, this induces an arched shape in the tows to follow the part topology. In the RFF molding in Figure 37a, the curvature of the tows varies gradually over the raised wall region as shown by the superimposed red line in the images. For the twill fabric in Figure 37b, the interlocked structure of the fabric induces more localized sharp curvature in the tows to follow the deformed path. These general paths are accurately predicted in PAM-FORM in Figure 37c.

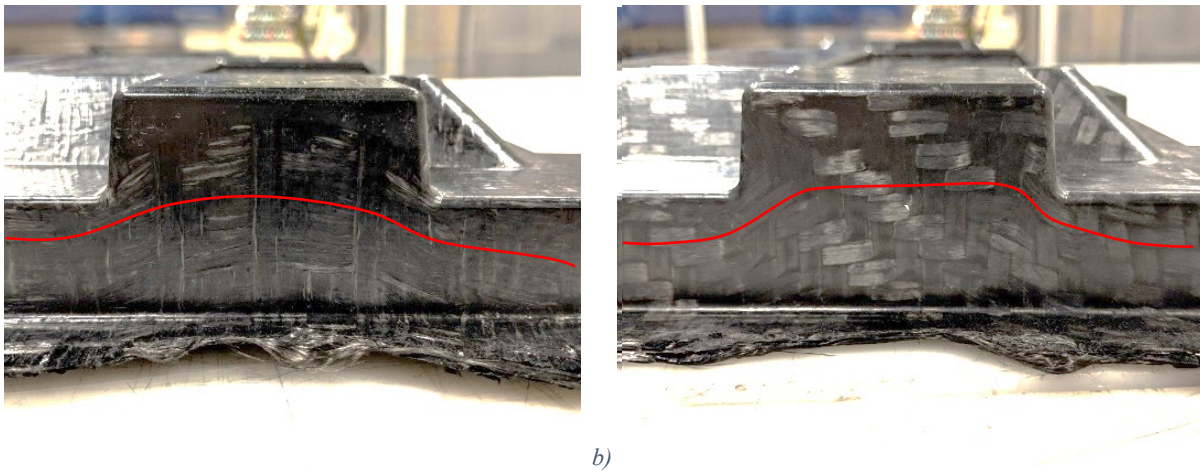

a) b)

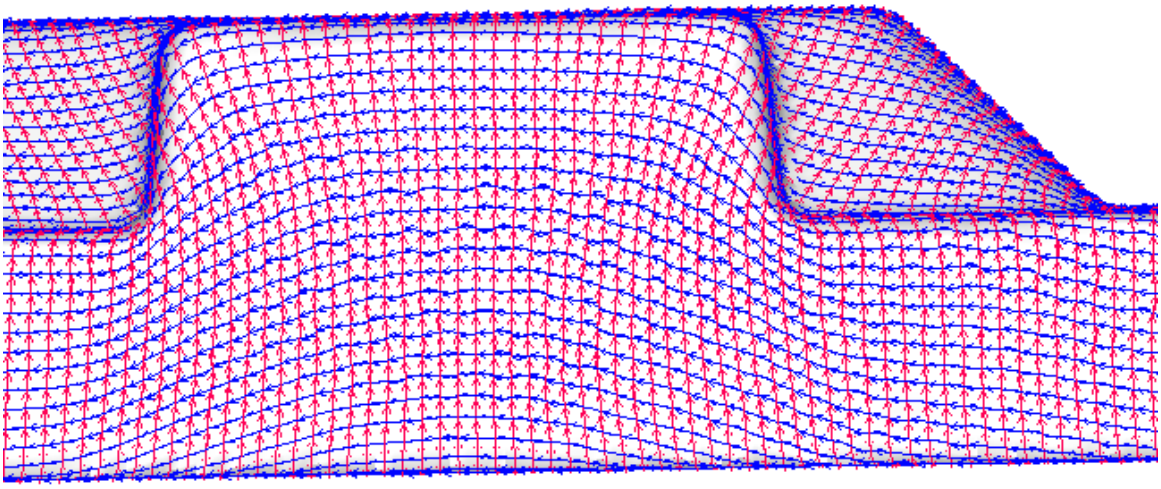

c)

Figure 37. Tow rotations at extended vertical wall for a) RFF, b) twill fabric, and c) as predicted in PAM-FORM. The red line in a) and b) has been added as a guide to the reader for comparing the tow paths in the RFF and twill-based materials.

The region adjacent to the vertical wall above highlights a variation between the behavior of the RFF and twill fabrics regarding their overall fiber directions. Figure 38a shows the RFF molding where the tows at the corner are orthogonally aligned and do not display significant deformation. In contrast, the twill fabric molding in Figure 38b demonstrates significant warpage of the unit cell and misalignment of the tows. The PAM-FORM molding simulation in Figure 38c shows minimal deformation in the fiber direction predicted in this region. One explanation for this behavior is that the lack of interlocking between tows in the RFF allows the unit cell mesostructured to deform internally to respond to the forces on the blank while the interwoven twill must deform with more significant macroscopic rotation and deformation.

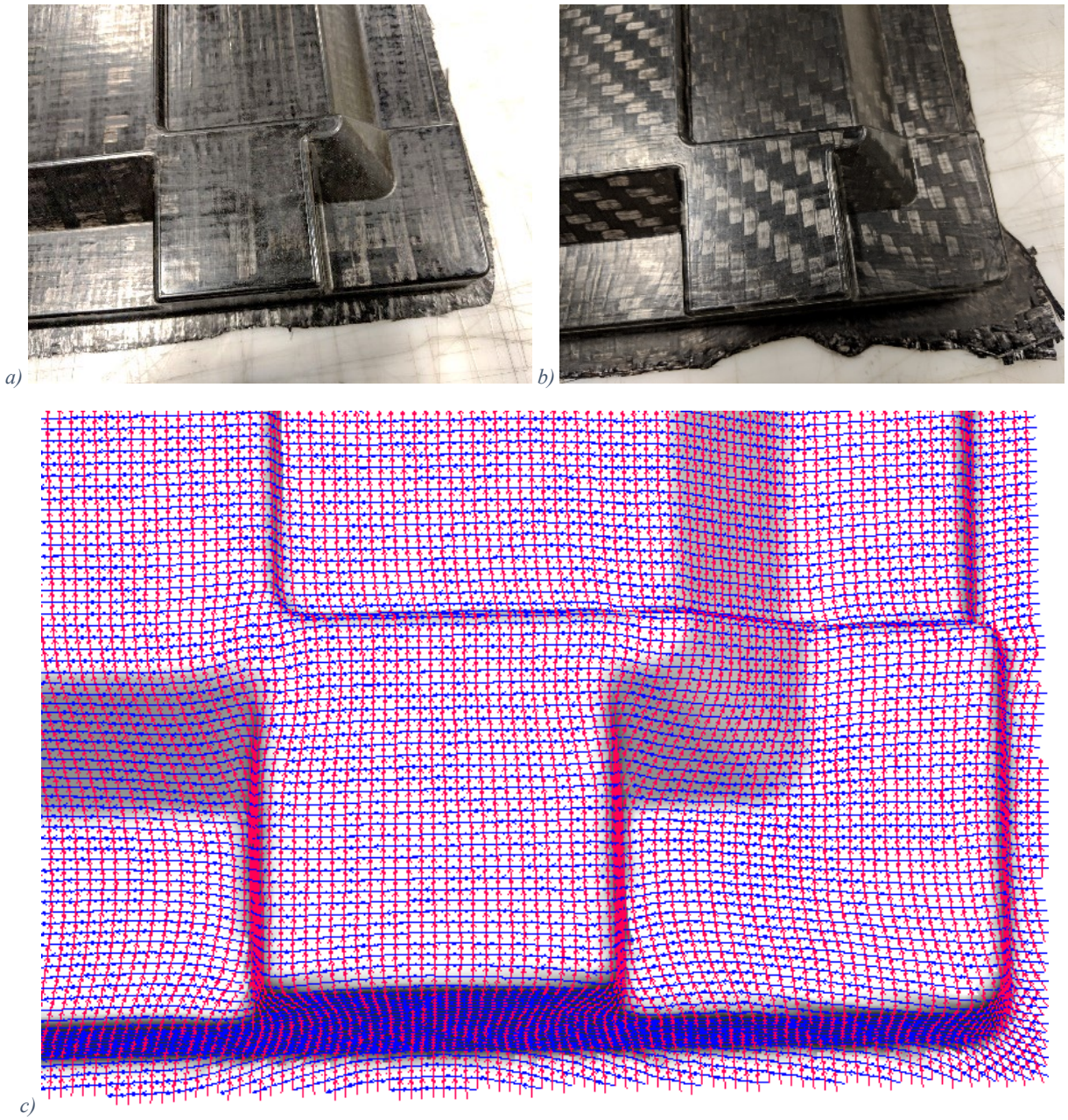

Figure 38. Mesostructure distortion in corner for a) RFF showing orthogonal tows and b) twill fabric with stretched and shear unit cells.

Comparing the fiber direction predictions from PAM-FORM with the as-molded RFF constructions provides reasonable validation of the physics-based molding analysis approach. The ability to accurately predict fiber orientation and fabric shearing is critical for predicting in situ mechanical properties of the anisotropic fabric. The qualitative trends from the molding are mostly captured in the simulation, with some higher-order effects in the mesostructured and local deformation of the unit cell not completely captured. This would require a higher-fidelity multiscale modeling approach as the size scale of the fabric unit cell is larger than the element size required for the forming simulation, requiring multiple elements in the forming simulation to

represent a single unit cell. This type of simulation does not currently exist commercially, and it is not clear that it would significantly improve the design effectiveness of the simulation, particularly for directional design.

5.9 Fabrication of automotive seatback

As noted in the "Lower Control Arm Design" section, after dismissing the LCA as an attractive target for fabrication, the Team decided on a molded automotive seatback as a demonstrator part for this technology. An already-existing oil-heated aluminum mold was provided by Uday Vaidya (U. Tennessee), shown in Figure 39. The mold was mounted in a Williams and White HPU 40 press, and the mold attached to a recirculating oil heater capable of a 280C peak temperature. Based on a computer model of the mold, the Team at Purdue used CATIA to virtually flatten the composite to define the dimensions that would be required for the RFF preform. The draping analysis shown in Figure 40 uses a geometry-based algorithm to predict the deformation of a continuous fiber tape or fabric as it conforms to complex, three dimensional shapes. This analysis is critical for assessing manufacturability and evaluating regions in the part geometry that are susceptible to excessive fabric deformation and wrinkling. The software is also capable of using similar algorithms to recover a two-dimensional "flattened" outline of the sheet dimensions required to yield the desired three-dimensional shape. This flattened geometry for the seatback is shown in Figure 41. The maximum dimensions of this preform are 620 x 720 mm.

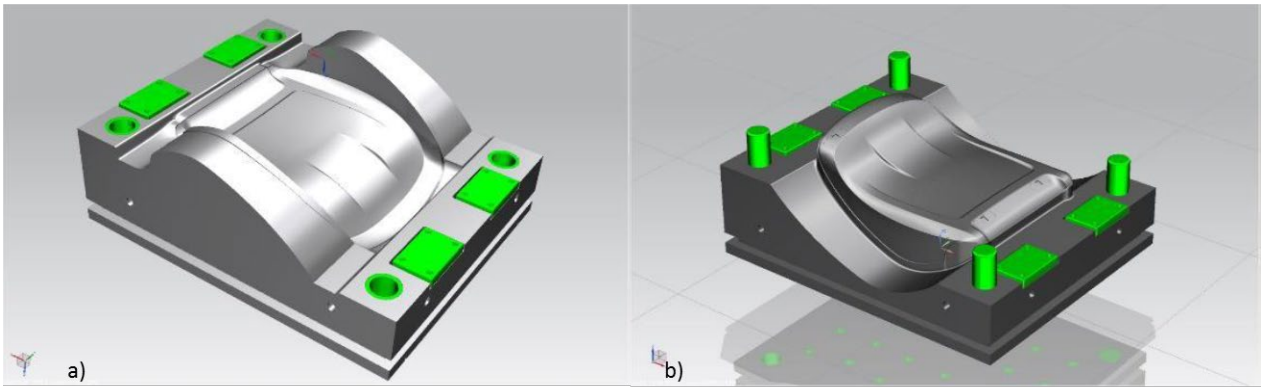

Figure 39. Seatback mold showing a) upper and b) lower portions.

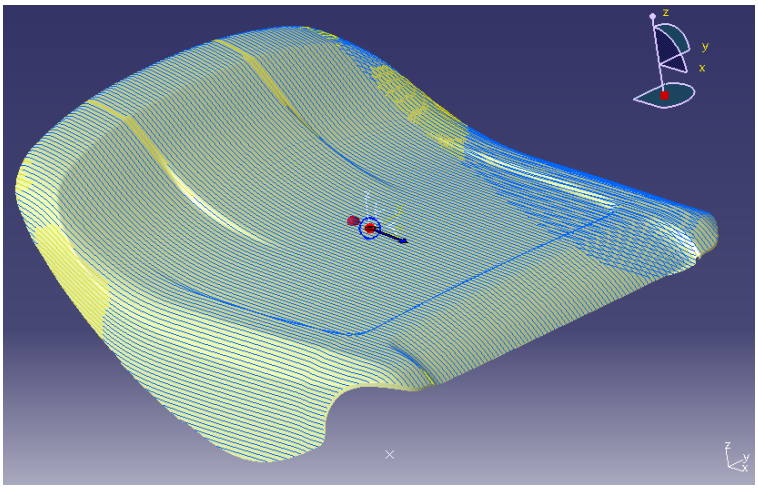

Figure 40. Producibility analysis from CATIA for the seatback tool. (Yellow lines indicate shearing angles greater than 10 degrees, blue indicate less than 10 degrees.)

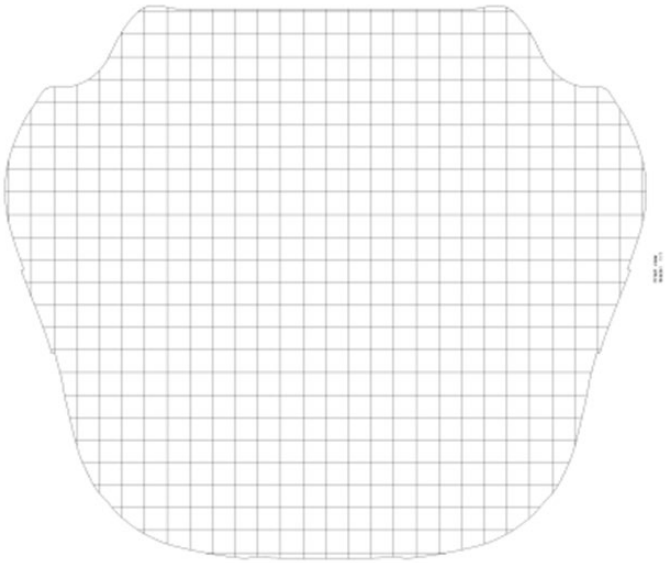

Figure 41. "Flattened" seatback composite, where each inscribed square is one by one inch

Based on the dimensions in Figure 41, Automated Dynamics Corporation (ADC) produced a total of 24 RFF panels using AFP. As with previous fabrics made at ADC, the coated tows were laser-anchored to a thermoplastic tape frame only at the tow ends and were allowed to slip relative to one another in the remainder of the area. Due to the shape of the intended preform being so close to rectangular, the Team decided to produce rectangular fabrics rather than make a shape that was closer to net shape. In addition, to reduce machine set-up time, the panels were made at ADC at a double width that were subsequently cut in half prior to molding. The mold and the fabrics were then sent to Valley Enterprises, Inc, part of the Gemini Group, in Ubley, MI.

In parallel with the fabric production, the Valley team bent a steel bar, roughly 1.5” wide by one eighth inch thick, into the shape of the preform perimeter, henceforth referred to as a “guide”. To prepare the preform, 8 layers of fabric were laid on a one eighth inch thick stainless steel sheet.

The steel guide was then placed on top of the fabric stack (Figure 42), followed by another stainless steel sheet.

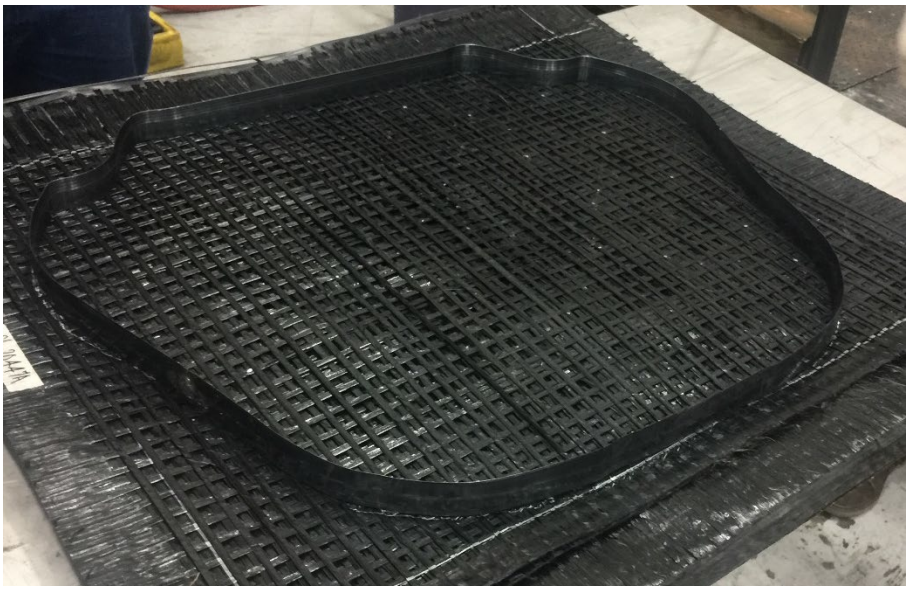

Figure 42. Preform shaping guide in position on fabric preform.

Following assembly of this stack, the entire assembly was inserted into a press that was preheated to 280C and pressurized to 1000 pounds of force. After waiting for 15 minutes, the pressure was removed and the stack was taken out of the press. The stack was then cooled, the steel cap removed, and the fabric/guide moved to a plastic covered table. At this point in the process, the preform was cut out of the rectangular fabric, and the guide was removed, resulting in the shape in Figure 43. During the cutting operation, there were very few tows that became loose, indicating that the RFF was partially consolidated in the area under the guide, as was intended. Loose tows were reattached to the preform by heating the end of the tow with a soldering iron.

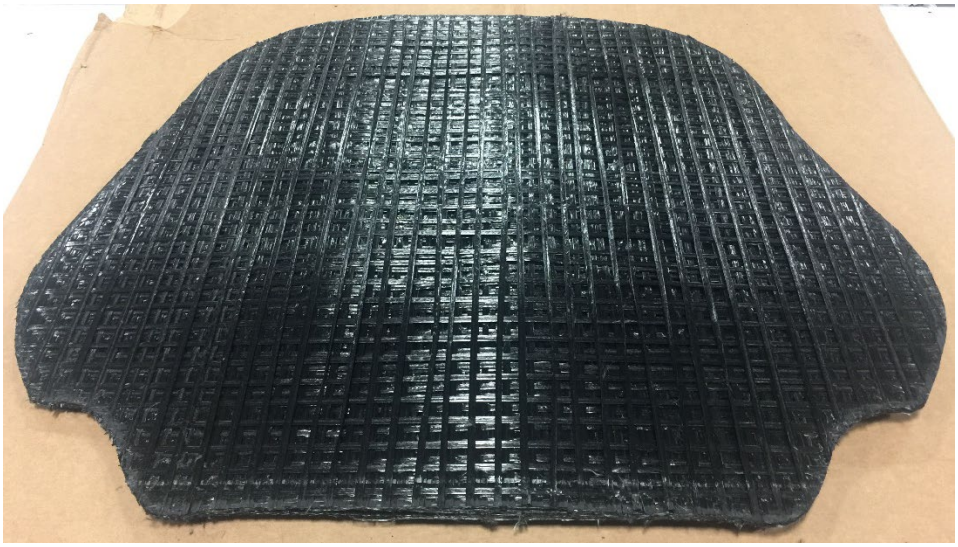

Figure 43. Eight-layer fabric preform after cutting to shape.

In the final stage of processing, the preform from Figure 43 was placed into the mold that was preheated to 280C in a Williams and White HPU 40 press, after which the lower portion of the mold was raised until a pressure of 830 psi was reached (Figure 44). The pressure was maintained for 120 minutes, at which point the mold was cooled to 120C over 14 hours to ensure that the polyamide was fully solidified. At that time, the mold was opened and the seatback was removed, as shown in Figure 45.

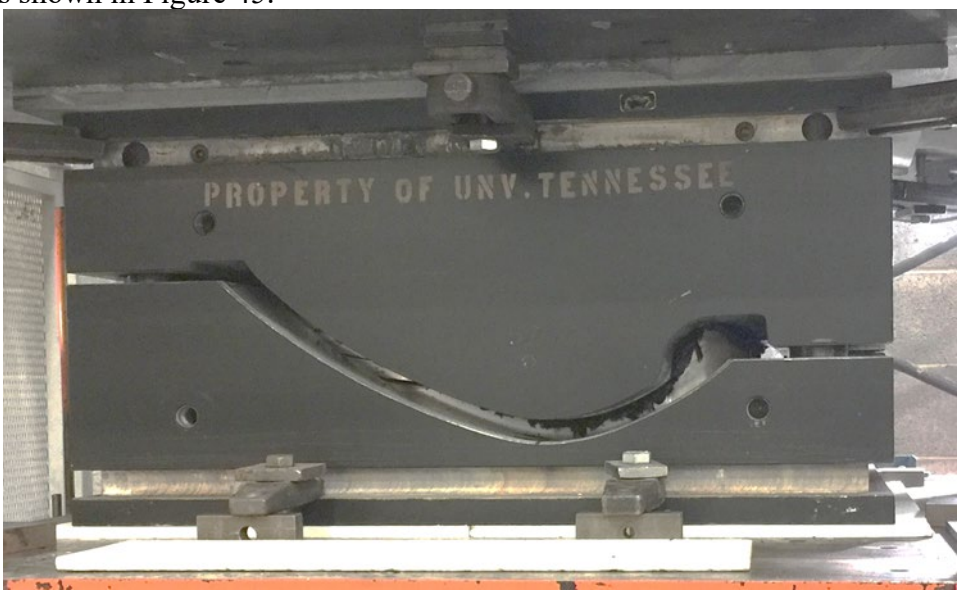

Figure 44. Closed seatback mold showing flashing over the shear edge of the mold.

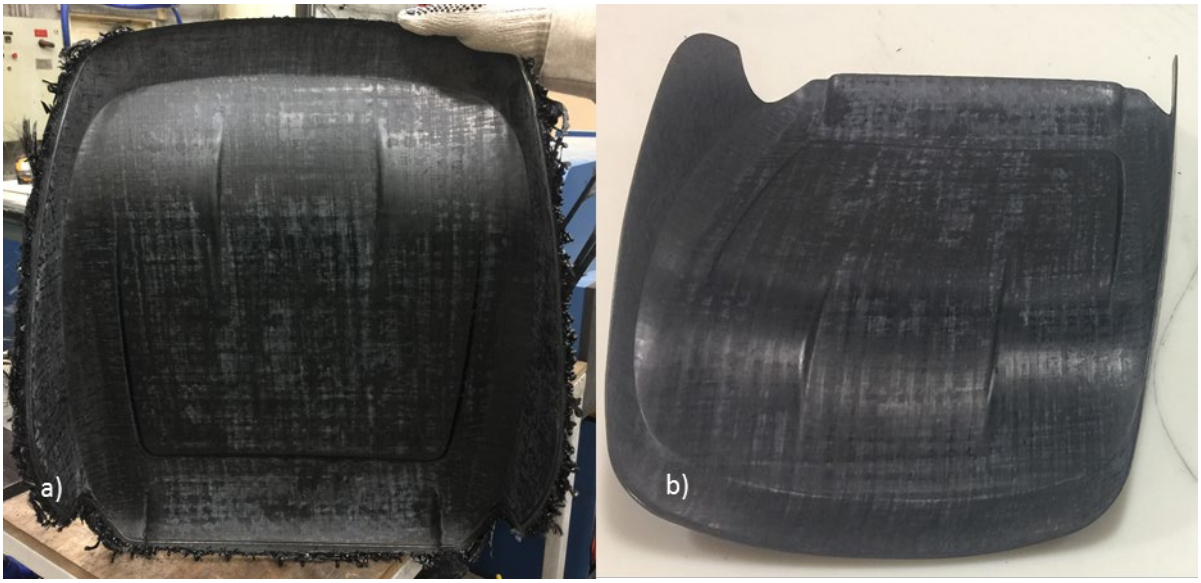

Figure 45. Seatback a) after molding, and b) after flashing removed.

The process described above was used to make a total of 3 seatbacks

The team understands that this consolidation process chosen for this program was slow, and therefore capital intensive. However, there are processes that significantly reduce residence time in the mold. The most attractive of these is stamping, where the thermoplastic preforms are

preheated with infrared radiation to a temperature above their glass transition, then stamped in a mold that is below the glass transition temperature. This process is very fast and leads to a very high productivity. An example of this process can be viewed at:
https://www.youtube.com/watch?v=h6if37hN6OM

5.10 Characterization of automotive seatback

The primary characterization effort for the seatback focused on investigating the microstructure of the molded part using microscopy and computed tomography imaging. The seatback molded in Section 5.9 was sectioned into multiple specimens for imaging as in Figure 46 using a hand saw. The regions labeled A-D were extracted for 3D CT imaging whereas E-H were extracted for 2D microscopy.

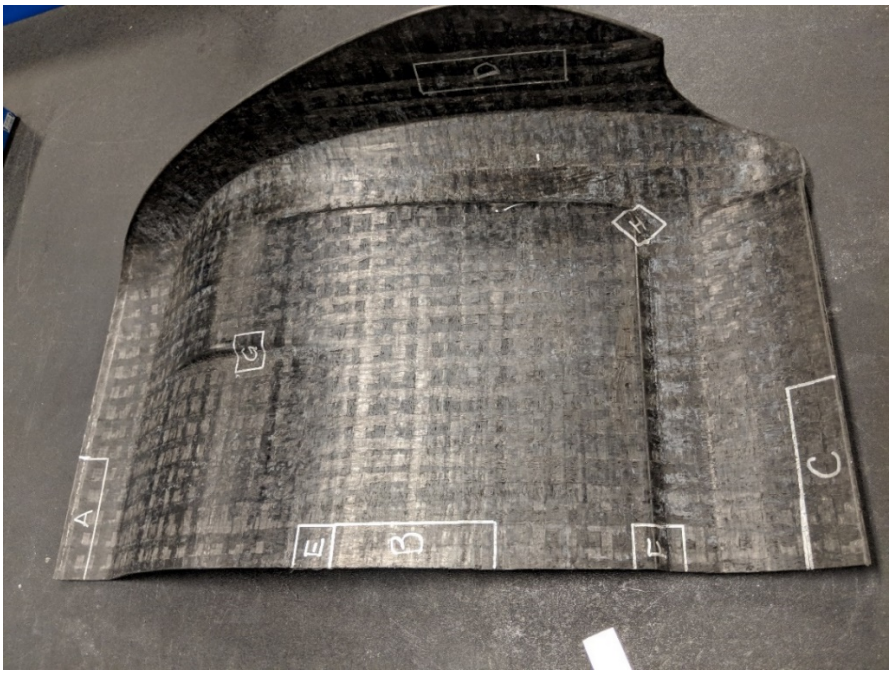

Figure 46. Sectioning for seatback imaging.

The CT imaging was performed on a Zeiss Xradia 510 Versa High-Resolution 3-D X-ray Tomography Microscope System located at Purdue University. To capture a reasonable volume of the specimens, the resolution of the voxels in the CT images was 37 microns. The CT processing method produces images through internal density variations of the scanned volume. The density of the carbon fibers is around 1.8g/cm^3 and the polyamide is around 1.15g/cm^3 which creates a contrast between the two materials in images where the fiber can be fully resolved. For lower resolution CT images, variations in local fiber content can be observed through the varying shades of gray in the image. Voids and resin rich areas will both present as dark regions in the image, and there can be ambiguity as to whether dark regions are true voids, or resin-filled regions that do not have significant fiber content. As such, these regions are both referred to as discontinuities and the nature of the discontinuity is up for interpretation. The primary goal of the CT imaging is to investigate the internal deformation of the RFF unit cells during molding and identify discontinuities, which can degrade mechanical properties in the part. While the resolution is larger than the diameter of an individual carbon fiber, the imaging

method is still able to identify these features.

The four specimens were mounted to a single fixture and scanned simultaneously. The 3D representation of the voxel image was processed to view slices within the specimen. Figure 47 shows 2D sections from the CT image from a top-down view showing the in-plane behavior of the RFF near the top edge of the seatback. There is some distortion of the unit cell out of plane due to the curvature in the part, but the general topology of the RFF is still discernable. The three images in Figure 47 are from sections near the top, middle, and bottom of the specimen. The relative location of tows within the unit cell does remain intact through the thickness of this specimen, indicating that the fabric is stable in this location.

a)

b)

c)

Figure 47. Top-down CT Images from top of the seatback (Location A) at the a) top surface, b) midplane, and c) bottom surface.

The first image in Figure 47a, taken near the top of the specimen, shows little distinction between adjacent tows, indicating that the relative density remains consistent throughout the slice and there are minimal resin rich areas and/or voids. The interfaces between tows are more pronounced in Figure 47b and c, and additional dark regions are present within the specimen, indicating that there are regions where the resin did not uniformly impregnate the tows throughout the structure. This behavior is also demonstrated in Figure 48 showing a cross-sectional view of the same specimen. Contiguous black regions are present in the specimen, which indicate the presence of voids where it is likely that air was entrapped in the molding process and is unable to escape.

a)

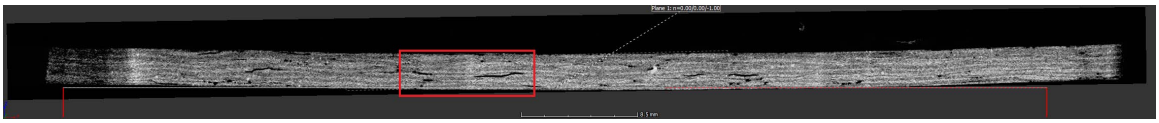

b)

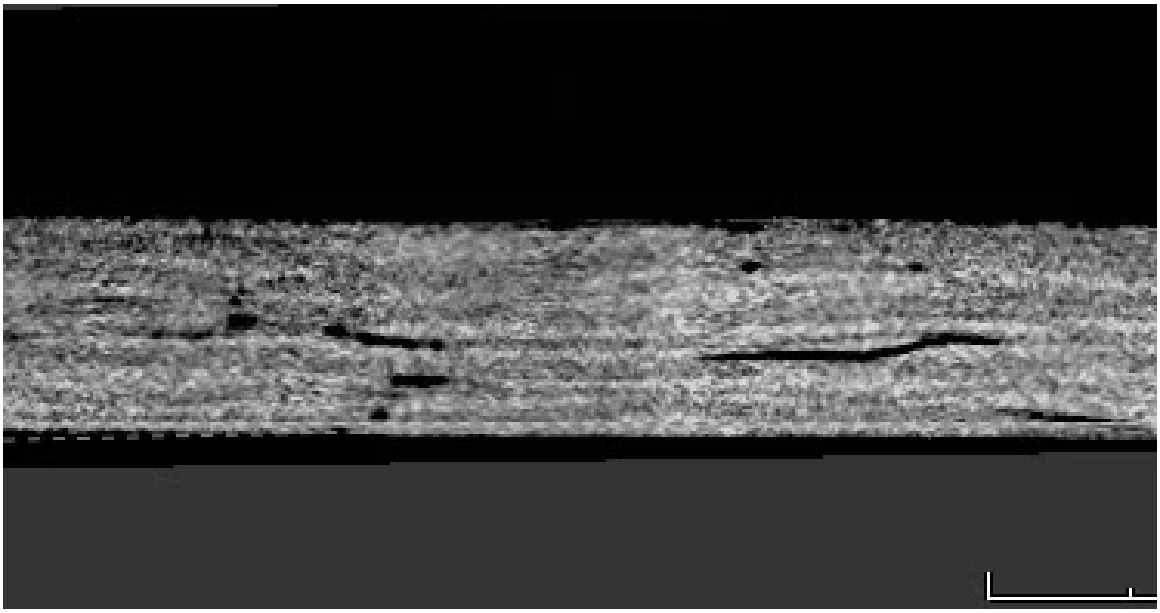

Figure 48. Cross sectional view of specimen from top of seatback (Location A) with a) full specimen and b) enlarged view.

Top-down images from the CT scan of the specimen extracted from the middle of the seatback are shown in Figure 49. The dark regions in the images indicate that there are voids in the specimen where the resin does not completely penetrate the fiber tows. The voids in the specimen taken from the middle of the seatback are less consistent in shape, in contrast to the longer, thinner voids from specimen A in Figure 47. A possible interpretation of this behavior is that the voids present in Figure 49 represent voids that form between successive plies of the RFF in the through thickness direction, and the long, thin voids in Figure 47 are formed either between adjacent tows in the same plane, or within the internal region of the coated tows that arises from the partial impregnation process. The extent of the voids in specimen B can be seen in the cross-sectional view in Figure 50, which was extracted from the middle of the specimen looking along the cut edge of the seatback.

a)

b)

Figure 49. Top-down CT Images from seatback middle (Location B) at the a) top surface and b) midplane surface.

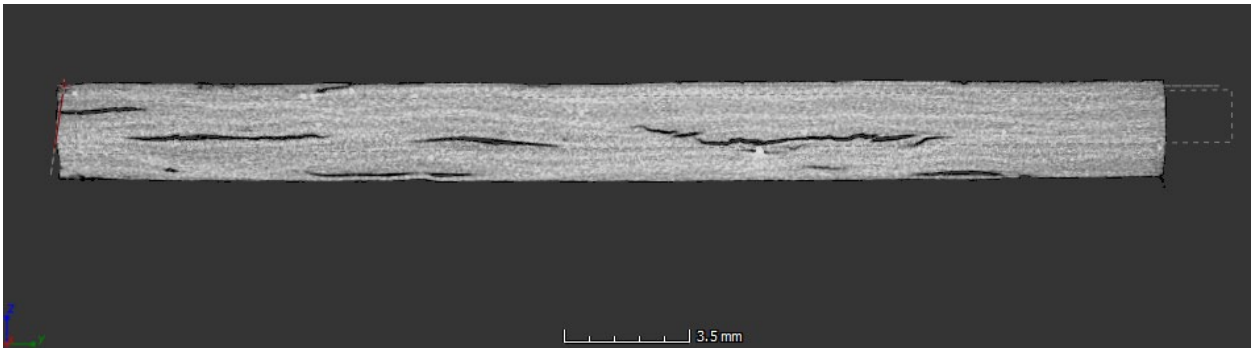

Figure 50. Cross sectional view of specimen from middle of seatback (Location B).

The specimen extracted from the bottom of the seatback at Location C has significant curvature as seen in Figure 51. This presented challenges in extracting planar slices from the CT scan for the top-down view included in Figure 52. There is also a significant amount of in-plane deformation of the unit cell at this location where adjacent tows within the RFF unit cells move with respect to one another and the tows rotate in plane. This specimen also exhibits a combination of the long, thin discontinuities and the amorphous discontinuities observed in the

previous specimens.

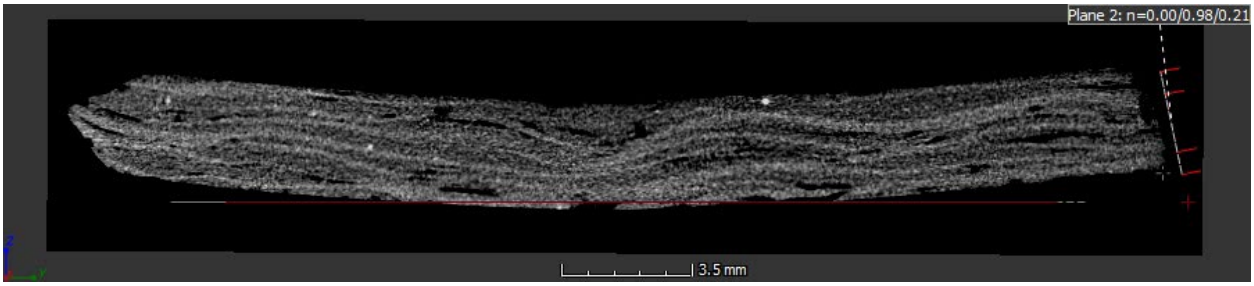

Figure 51. Cross sectional view of specimen from bottom of the seatback (Location C)

a)

b)

Figure 52. Top-down CT Images from bottom of the seatback (Location C) near the a) top surface and b) bottom surface.

Figure 53 shows the top down images from the CT scan of the specimen extracted from the side wall of the seatback, Location D. There are some discontinuities visible in the slice taken near the top surface of the specimen, but the slices from the middle and bottom of the specimen have much fewer discontinuities than the previous specimens. This is somewhat counterintuitive as the near-vertical configuration of the side wall with respect to the mold closing direction would

be expected to result in lower consolidating pressure on the material and a higher propensity for voids. This does not appear to be the case based on the results of the CT images. There do, however, appear to be some surface effects arising from the molding condition where Figure 53a does show the presence of significant discontinuities near the surface.

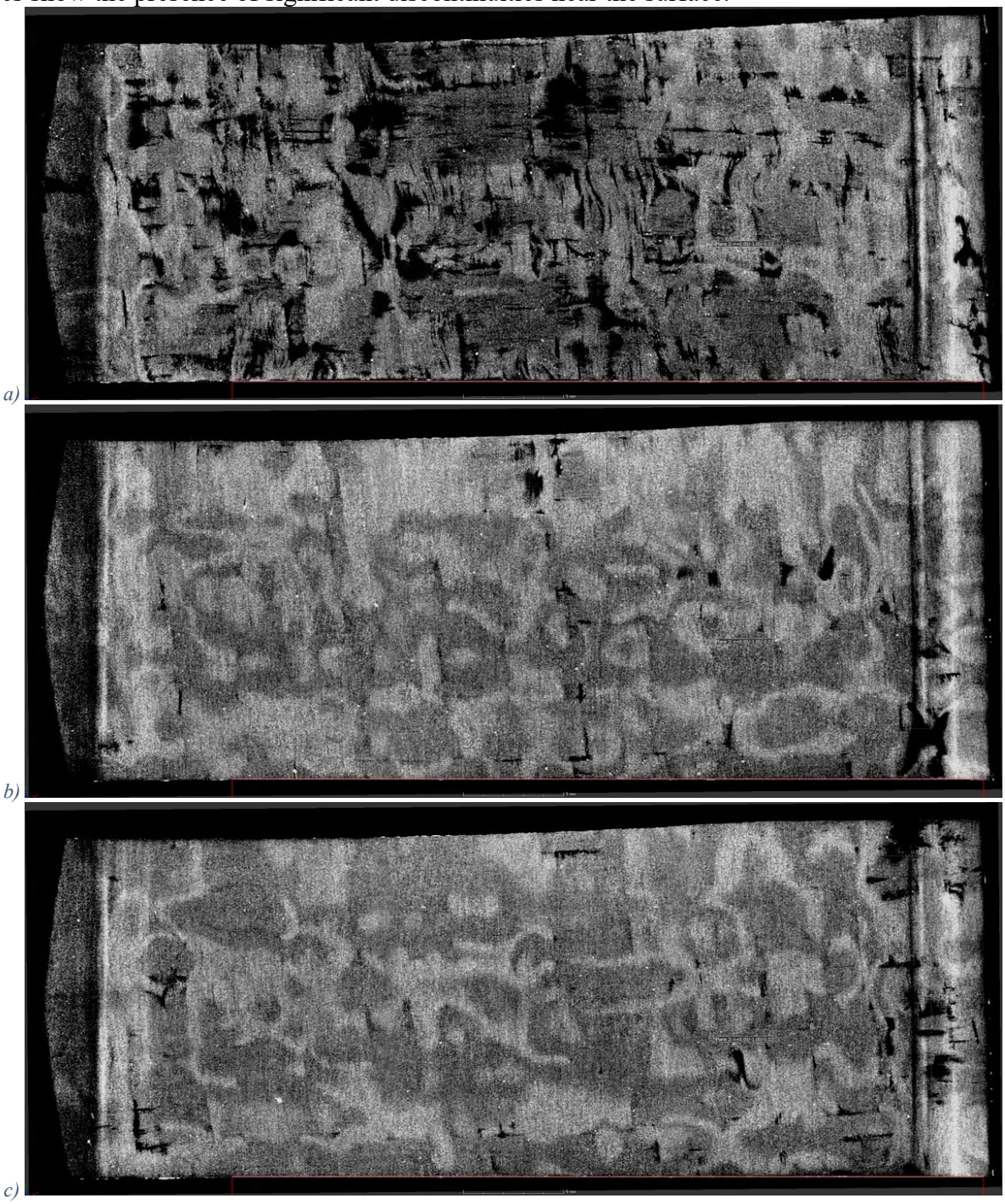

Figure 53. Top-down CT Images from side of the seatback (Location D) near the a) top surface and b) bottom surface.

In addition to the CT imaging, four of the specimen regions were investigated using 2D microscopy on sections which were cut from the seatback, mounted in resin, polished, and

analyzed using a Leica DMI5000M microscope with an automated stage. The automated stage permits the instrument to capture an array of images and automatically combine them into one, allowing a larger region of interest to be observed at a high resolution. The specimens are each an inch wide, taken from regions with various geometrical features, and the moving stage permits the entire area to be imaged at high enough resolution to see individual fibers.

Specimen E in Figure 54 represents a similar region in the seatback as Specimen B from the CT images. In this case, the micrographs help the interpretation of the discontinuities that were ambiguous from the CT. The micrographs have similar color scale as the CT images, in that the fibers are white, voids are black, and the resin is a dark gray in between. The micrographs have distinct striations indicating the layers of the RFF material. While the fiber are not entirely perpendicular or parallel with the image axes, the lighter regions indicate layers with the fibers running mostly across the image and the darker have fibers oriented into/out of the page. Figure 54 also includes both resin-rich regions and true voids. The presence of voids does indicate that air is entrapped in the part during the molding process either due to localized lack of consolidation pressure or premature solidification of the material creating an impermeable barrier for the air pocket. The resin-rich areas occur due to uneven impregnation of the resin into the fiber, which can be expected from the coated tow process. In general, the resin does penetrate the fiber tows homogenously, with only minimal localized regions of high resin concentration.

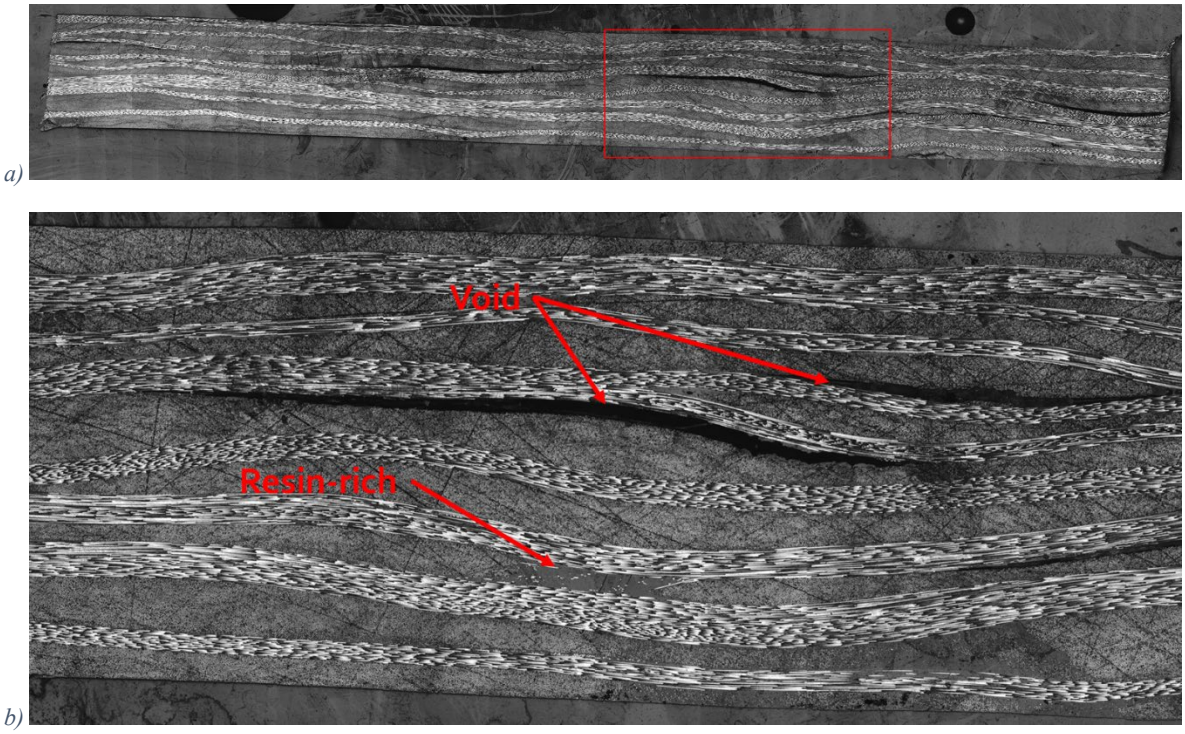

Figure 54. Micrograph of specimen extracted from Location E with a) full specimen and b) enlarged view.

Specimen F was extracted near the middle of the seat back at a location where the material undergoes and "S" type bending in the tool. Slight mismatching of the tooling radii to the thickness of the material and localized pinching of the material can create uneven pressure in these regions. The dark region in the left side of Figure 55a is likely due to damage in the

specimen extraction process. The region highlighted in Figure 55b shows localized resin-rich regions and cracks in the material at the bending location. The black crack near the mid plane of the specimen at this location could either be a product from the molding process, or formed due to stresses observed in handling the material for cutting the specimen.

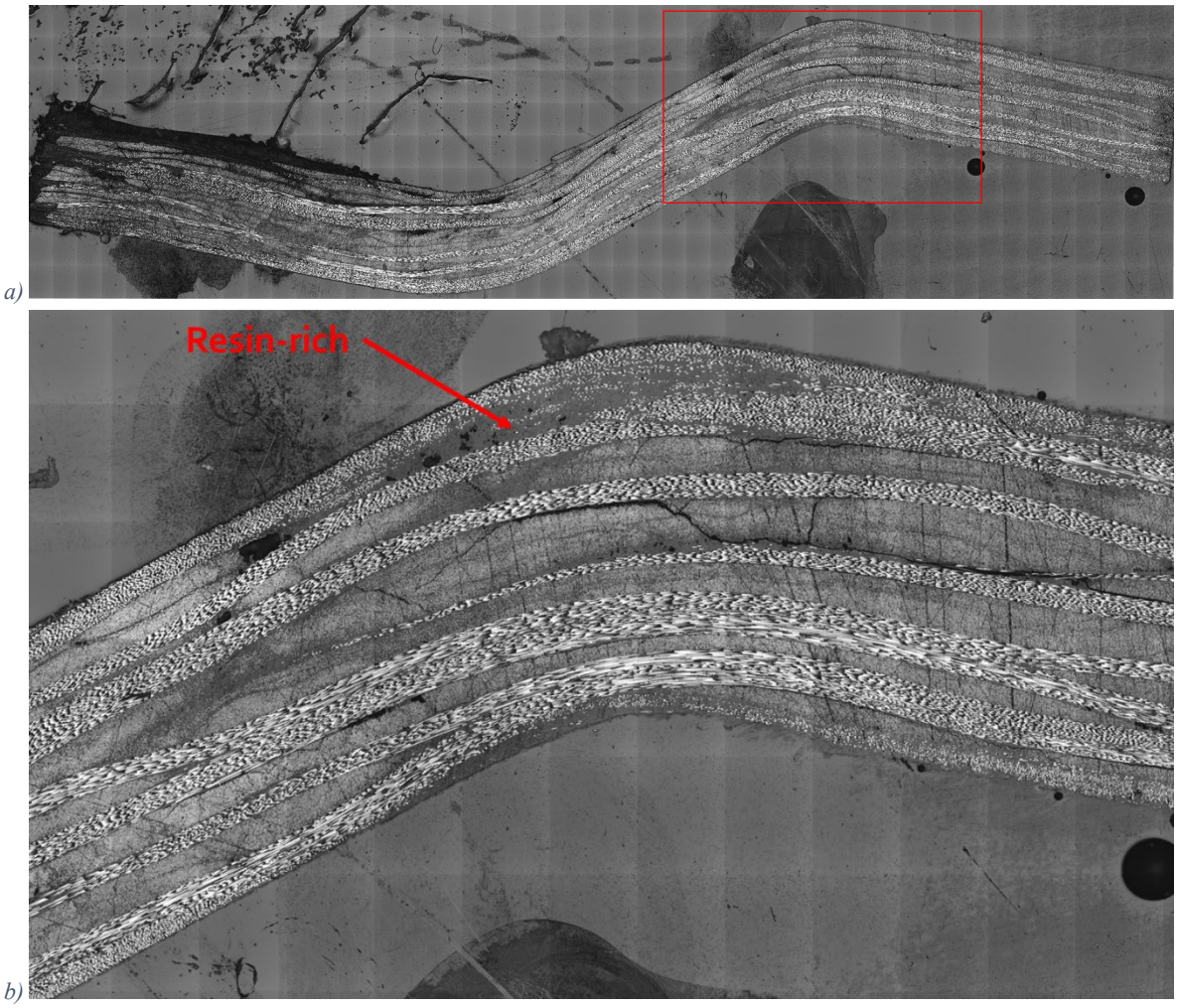

Figure 55. Micrograph of specimen extracted from Location F with a) full specimen and b) enlarged view.

A similar feature is shown in Figure 56, extracted from Location G in the seat back. In this case, the highlighted region enlarged in Figure 56b shows a large concentration of fibers aligned into normal to the page, which indicates significant internal tow movement into this region. Large resin-rich regions can also be observed in the image.

a)

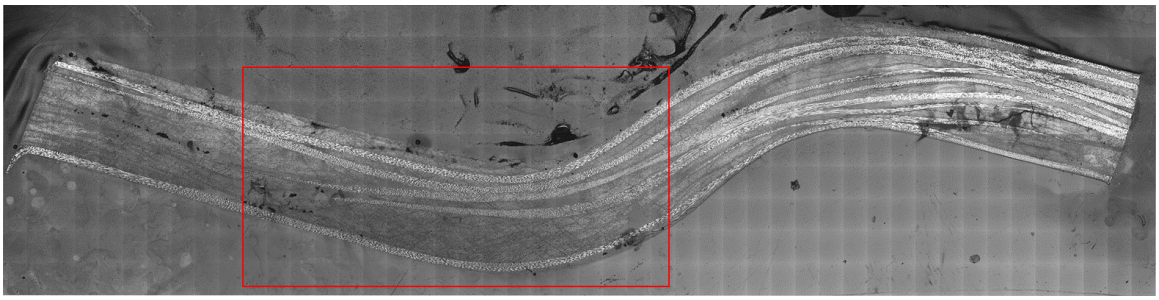

b)

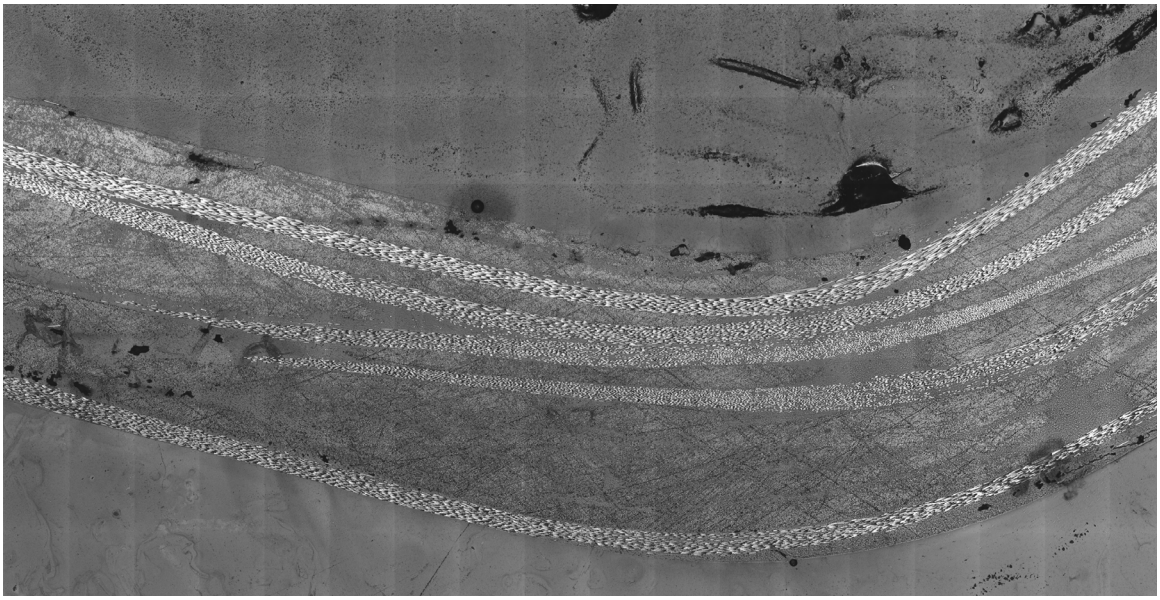

Figure 56. Micrograph of specimen extracted from Location G with a) full specimen and b) enlarged view.

The last image in Figure 57 of specimen H was extracted from a similar "S" feature as above where a double curvature also exists as the feature line makes a right angle bend. This image included similar behaviors as discussed above.

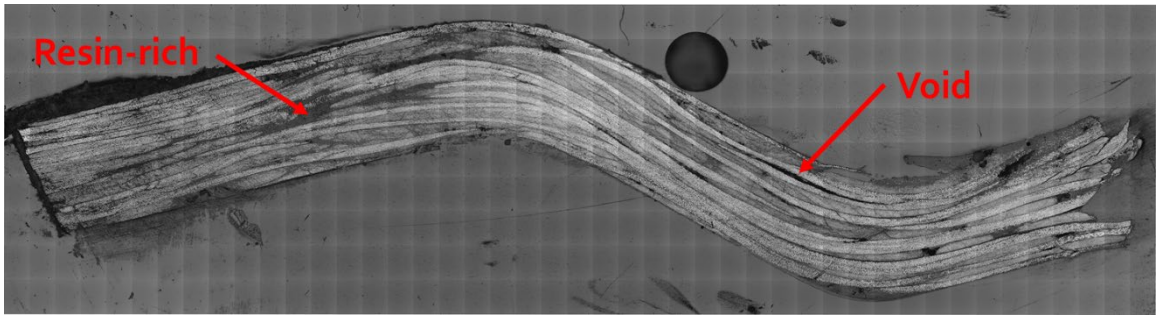

Figure 57. Micrograph of specimen extracted from Location H.

The CT images for each of the four specimens indicate that the seatback does have internal discontinuities that are further investigated in the micrographs to include both resin-rich regions and voids. The CT images also show that the RFF unit cells remain mostly intact during the molding process, but some localized movement of the tows does occur. In general, the imaging performed on the seatback yields positive results for the molding process, particularly for the

first three parts molded with this material system on a new tool that was not produced with this material form specifically.

5.11 Cost estimate for RFF fabrication equipment

While the cost of Fibrflex coated-tow material is much reduced when compared to fully impregnated carbon-fiber tape, reducing the cost of a finished composite is also dependent on the method by which the preform is prepared and consolidated. While this program has used a conventional AFP process to prepare the preforms up to this point, it is well understood that this process is too expensive when considering composites for industrial or automotive applications. This is because the flexibility to create complex geometries, embodied in the 5-axis AFP robots, is inherently expensive. In addition, the laser-based heat source is also expensive, and makes up a large portion of the equipment cost. These two factors will drive the cost of a conventional AFP too high to be considered for this application, even if a system can be developed to use one laser over the entire RFF surface.

RFF preform fabrication does not require many of the features that built into conventional AFP machines, because the process for laying down and consolidating the tows is different. First, since the RFF technology is usually based on flat non-crimp fabrics, the preforms are generally flat. This eliminates the need for multi-axis robotic arms, and the tape reels can be located on a stationary creel. Second, because RFF-based technology requires a post-laydown consolidation step, the combined laser/compression roller that must be operating at all times during AFP laydown to result in fully consolidated parts is not required. RFF preforms need only to be tacked together at strategic points, such as the tow-ends, and this can be done with a process that is not laser-based. This strategy will therefore save capital by eliminating the laser and the enclosure that is required for safe laser operation.

RFF panel fabrication can be broken down into three basic functions: tacking the tows together, extending the tows over the preform surfaces, and cutting the tows at the end of each traverse. The basic machine design consists of a high-speed x-y-Θ table, on which the coated tows are laid. Positioned above the table is a stationary row of inexpensive tow dispensers that control the position of the tow as it is being played out from the source spools that are located on a creel. The laydown process is accomplished by moving the table under the stationary tow dispensers, pulling the tow out of the dispensers as the table moves. Subsequent layers are applied by rotating the table and traversing the table under the dispensers once again. Fastening of the coated tows to the thermoplastic tape frame, similar to that used for the manually built fabrics, is done with small ultrasonic welders – one per tow. Ultrasonic welders were selected for this application because they are fast, and do not rely on heat conduction to attach the tows to the thermoplastic frame. An additional feature of ultrasonic welders is that they are exceedingly fast, and can therefore be used on moving tow with the use of a radiused horn, as demonstrated on several coated tow samples that were supplied to Dukane (a company that specializes in ultrasonics for welding) for evaluation. Welding during the translation process will increase the average speed for preform fabrication by not requiring the table to stop for welding. After welding, the tows are cut with ultrasonic cutters, again with one per tow. A schematic of a tow-laydown head is shown as Figure 54, with the tow dispensers (grey), ultrasonic welder (red), tow cutter (green), thermoplastic substrate (orange), table (white), and tow (black). Controlling the table, the welders, and the cutters is a computer or PLC. A schematic of the laydown process is

shown in Figure 55 with thermoplastic substrate (blue), dispensing heads (orange), coated tow (black), and ultrasonic welds (red).

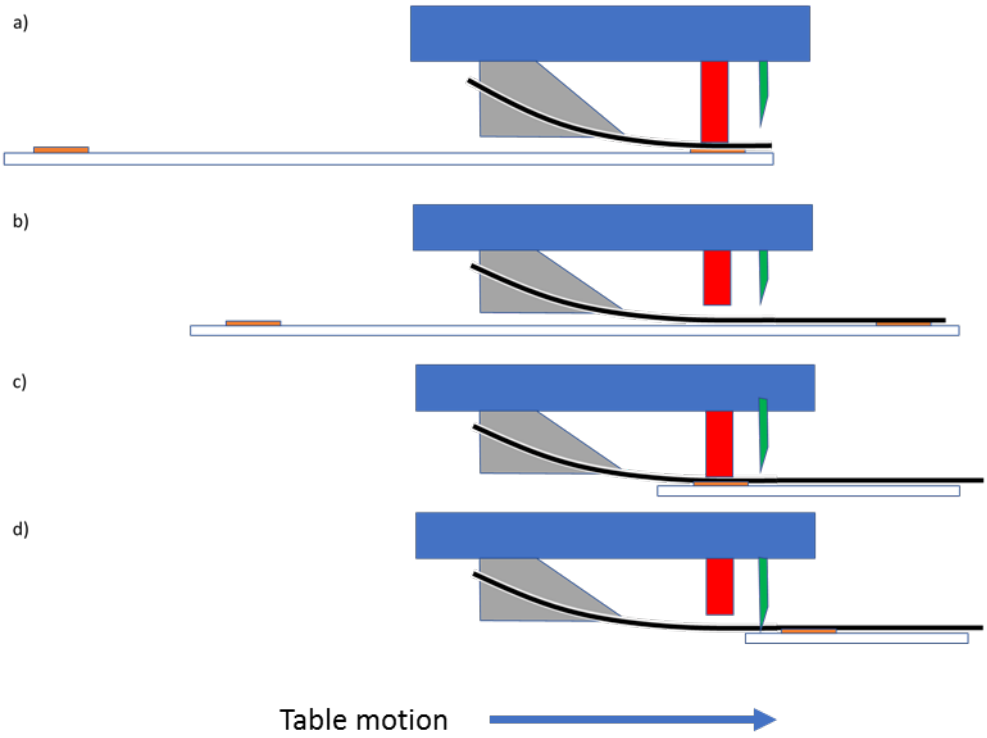

Figure 58. Schematic of stationary RFF tow-laydown head during different process steps; a) fastening the tow to the frame, b) dispensing the tow, c) fastening, and d) cutting the tow.

A typical process would run as follows. Initially, the table is positioned under the stationary tow-dispensers, as shown in 59a. The array of ultrasonic welding probes would then drop onto the coated-tows and weld them to the blue thermoplastic sheet resulting in the red welds shown in Figure 59b. Figure 59c shows the table traversing under the tow-dispensers, pulling out the required coated-tow. The tows are welded to the thermoplastic sheet as shown by the red circles, and then cut, resulting in Figure 59d. Figure 59e shows the table being turned by 90 degrees to prepare for the next layer, the start of which is shown in Figure 59f.

Since each tow is controlled independently, the system is very flexible in terms of the shape and layup pattern of the preform. It is not constrained to laying down square patterns because each tow lane has an independent ultrasonic attachment and cutting mechanisms and each can be controlled independently. It is therefore possible to make whatever shape is desired by the fabricator, i.e. near net shape preforms. Because the table can be rotated to any angle, the angular relationship between the tows can be optimized to the load requirements of the fabricated part.

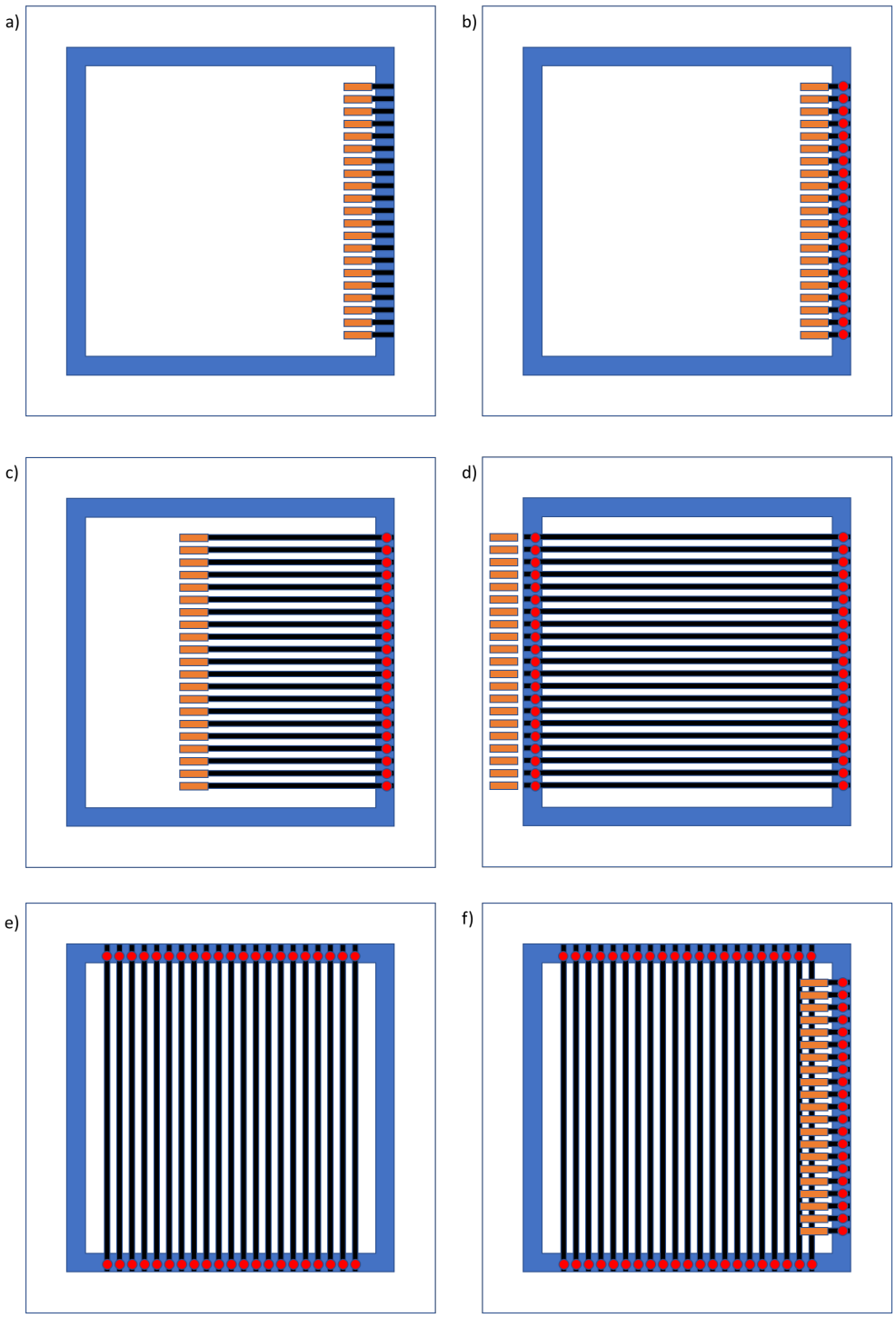

Figure 59. Schematic of tow laydown process a) process start, b) after tow welding, c) during dispensing, d) after weld and tow cut, e) table rotation, and f) beginning of second layer.

In terms of throughput, the system as described above has many benefits over a more conventional robot-based AFP system for simple geometries such as this. The laydown rate of coated-tow is much higher than traditional AFP because multiple tows can be applied in parallel,

the number of which is only limited by the number of ultrasonic welders and cutters that will fit within the equipment budget. Examples of moving tables such as this one can achieve translation rates of between one and five meters per second, and ultrasonic welding and cutting can be accomplished for this materials in well under one second. Assuming a one third second weld time, a similar amount of time for the cutting cycle, and a 1 meter per second table traverse, one layer of the RFF can be deposited in two seconds. Following this the table must be rotated 90 degrees and returned to the starting position. Assuming a two second time for this, a complete 4x4 unit cell RFF can be created in 30 seconds. If the unit has the capability to supply 37 tows, the center of each spaced 1 inch apart, the system will be capable of creating a 36-inch square, 4x4 RFF in that amount of time.

A faster, but more capital-intensive process, might be configured with multiple stations similar to the one described above. In this case, each application station would apply a single layer of tows, with the table being moved between laydown stations sequentially. In this case, an eight-layer build like the one above would require 8 application stations, with the table being rotated between applications as shown in Figure 60. In this case, because all of the layers are being applied in parallel, a completed fabric would be produced every four seconds. The mechanism by which the tables would be transported down the entire line of 8 application stations will require a significant amount of hardware and engineering, not covered in this document, and would therefore be more expensive than the single-table system required for application of 8 layers sequentially.

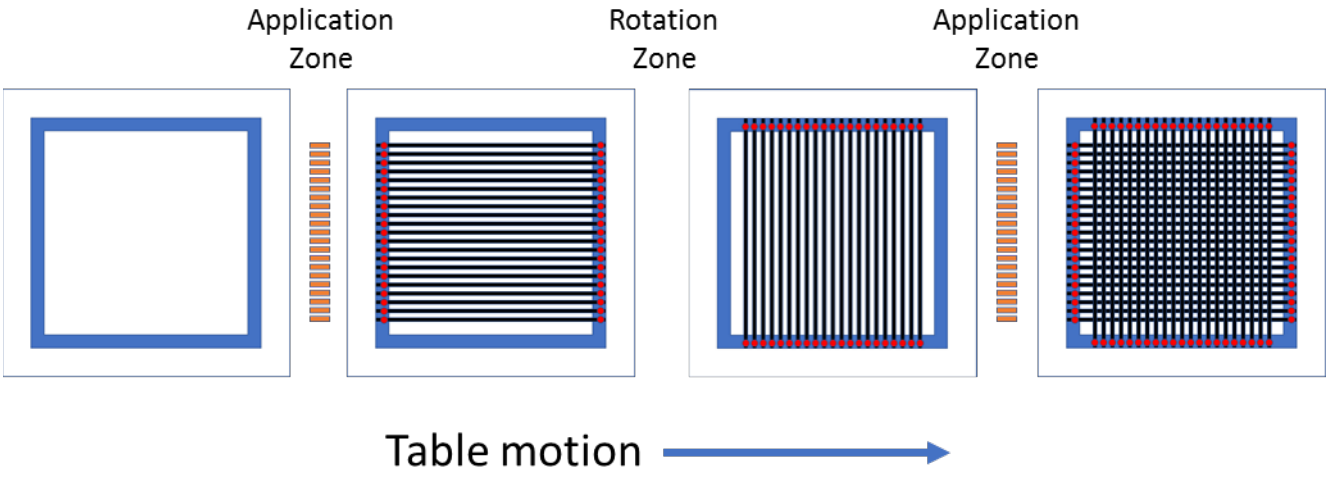

Figure 60. Process schematic for continuous batch RFF process.

For the purposes of this program, the Team decided to focus on a unit that consisted of a single work station with 37 application heads, with a single table that would both raster and rotate under a single application zone. This system will be capable of creating up to a 36” square of RFF. The cost estimate can be broken down into two major components, the ultrasonic components and the automation. It should be noted that all costs shown in the following tables are for information only, and do not represent how much the components can be purchased for in the future.

The layup-table components were recommended by Macron Dynamics (Paoli, PA) and were selected to provide traverse rates of over one meter per second, with a stroke distance of 1 meter in the x direction, 15cm in y, and 360 degrees in Θ. All of the translation components are mounted under the rotation actuator for simplicity. Additional automation is required for the raising and lowering of the individual ultrasonic components, and this function is provided with 74 linear actuators. An estimate of the cost of the table and automation components is shown in Table 5. The table itself was specified as a one meter square sheet of aluminum, 6 mm thick. This thickness is specified to provide the substrate stiffness required for ultrasonic welding and cutting. The sequencing of the automation is performed using an EtherCAT system.

Table 5. Cost estimate of automation components for laydown-table for single-table design.

Quantity	Description	Price Each	Total Price
1	X & Y Macron Dynamics Gantry System	39,000	39,000
1	Camco Rotary Cambox with servo	12,000	12,000
74	Horn Linear Actuator	900	66,600
1	Electrical Controls Enclosure	25,000	25,000
	Mechanical Engineering		11,000
	Electrical Engineering		9,500
	Programming		22,000
	Mechanical Components		7,500
	Miscellaneous Expenditures		5,000
		TOTAL	197,600

The majority of the cost of the current design is in the ultrasonic systems. Ultrasonic technology was selected due to its cleanliness, controllability, and speed, but can be replaced with other technologies if cost is a controlling concern. The components for this system were recommended by Engineered Automation Components (Hatfield, PA), a distributor for Dukane, and are listed in Table 6. As designed, each signal generator will feed the welding and cutting heads on a single laydown-head, as these two functions will not be used simultaneously. This dramatically reduces the cost of the entire system.

Table 6. Cost estimate of ultrasonic components for single-table design.

Quantity	Model	Description	Price Each	Total Price
37	40AP060-2F	IQ-Auto 40K 600W 240V Gen	3705.00	137,085.00
74	41C28-001	41C28 Probe w/ rear mount connector	1570.00	116,180.00
74	110-2534	1.0 to 1 Aluminum Booster w/ 8mm studs	300.00	22,200.00
74	200-615-03M	40kHz Ultrasound Cable – 3 meters	155.00	11,470.00
37	MPC0402	Single Row MPC enclose	625.00	23,125.00
37	200-479-03M	MPC Ultrasound Cable – 3 meters	155.00	5,735.00
37	200-1408-03M	MPC Interface Cable – 3 Meters	125.00	4,625.00
4	721-44	30/40 kHz Pinned Spanner Wrenches	40.00	160.00

37		40 kHz Welding Horn – Ti	750.00	27,750.00
37		Cutting Horn	650.00	24,050.00
37		Carbide Cutting Tips	150.00	5,550.00
			TOTAL	367,720.00

Combining the ultrasonic system with the table system, the estimated cost of the entire system is just over $565,000, and will be capable to produce an RFF panel up to one meter square every 30 seconds.

6 BENEFITS ASSESSMENT

The results of the work described above demonstrates that the cost of manufacture of continuous carbon fiber composites at high rates can be significantly reduced relative to using woven cloth by employing a near-net-shape Rapid Fabric Formation process using FibrFlex® coated tow technology. In addition, enhanced drape of FibrFlex® fabrics made using coated tow materials in RFF, as well as enhanced control of fiber motion during molding allows for more tow control and therefore predictable complex shape formation. With these benefits, relatively inexpensive complex thermoplastic CFRP composites should be enabled, the cost of carbon fiber excluded, with cycle times and costs low enough to allow penetration into mass market applications should the cost of carbon fiber be reduced. The reduced COM of carbon fiber composite parts will enable faster market penetration into high volume commercial applications. This in turn will drive energy savings through system lightweighting and associated support for job creation in the composites industry.

As stated on the IACMI website:

> "IACMI's research, development, and demonstration programs will be driven by major industry participation with a focus on reducing technical risk and developing a robust supply chain to support a growing advanced composites industry."

This program has focused on the fabrication and characterization of RFF-based parts, and by demonstrating the benefits associated with this technology, has de-risked the adoption of this process to relatively low cost CFRP composites for mass market industries.

Also stated on the IACMI website

> "The Institute for Advanced Composites Manufacturing Innovation, IACMI, is committed to delivering a public-private partnership to increase domestic production capacity, grow manufacturing and create jobs across the US composite industry."

Through substantial cost reduction of thermoplastic composites, this project has the potential to broaden the domestic industrial manufacturing base for these products, with the follow-on impact of creating high quality jobs.

7 COMMERCIALIZATION

These results have shown that the cost of continuous carbon fiber composites can be reduced by using Fibrtec's coated tow technology combined with near net shape processes such as automated fiber placement. This will lead to accelerated adoption of these materials into mid-

range value applications such as those in the automotive industry

8 ACCOMPLISHMENTS

This project has shown that coated-tow technology combined with automated fiber placement will lead to reduced cost of carbon fiber composite. In addition, these materials have been shown to have beneficial draping properties that will allow enhanced conformation to mold shapes.

Phase I of this program was completed at the end of March 2017. During this phase of the program, a significant de-risking of the technology was demonstrated.

1) A preliminary technoeconomic forecast was created that compared the processing costs of the CT/RFF technology to existing composite manufacturing methods. The analysis indicated that CT/RFF technology will enable creation of preforms at a 30% savings relative to existing dry carbon weave/PA film consolidation technology. A major portion of the benefit comes from the ability of CT/RFF to directly make near net shape preforms, eliminating the majority of the carbon fiber waste.

2) A process was developed to produce coated tow at greater than 100 feet per minutes. The process speed is currently limited by the uptake equipment rather than by the coated tow formation process. This limitation is easily overcome by making straight forward mechanical modifications to the winder to maintain the 130fpm speed.

3) A production facility for making RFF fabrics was demonstrated with variable crossover angles and variable bonding density. Specifically, fabrics with 0/90 and 60/120 orientations were made with different bonding programs

4) Consolidated RFF fabrics were strength tested. The produced data indicates that stiffness and strength of the consolidated RFF CFRP composites are greater than 90% of the theoretical maximum for 0/90 laminates.

5) One commercially viable part that can benefit from this technology was selected for evaluation in future work. Ford worked with the Team to assess multiple applications. As a result, a lower control arm was selected as a commercially viable target.

6) Models were developed for the deformation of unconsolidated RFF fabrics and the mechanical properties of the consolidated composites. These models predicted that there will be a substantial benefit in fabric draping for molding RFF materials when compared to 2,2 twill carbon fabrics.

Phase 2 of this program was completed in February 2019. During this phase of the program, the technology was successfully demonstrated.

1) Enough coated-tow was produced for the creation of both parts for property

determinations and the demonstration parts.

2) An automotive lower control arm was successfully modeled and it was determined that this part was not a suitable target. As a result, the target part was changed.

3) Two additional target parts for which molds already existed were identified, one having a large format suitable for automotive applications, and the second, while smaller, having areas of deep draw where the drape benefits of RFF could be demonstrated.

4) Drape in the targeted molds was modeled using PAM-FORM to identify areas of the most risk.

5) The topologically complex Manta laptop case and a large area automotive seatback were successfully molded.

6) The cost of a developmental RFF laydown unit capable of high throughput was estimated.

9 CONCLUSIONS

The Project Team has successfully demonstrated all of the requisite steps for a new low cost concept for creating low cost thermoplastic CFRP composites at high rates. These steps include polymer matrix production, coated tow production, and RFF preform production. This technology should enable CFRP composites to be more economical for mass market applications.

10 RECOMMENDATIONS

Due to mold availability, this program used a relatively slow compression molding process. However, a stamping process, where the thermoplastic preform is preheated prior to being stamped in a warm mold, should be optimized. Processes such as this have been demonstrated on thermoplastic parts in the laboratory in DuPont and elsewhere, but not for RFF preforms. Demonstration of this low-risk process will ensure that production times of CFRP composites can be reduced dramatically reduced, and with that the cost of capital required for their production.

11 REFERENCES

1. Popper, P., Walker, C.W., Tam, A.S., Yngve, P.W., Odle, J.K., and Thomson, G.Y, Rapid Fabric Forming, US Patent 6,107, 220
2. Brosius, D., & Deo, R. *Impact of Technology Developments on Cost and Embodied Energy of Advanced Polymer Composite Components*. United States. doi:10.2172/1437162.
3. Silverman, Lee, Bogdanor, Michael, Davies, Robert, and Dickinson, Jacob. Tue . "Thermoplastic Composites Parts Manufacturing Enabling High Volumes, Low Cost, Reduced Weight with Design Flexibility". United States. doi:10.2172/1434284. https://www.osti.gov/servlets/purl/1434284

APPENDIX 1. MATERIALS CHARACTERIZATION REPORT

DuPont Material Characterization Report

Customer Technical Contact:

Lee A. Silverman
lee.a.silverman@dupont.com

Purdue CMSC Technical Contact:
Michael Bogdanor
bogdanor@purdue.edu

Josh Dustin
jdustin@purdue.edu

David Minkyum Kim
kim1550@purdue.edu

Himal Agrawal
agrawalh@purdue.edu

1 RESULTS SUMMARY

Material	Layup	Volume Fraction	ASTM Standard	Property	Average	Unit	St. Dev.	Min	Max
UD	[0]8	47	ASTM D3039	E1	108.19	GPa	6.28	102.18	122.05
UD	[0]8	50		E1	119.73		5.41	111.71	129.09
UD	[0]8	53		E1	120.39		2.49	118.33	125.91
UD	[0]8	47		X1	1519.1	MPa	201.67	1199.4	1841.7
UD	[0]8	50		X1	1814.0		100.61	1652.9	1976.4
UD	[0]8	53		X1	1507.1		91.14	1354.2	1675.2
UD	[0,90]2s	47		E1	55.95	GPa	2.32	53.30	59.29
UD	[0,90]2s	50		E1	60.00		1.11	58.92	61.50
UD	[0,90]2s	53		E1	60.03		1.94	58.58	63.07
UD	[0,90]2s	47		X1	896.7	MPa	29.00	873.7	929.9
UD	[0,90]2s	50		X1	901.4		51.95	850.1	981.4
UD	[0,90]2s	53		X1	960.5		38.03	918.2	997.3
RFF[0/90]	[0]4	50		E1T	61.47	GPa	6.64	48.26	59.38
RFF[0/90]	[0]4	50		X1T	851.4	MPa	158.28	617.8	1084.1
RFF[0/90]	[0]8	50	ASTM D3410	E1C	54.58	GPa	5.78	47.65	63.06

RFF[0/90]	[0]8	50		X1C	253.4	MPa	39.35	195.6	340.7
RFF	$[\pm 45]4$	50	ASTM D3518	G12					
RFF	$[\pm 45]4$	50		X12					
RFF[0/90]	[0]12	50	ASTM 5528	GIC	1175	$\mathrm{J/m^2}$	305.77	855	1444
RFF[0/90]	[0]12	50	ASTM D7905	GIIC	2321		332.35	1977	2763
RFF[0/45]	[0]4	50	ASTM D3039	E1	48.50	GPa	2.83	44.19	51.82
RFF[0/45]	[0]4	50		X1	572.5	MPa	78.82	396.5	674.1

*note: test results are not normalized to fiber volume fraction

2 TEST PLAN

2.1 Background

DuPont is exploring a new composite manufacturing technique that will be used as replacement for metals. This new material combines FIBRTEC's flexible coated tow FibrFlex™ technology with DuPont's Rapid Fabric Formation (RFF) technology and a proprietary DuPont polyamide resin. The coated tows are partially impregnated carbon fiber/polyamide composite tow where the tow is not fully wetted with the polyamide initially, which allows it to be a more flexible tow material than a fully impregnated tow. The layers of the fabric are held together in this material by locally melting the polyamide at the intersection between tows in specific locations to connect the top layer of tows to the bottom layer. The below figure briefly shows how RFF process goes.

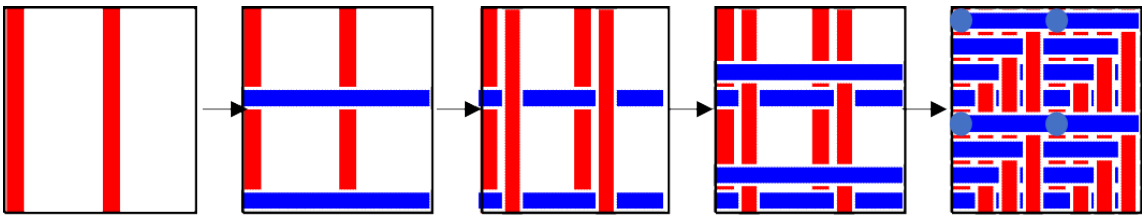

Figure 1. Rapid Fabric Formation process.

Material characterization is done on various ply setups to find Young's modulus, compressive modulus, shear modulus, strength in respective directions, Mode I / II fracture toughness, etc… The testing procedure is to prepare the specimens from the panels and coupons sent from DuPont and FIBRTEC and to follow corresponding ASTM standards to perform testing. Post processing is done afterwards to provide characterization results.

2.2 Testing Methods

The following ASTM standards are used for the testing and are listed out for reference.

Tensile test	ASTM D3039
Double Cantilever Beam test	ASTM 5528
Compression test	ASTM D3410
End Notched Flexure test	ASTM D7905
Shear Test	ASTM D3518

2.3 Test Coupon Machining

Waterjet cutting was used when plates needed to be cut into certain dimensions. There also is a surface grinder, but waterjet requires less time and has better surface finish. Therefore, waterjet cutter is preferred over the surface grinder in preparing the panels into coupon specimens.

Figure 2. Waterjet Cutter

After the specimens were cut in required dimensions, surface preparation was done using sand paper and orbital grinder.
Excess adhesive was removed using the belt sander to get a flat surface to be used as guide surface.

Figure 3. Belt Sander

When a rough cut needs to be made, vertical band saw was used.

Figure 4. Vertical Band Saw

For attaching the tabs and piano hinges onto the specimens in tensile, compression, and double cantilever testing, LORD 7542A/B Urethane Adhesive was used. Applying the urethane adhesive was done by using an epoxy gun and a mixing tube attached at the front that mixed the two parts to cure.

Figure 5. Lord 7542A/B Urethane Adhesive

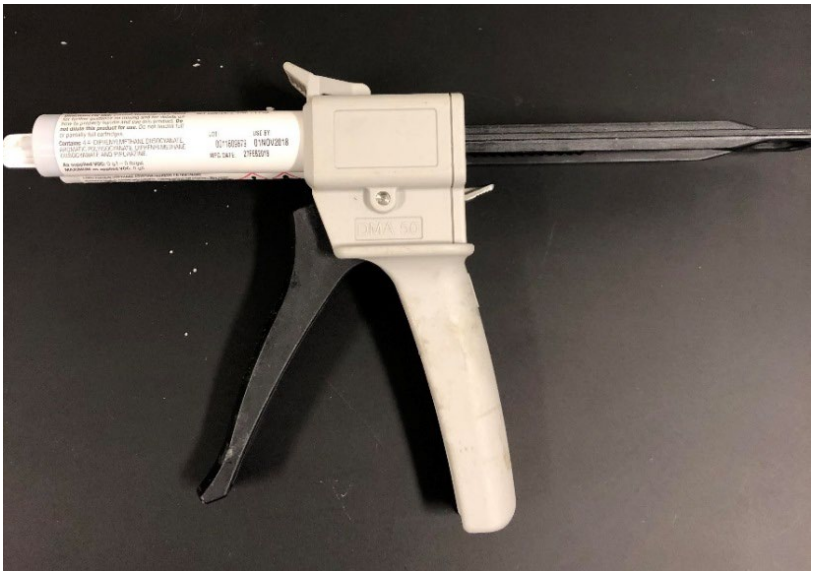

Figure 6. Epoxy Gun

3 EQUIPMENT

A 22 Kip machine with a 22 Kip load cell was used for the tensile testing of the specimens. Also, a 5 Kip machine with a 1 Kip load cell was used to perform the double cantilever beam and end notched flexure tests. The figure below shows the machine used. The tests were performed according to the ASTM standard mentioned previously. The images below show the machines used for the testing.

Figure 7. 22 Kip MTS

Figure 8. 5 Kip MTS

Tab sliding was observed while the specimens were tensile tested, and in order to avoid tab sliding, emery cloth was used at the machine grips to provide sufficient amount of friction to avoid slipping.

Figure 9. Emery Cloth

For the calculation and analysis of strain, Digital Image Correlation was used instead of strain gauges as DIC provides much larger field of view. However, for compression testing, due to the restricted field of view because of the fixture, strain gauges were used. To use DIC analysis, white enamel paint was sprayed and then speckle pattern was applied. DIC measures the distance traveled by each speckle pattern to analyze strain.

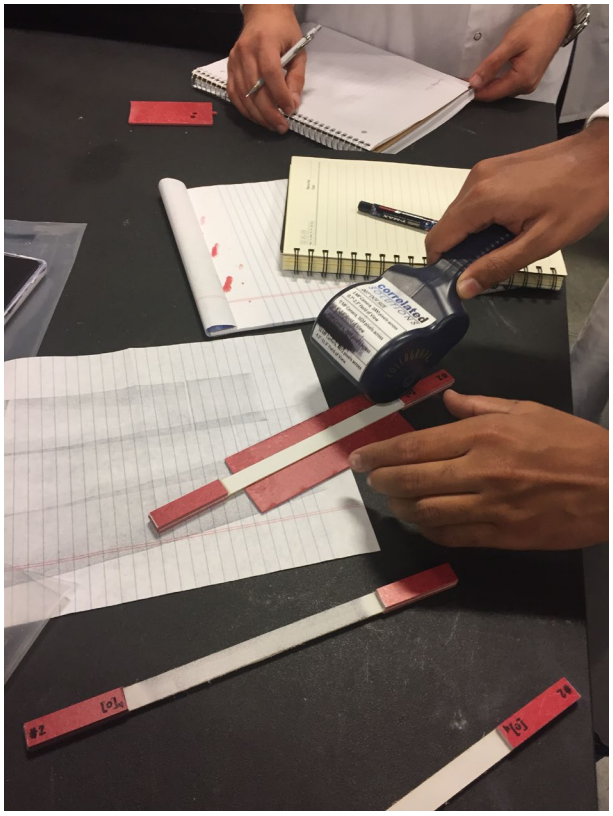

Figure 10. Applying speckle pattern

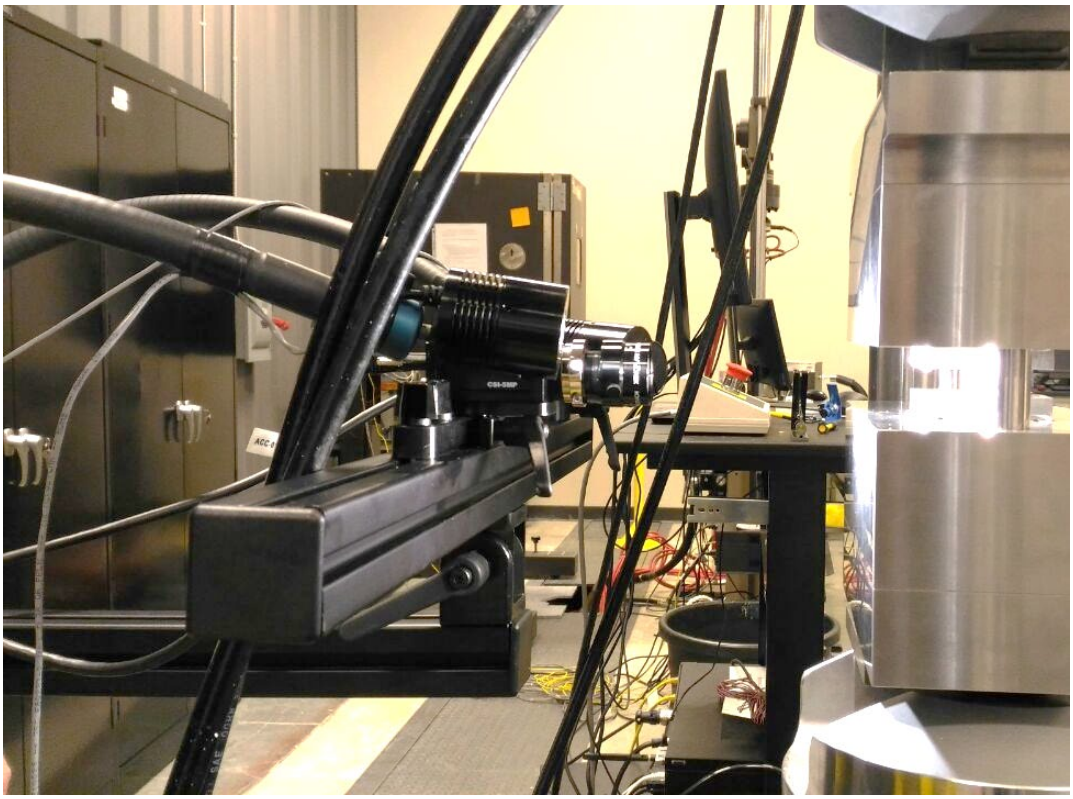

Figure 11. DIC camera

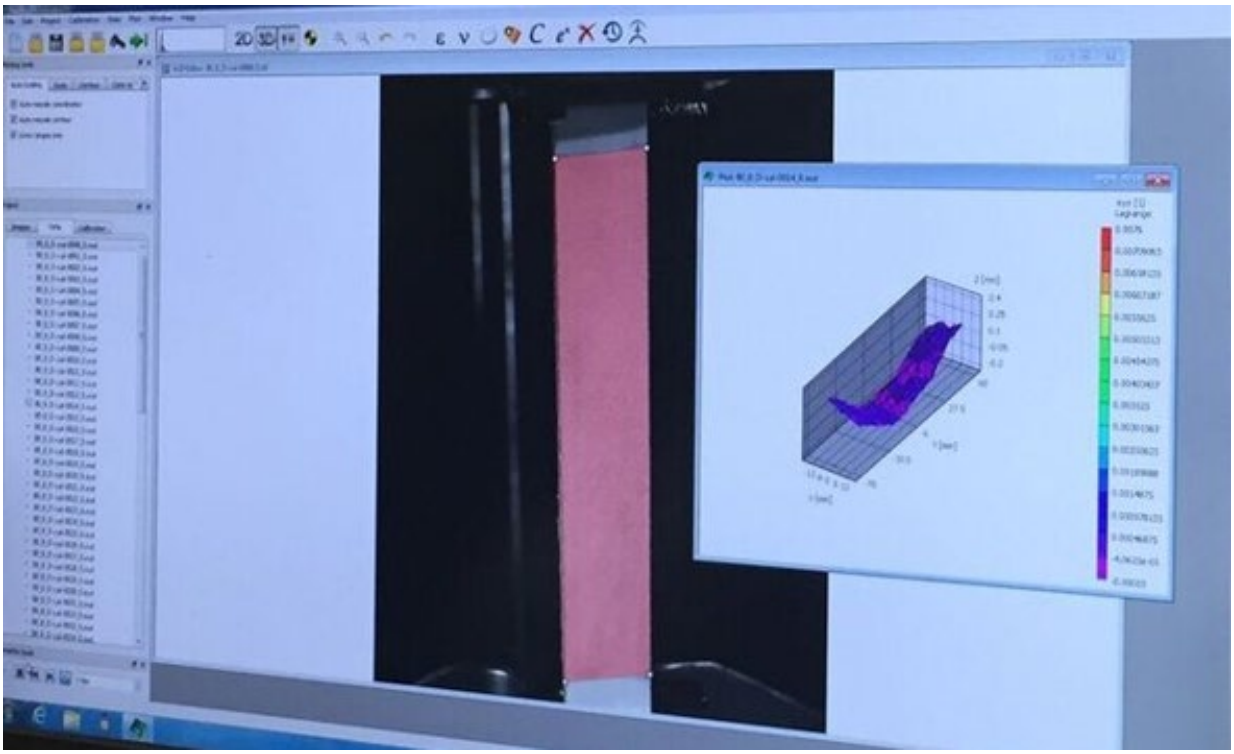

Figure 12. DIC Post-processing

For measuring crack length during DCB testing, moving microscope was used to view the

crack at a magnified monitor.

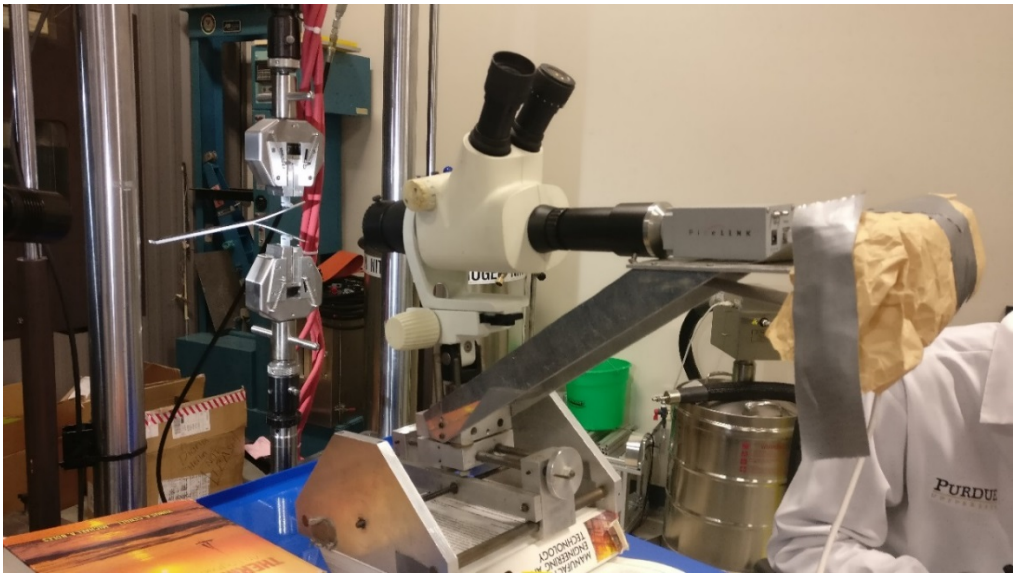

Figure 13. Moving Microscope

4 MATERIAL RECEIVED

The following coupons and panels were received from DuPont and FIBRTEC. Their images are included below in the table.

Material Provider	Panel ID	Details
FIBRTEC	EX0816DP-47	6 Ply-0's
FIBRTEC	EX0816DP-50	6 Ply-0's
FIBRTEC	EX0816DP-53	6 Ply-0's
FIBRTEC	EX0816DP-47-06	8 Ply [0/90]'s
FIBRTEC	EX0816DP-50-06	8 Ply [0/90]'s
FIBRTEC	EX0816DP-53-06	8 Ply [0/90]'s
DuPont	D201166-6-A	10.5''x10.5'' Panel 4 ply [0/90]
DuPont	D201166-6-B	10.5''x10.5'' Panel 4 ply [0/90]
DuPont	D201166-6-C	10.5''x10.5'' Panel 8 ply [0/90] Compression
DuPont	D201166-6-D	10.5''x10.5'' Panel [45/45]
DuPont	D201166-6-E	10.5''x10.5'' Panel [45/45]
DuPont	D201166-6-F	10.5''x10.5'' Panel 12 ply [0] Teflon Insert
DuPont	D201166-6-G	10.5''x10.5'' Panel 12 ply [0] Teflon Insert
DuPont	D201166-6-H	10.5''x10.5'' Panel 4 ply [0/45]
DuPont	D201166-6-I	10.5''x10.5'' Panel 4 ply [0/45]
DuPont	No Numbering	Weaved pattern for DCB+ENF
DuPont	No Numbering	Weaved pattern for DCB+ENF

Table 1. Panels received from DuPont and FIBRTEC

Test	Coupons + Panels Used
Tensile test of FIBRTEC Coupons	EX0816DP-47, EX0816DP-50, EX0816DP-53 EX0816DP-47-06, EX0816DP-50-06, EX0816DP-53-06
Tensile test of RFF	D201166-6-A, D201166-6-D
DCB test	D201166-6-F
Compression test	D201166-6-C, recycled D201166-6-F
ENF test	D201166-6-G
[0/45] Tows tensile test	D201166-6-I
Shear test	D201166-6-B
Not Used Yet	D201166-6-E, D201166-6-H

Table 2. Panels Tracking

EX0816DP-47 EX0816DP-50 EX0816DP-53	EX0816DP-47-06 EX0816DP-50-06 EX0816DP-53-06

D201166-6-A Front	D201166-6-A Back
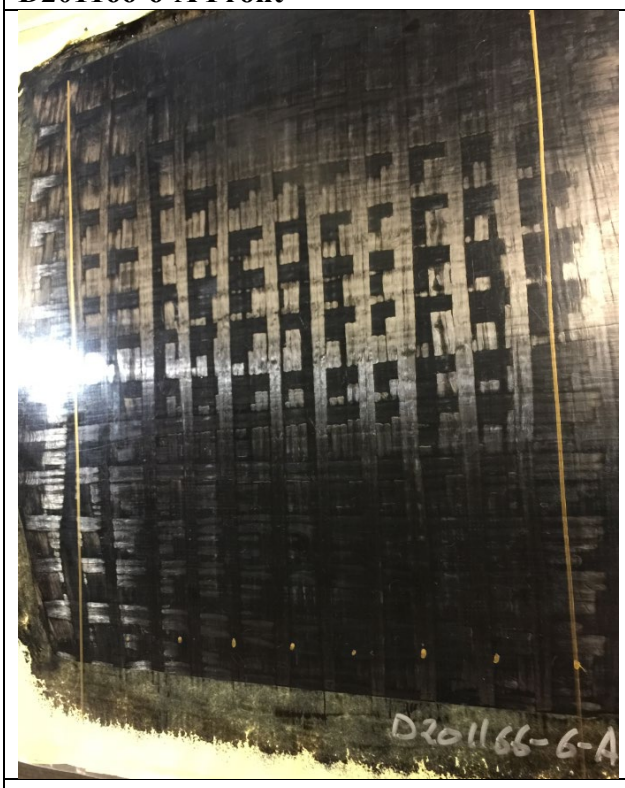	
D201166-6-B Front	**D201166-6-B Back**
	

D201166-6-C Front	D201166-6-C Back
	
D201166-6-D Front	**D201166-6-D Back**
	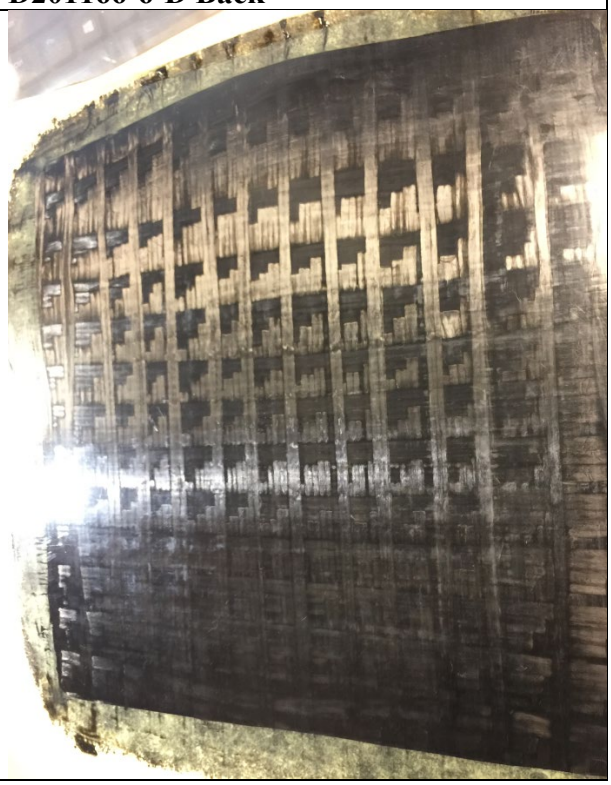

D201166-6-E Front	D201166-6-E Back
	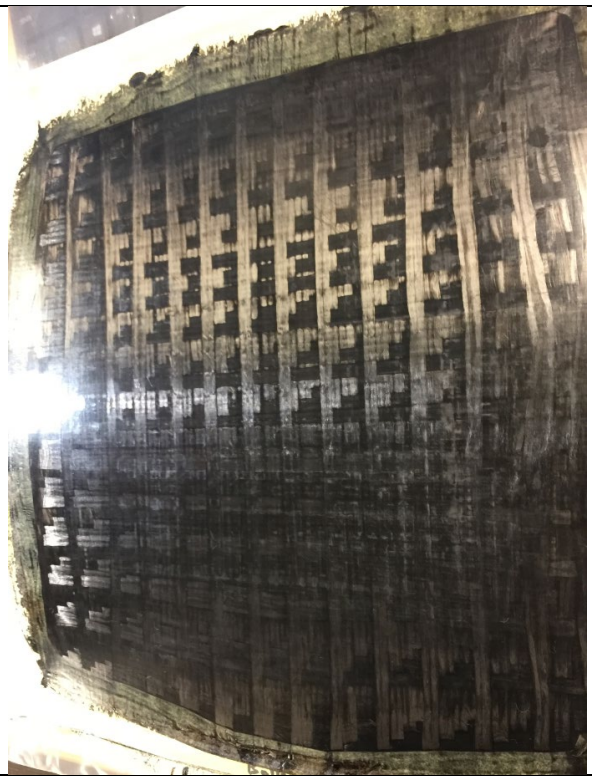

D201166-6-F Front

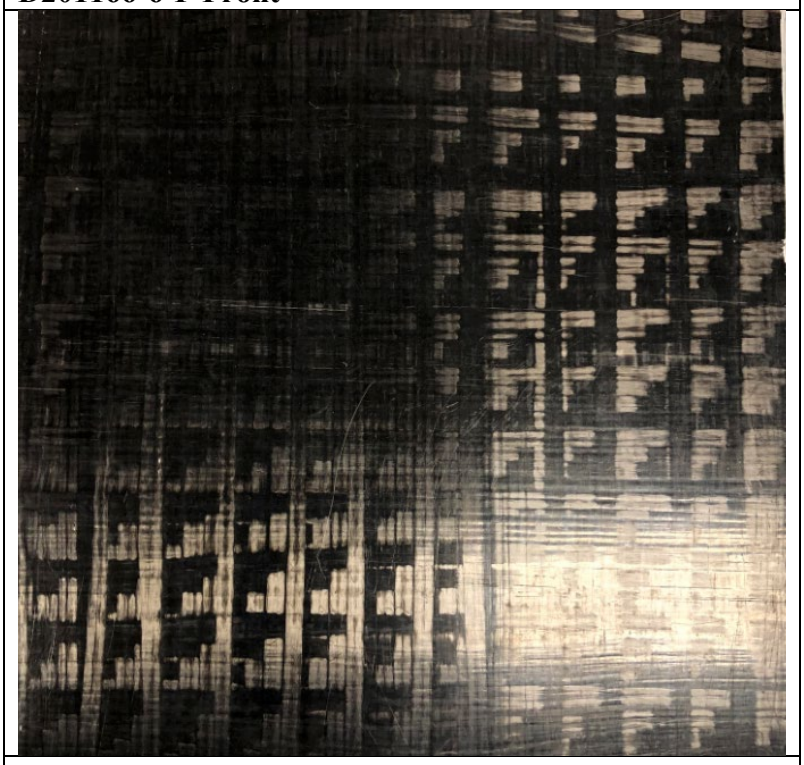

D201166-6-G Front

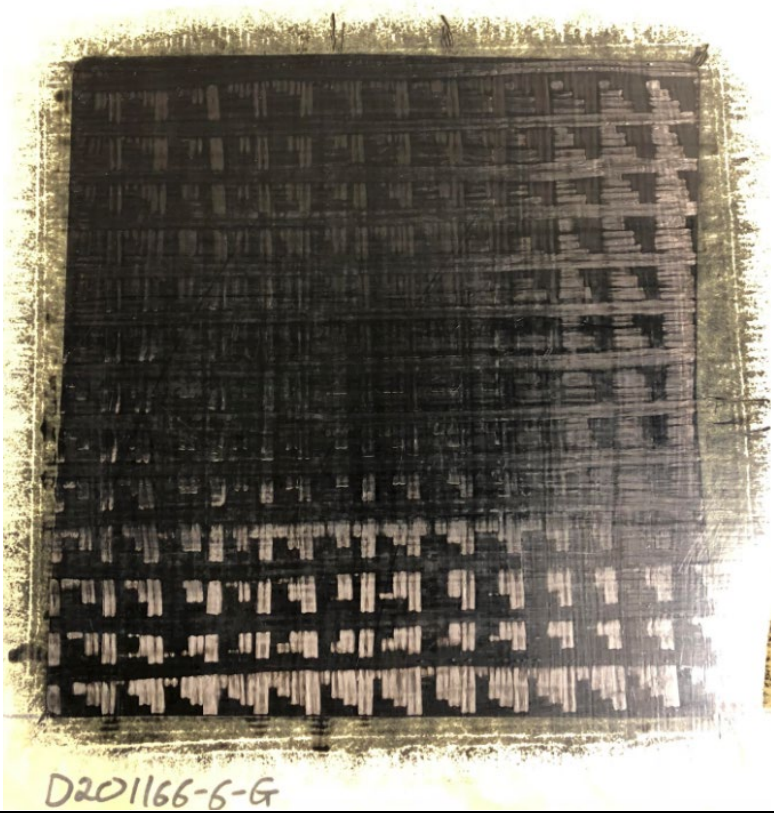

D201166-6-H Front

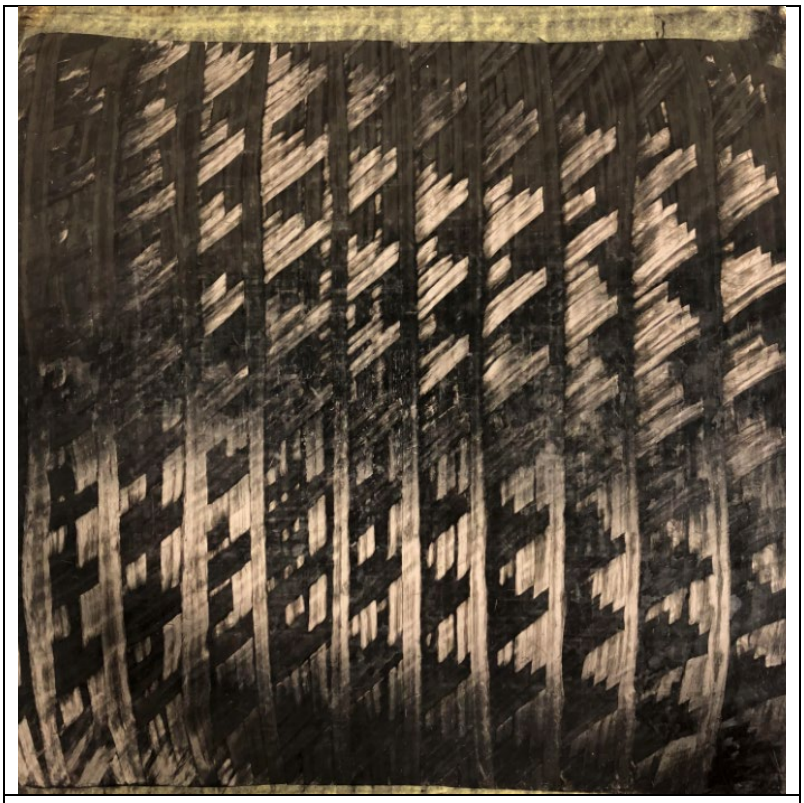

D201166-6-I Front

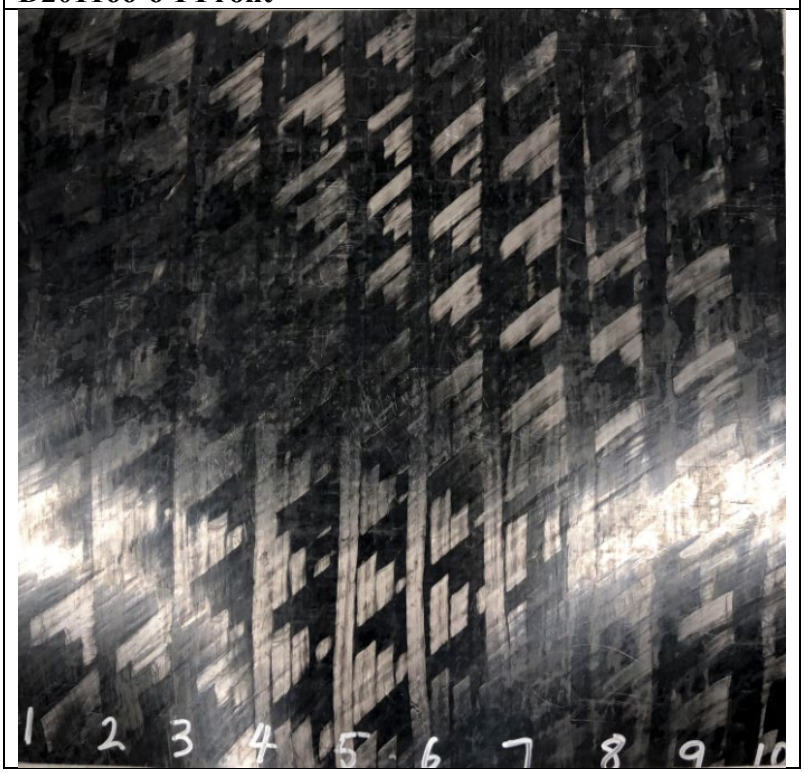

Weaved Pattern – No numbering

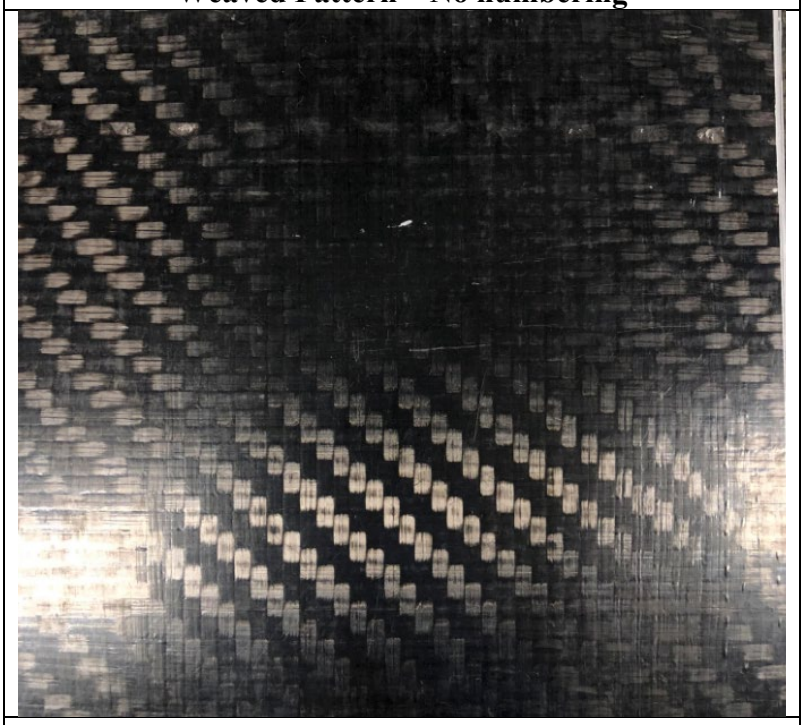

Weaved Pattern – No numbering

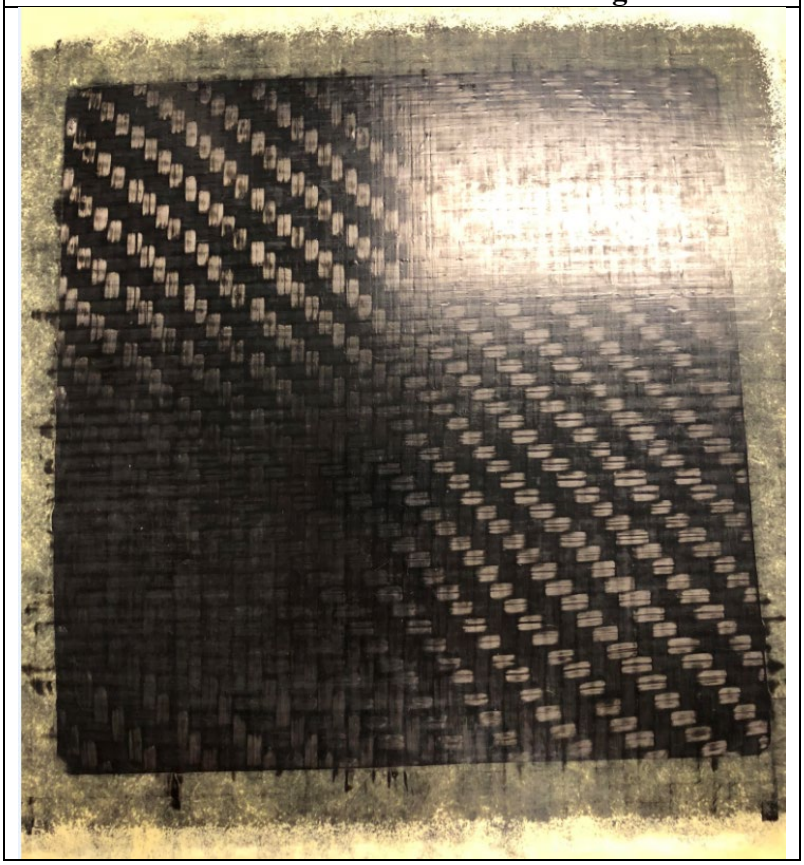

5 TEST RESULTS

5.1 Tensile Testing of FIBRTEC Specimens

5.1.1 Summary

First, 5 out of 10 $[0]_6$ samples and 1 out of 5 $[0/90]_8$ from FIBRTEC for each fiber content of 47%, 50%, 53% are tested for tensile properties. Total of 15 0° samples and 3 0/90 samples are tested. Red fiberglass sheets are cut to prepare tabs for the MTS grips. After the surfaces of the tabs and specimens are prepared, epoxy resin is used to attach the two. However, during the tensile testing process, most of the tabs slid before the specimens fractured. This means the tensile strength value could not be valid. The tab sliding often occurs in thermoplastic materials, and the surface is even more slippery when the resin material is nylon. Therefore, instead of tabbing the specimens, emery cloth is used to provide a coarse layer for the grips and also the surfaces are more roughened with coarser grit size. Only first set of $[0]_6$ samples were tested and experienced tab sliding, and the $[0/90]_8$ were tested directly with emery cloth.

After changing to emery cloth, the rest of the samples are all tensile tested. Strain is evaluated with speckle pattern Digital Image Correlation (DIC) analysis. The strain used for calculating Young's Modulus was calculated by using strain from 0.002 to 0.005.

5.1.2 Dimension

	Avg Width [mm]	**Avg Thickness** [mm]	**Cross sectional Area** $[mm]^2$
47 02 A	12.78	1.45	18.59
47 03 B	12.90	1.47	18.89
47 01 B	12.88	1.39	17.85
47 03 A	12.98	1.46	18.92
47 02 B	12.86	1.43	18.42
50 02 A	12.96	1.39	17.97
50 01 A	12.83	1.45	18.60
50 04 A	12.98	1.42	18.39
50 01 B	12.86	1.43	18.45
50 02 B	12.89	1.41	18.21
53 03 A	12.95	1.44	18.67
53 02 A	12.72	1.46	18.59
53 02 C	12.94	1.45	18.79
53 02 B	12.92	1.44	18.59
53 01 C	12.79	1.47	18.75

Table 3.Tensile testing of $[0]_6$, tab sliding

	Avg Width [mm]	**Avg Thickness** [mm]	**Cross sectional Area** $[mm]^2$
47-06D	25.11	2.07	52.05
50-07C	26.83	1.93	51.74
53-07C	26.74	1.94	51.94

Table 4.Tensile testing of $[0/90]_8$*, Emery Cloth*

	Avg Width [mm]	**Avg Thickness** [mm]	**Cross sectional Area** $[mm]^2$
4704B	12.96	1.38	17.91
4701C	12.76	1.32	16.90
4702C	12.88	1.31	16.93
4703C	12.84	1.36	17.51
4704C	12.85	1.29	16.61
5003B	12.91	1.32	17.09
5004B	12.94	1.31	16.96
5002C	12.83	1.33	17.04
5003C	12.83	1.30	16.72
5004C	12.83	1.29	16.51
5304A	12.73	1.30	16.59
5303B	12.85	1.33	17.04
5304B	12.73	1.31	16.72
5303C	12.82	1.31	16.84
5304C	12.69	1.31	16.65

Table 5. Tensile testing of $[0]_6$*, Emery cloth*

	Avg Width [mm]	**Avg Thickness** [mm]	**Cross sectional Area** $[mm]^2$
4706A	25.98	2.13	55.24
4706B	25.11	2.07	51.74
4706C	26.83	1.93	52.44
4706E	26.74	1.94	51.94
5008A	26.57	2.03	53.84
5008B	26.27	1.90	51.74
5008D	26.55	1.88	49.82
5008E	26.35	1.99	52.45
5307A	26.89	1.98	53.16
5307B	26.55	1.92	51.00
5307D	26.50	1.89	50.16
5307E	25.89	1.96	50.80

Table 6. Tensile testing of $[0/90]_8$*, Emery cloth*

5.1.3 Properties

Fiber Volume Fraction	Specimen ID	Young's Modulus [GPa]	Avg Young's Modulus [GPa]	Max Strength [MPa]
47%	**47 02 A**	102.18	105.49	Not Valid Due to Tab Sliding
	47 03 B	103.96		
	47 01 B	111.57		
	47 03 A	107.25		
	47 02 B	102.51		
50%	**50 02 A**	122.29	117.48	
	50 01 A	117.42		
	50 04 A	114.70		
	50 01 B	116.43		
	50 02 B	116.54		
53%	**53 03 A**	122.50	120.57	
	53 02 A	118.85		
	53 02 C	118.37		
	53 02 B	120.97		
	53 01 C	122.15		

Table 7.Tensile Properties of $[0]_6$*, tab sliding*

Fiber Volume Fraction	Specimen ID	Young's Modulus [GPa]	Strength [MPa]
47%	47-06D	55.00	876.5
50%	50-07C	58.91	909.2
53%	53-07C	58.58	922.8

Table 8. Tensile Properties of $[0/90]_8$*, Emery Cloth*

Fiber Volume Fraction	Specimen ID	Young's Modulus [GPa]	Avg Young's Modulus [GPa]	Max Strength [MPa]	Avg Max Strength [MPa]
47%	**4704B**	113.68	110.89	1199.4	1410.4
	4701C	109.57		1549.8	
	4702C	106.29		1576.0	
	4703C	102.86		1299.2	
	4704C	122.05		1427.8	
50%	**5002C**	129.09	121.99	1828.5	1740.2
	5003B	111.77		1683.3	
	5004B	120.88		1652.9	
	5003C	121.40		1790.6	
	5004C	126.79		1745.8	
53%	**5304A**	125.91	120.21	1462.0	1455.6
	5303B	118.69		1508.9	
	5304B	118.87		1354.2	
	5303C	119.23		1465.8	
	5304C	118.33		1486.9	

Table 9. Tensile Properties of $[0]_6$, Emery cloth

Fiber Volume Fraction		Young's Modulus [GPa]	Avg Young's Modulus [GPa]	Max Strength [MPa]	Avg Max Strength [MPa]
47%	**4706A**	55.00	56.19	927.0	901.8
	4706B	57.17		873.7	
	4706C	53.30		876.4	
	4706E	59.29		929.9	
50%	**5008A**	58.92	60.28	860.3	899.5
	5008B	60.52		906.1	
	5008D	60.17		850.1	
	5008E	61.50		981.4	
53%	**5307A**	58.58	60.39	994.0	967.0
	5307B	63.07		918.2	
	5307D	60.85		997.3	
	5307E	59.04		970.4	

Table 10. Tensile Properties of $[0/90]_8$, Emery cloth

5.1.4 Fractured Specimens

Note: Not necessarily in order as the table

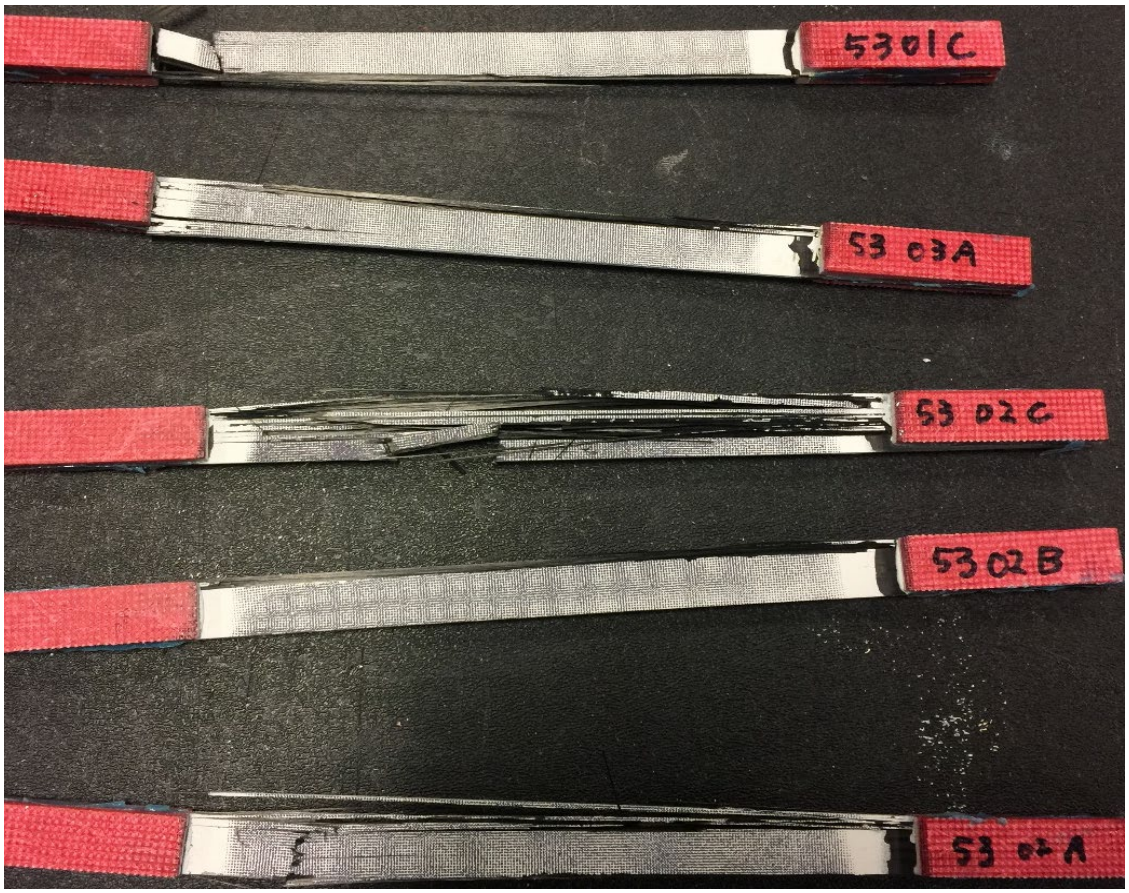

Figure 14. Tensile testing of $[0]_6$, tab sliding

Figure 15. First tensile test on $[0/90]_8$ samples, 47, 50, and 53% respectively.

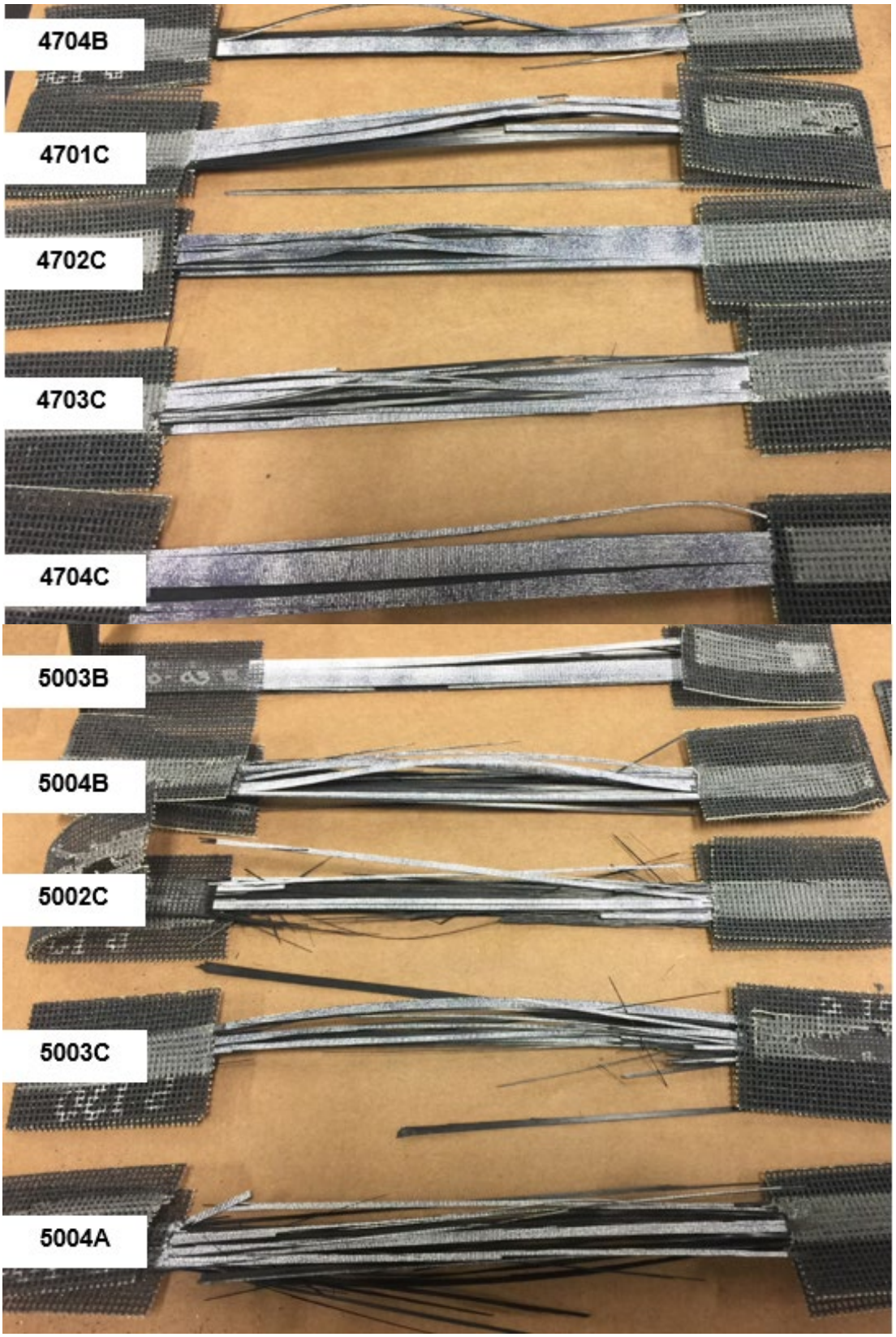
4704B
4701C
4702C
4703C
4704C
5003B
5004B
5002C
5003C
5004A

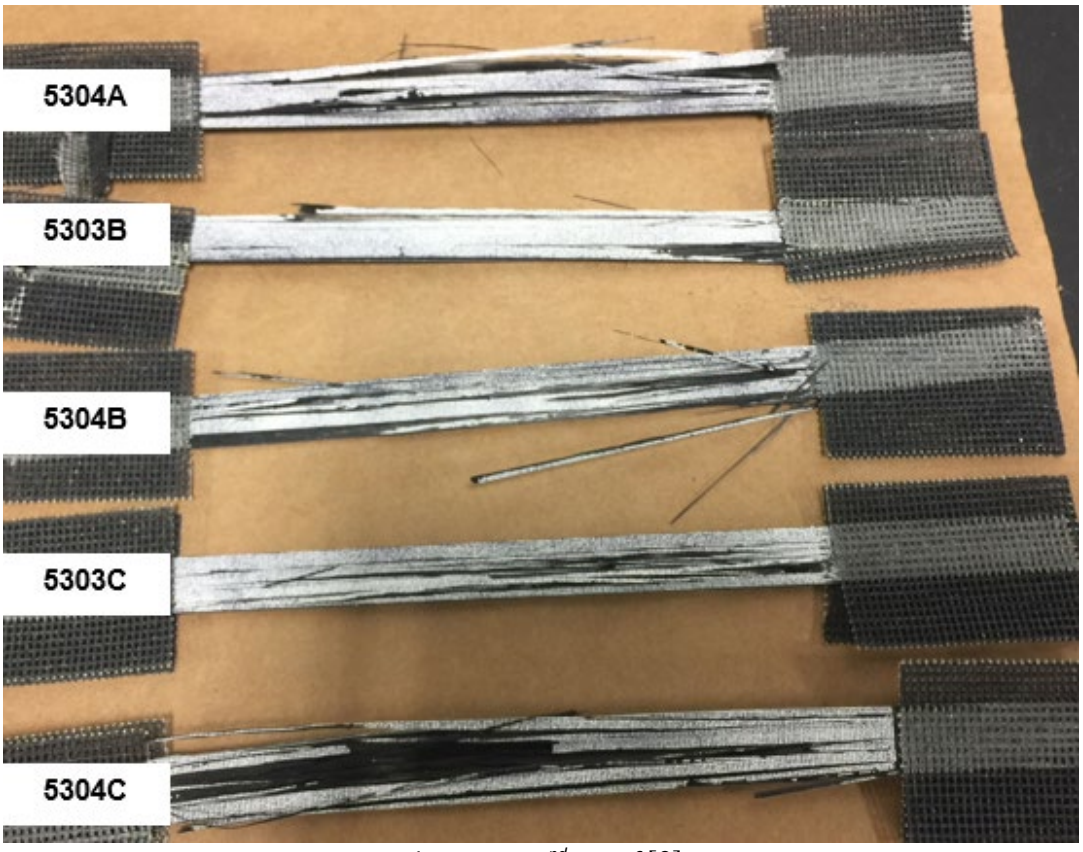

Figure 16. Tensile Test on 2nd set of $[0]_6$ *specimens*

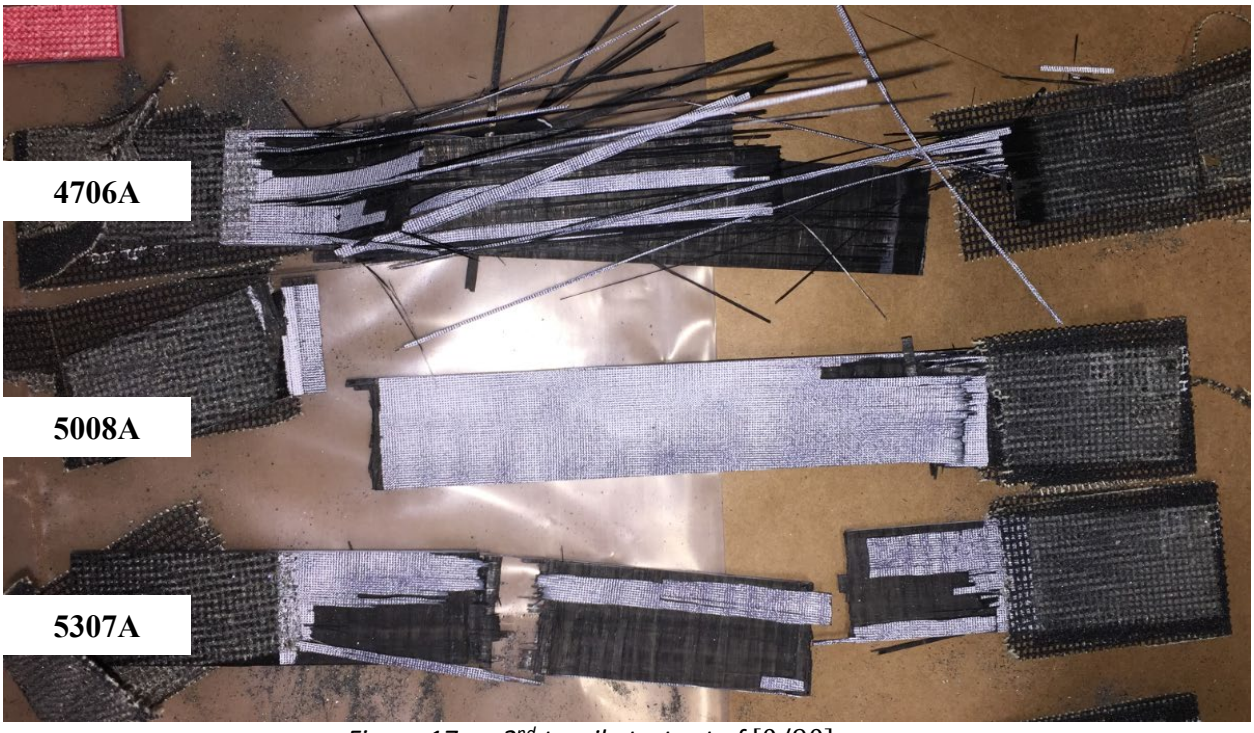

Figure 17. 2nd tensile test set of $[0/90]_8$

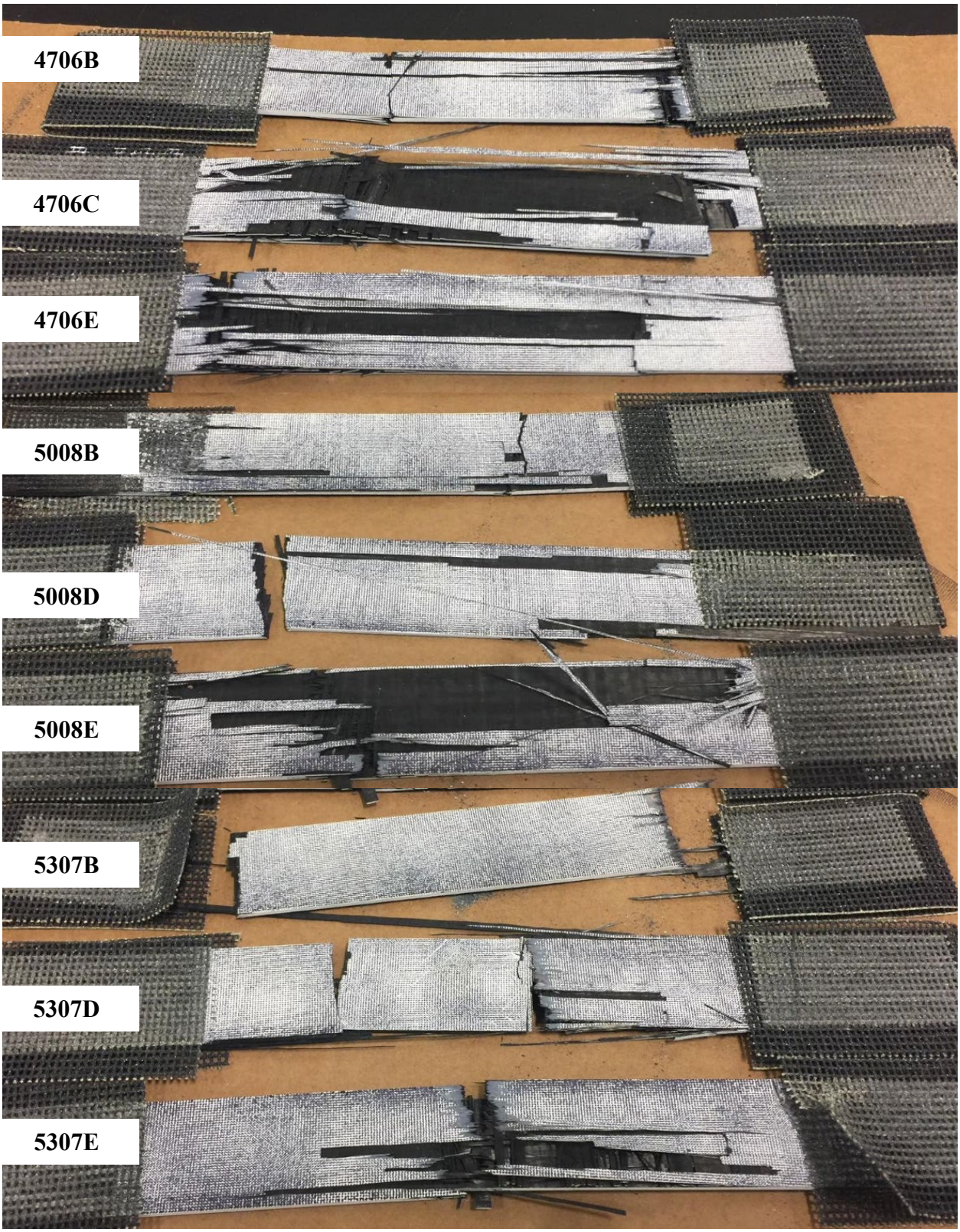

Figure 18. Last set of tensile testing for $[0/90]_8$

5.2 Tensile Testing of RFF Plates

5.2.1 Summary

After the tensile testing with FIBRTEC coupons are complete, the 10.5'' by 10.5'' plates from DuPont are prepared for tensile testing. According to clarification from DuPont, plate B is supposed to be 0/90 and D is supposed to be 45/-45, but B is cut to be 45/-45 plate. However, this does not matter because A, B, D, and E are identical plates. Therefore, plate A is cut into 4, specimens of width 2 inch with waterjet. One mistake occurred from this process because the MTS grip's width was about 1.75 inch such that it was not fully gripping the test specimens. So, each specimen was cut again to get 4 coupons of 1 inch. All of the testing are done with emery cloth in the grips of the MTS machine.

As for second plate, Plate D, 9 inch specimens are prepared and tested using DIC and emery cloth. The Young's Modulus is again calculated using 0.002 to 0.005 strain values. The testing result shows inconsistent result in sample 1 and 4 for plate A. During the testing, both specimens had very early fracture on the outside, but the inner fibers were still intact. Due to the sudden drop of the load, the MTS stopped, giving very low strength values.

5.2.2 Dimensions

	Avg Width [mm]	**Avg Thickness** [mm]	**Cross sectional Area** $[mm]^2$
A-1	25.40	1.14	29.04
A-2	25.40	1.18	30.04
A-3	25.40	1.18	30.06
A-4	25.40	1.13	28.74
D-1	25.25	1.09	27.52
D-2	25.24	1.11	28.10
D-3	25.25	1.12	28.36
D-4	25.24	1.13	28.6
D-5	25.23	1.13	28.43
D-6	25.25	1.14	28.78
D-7	25.23	1.12	28.35
D-8	25.25	1.12	28.28
D-9	25.24	1.13	28.52

Table 11. Tensile testing of RFF specimens from Plate A

5.2.3 Properties

	Young's Modulus [GPa]	**Strength** [MPa]
A-1	55.97	802.6
A-2	68.69	1055.2
A-3	66.57	993.8
A-4	66.01	617.8
D-1	53.92	756.6
D-2	58.48	813.3
D-3	65.10	1022.2
D-4	66.13	778.3
D-5	54.97	718.4
D-6	65.68	1084.1
D-7	69.38	736.0
D-8	59.96	1005.4
D-9	48.26	684.1

Table 12. Tensile Properties of RFF specimens from Plate A

5.2.4 Fractured Images

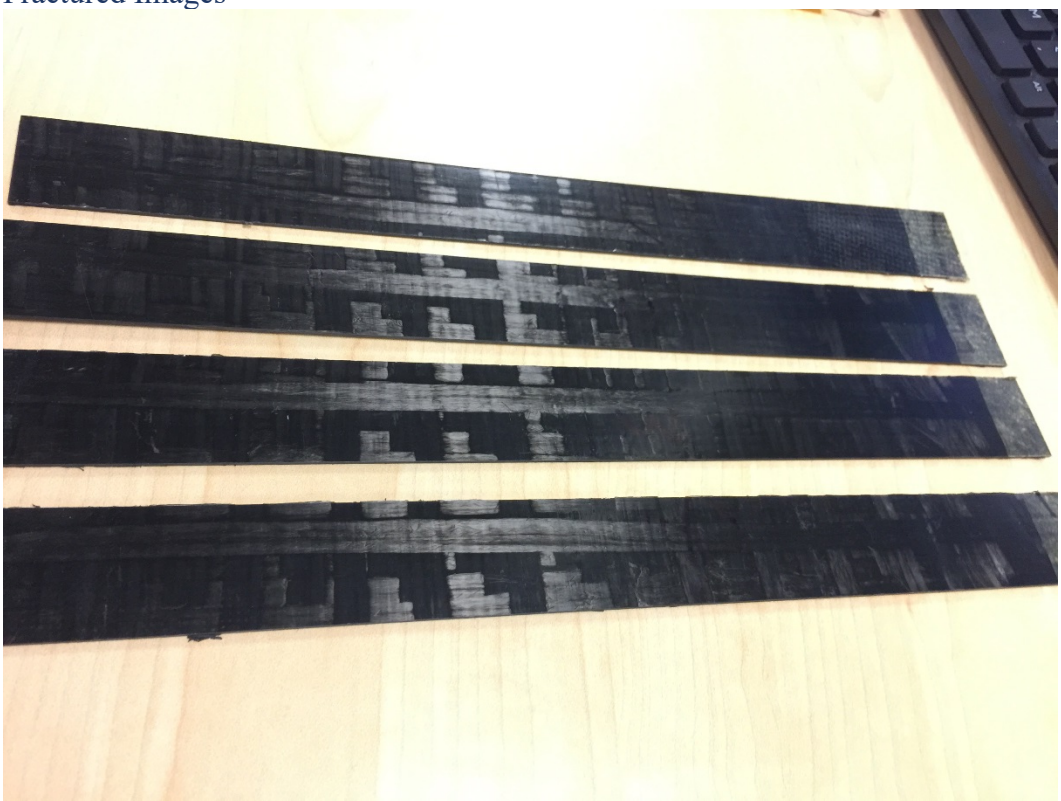

Figure 19. Test Plate A

Figure 20. Test Plate A after test

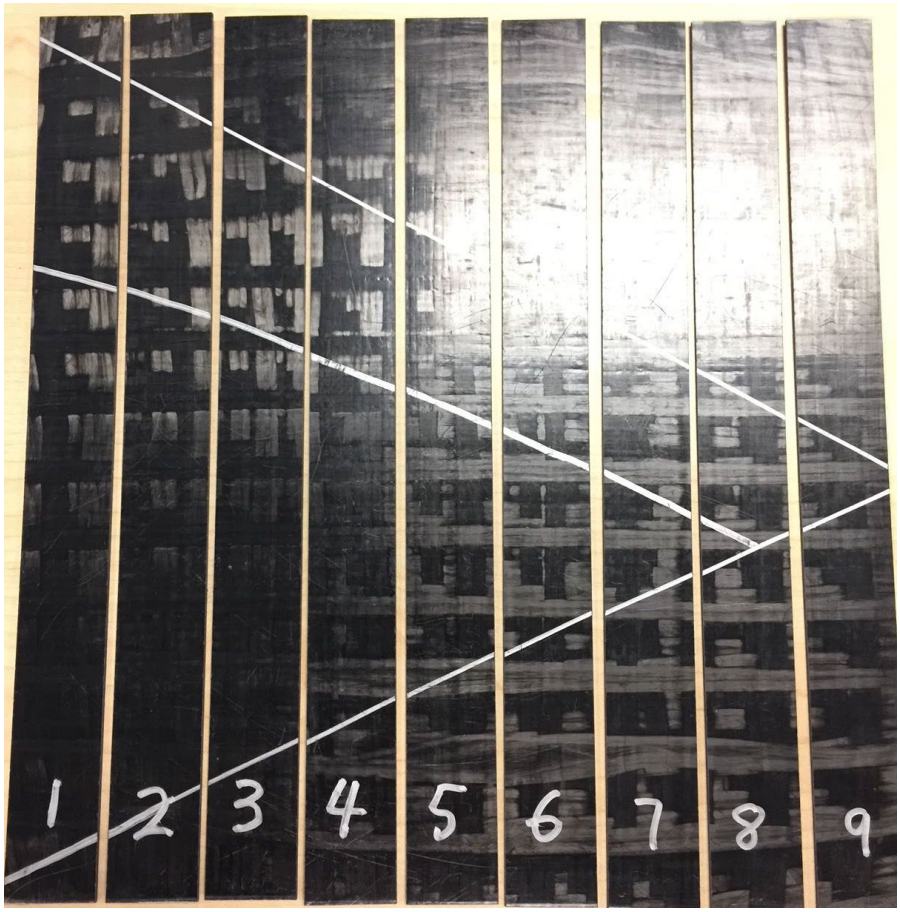

Figure 21. Test Plate D

Figure 22. Plate D after testing – 1 through 9 respectively

5.3 Double Cantilever Beams Testing

5.3.1 Summary

In the experiment mode I fracture toughness has been determined for the RFF composite fabric using modified beam theory, compliance calibration and the modified compliance calibration methods and the resistance plots are then plotted. The results are further compared for different theories. Flexure modulus has also been determined using the experiment. The test method was developed for unidirectional laminates and RFF material does not satisfy the criteria and hence these results do not satisfy the test criteria. Also, it was observed that the crack did not propagate completely on the mid plane due to the undulations of the RFF material which was again a condition in the test criteria.

The coupons were prepared using Plate F from DuPont, and 1 inch coupons are cut. 4 samples were tested. In second set of tests hinges were moved 1 in closer to reduce the active crack length but the resulting force was so higher that the hinges popped out. In third set of tests the hinges were moved 0.5 in closer instead of 1 in but same hinge popping phenomenon was observed. Out of 4 successful failure samples, 2 samples gave low values of initiation fracture toughness whereas the other two gave high values of initiation fracture toughness. The lowest value of initiation fracture toughness is displayed in table 2. There was a significant increase in fracture toughness with the increase in crack growth due to fiber bridging. Also, some samples failed in bending instead of crack propagation which implies the samples should be made thicker or should be glued with metal bars at the end to avoid failure in bending. It should be noted that a 70 micron thick Teflon insert was used for the crack instead of recommended 13 micron insert.

5.3.2 Experimental setup

Piano hinges are then bonded on the laminate with the help of epoxy as shown in the image below.

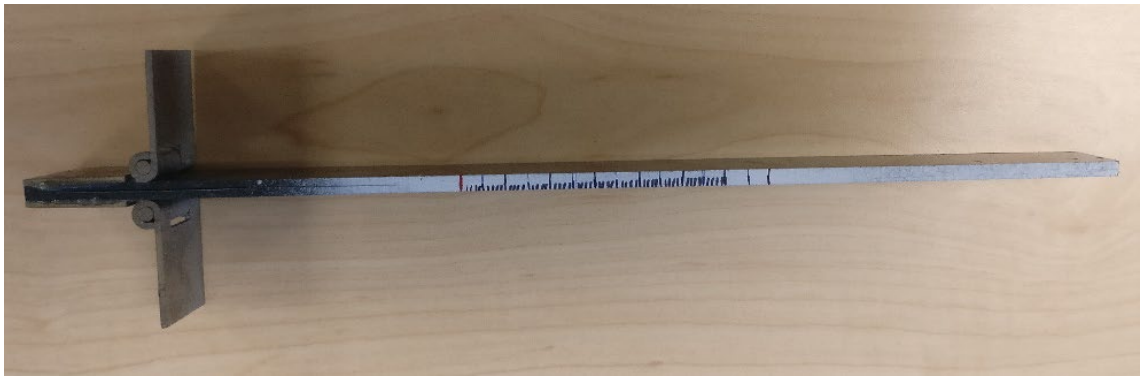

Figure 23. DCB specimen before testing

For the mechanical testing of the laminate paint the side of the laminate with contrasting paint (i.e., white enamel paint or anything that makes sense) if necessary and a metric scale is drawn. The dimensions of the laminate and the initial crack length are then measured with the help of calipers.
The test was done on a displacement control mode and the ramp rate was 0.15 in/min. The recommended ramp rate as per the standard is from 0.02 in/min to 0.2 in/min and the used ramp

rate lies between the recommended standard values.
Only one cycle was done for the DCB testing and the force corresponding to crack growth was measured. The standard recommends measuring the force for first every 1 mm of crack growth till 5 mm and then unloading the specimen and then loading it back and measuring the force every 5 mm of crack growth but the growth of crack in RFF material is very unstable and the crack almost grows instantaneously making the measurements at certain intervals very difficult.

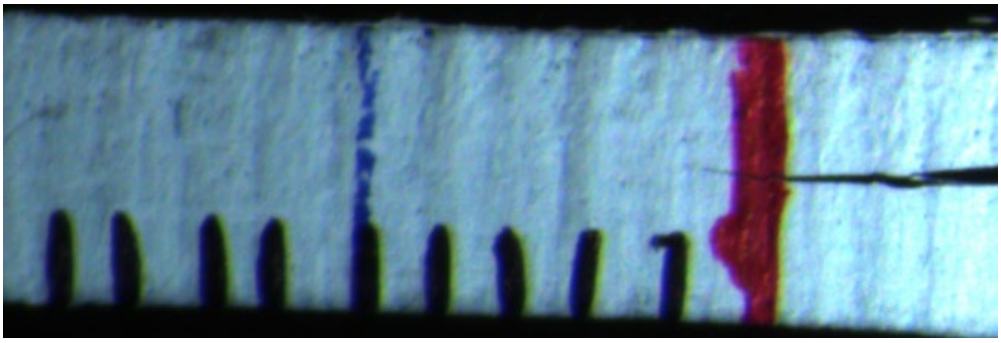

Figure 24. Crack growth taken from microscope camera

5.3.3 Dimensions

Sample #	Average width, W (mm)	Average thickness, h (mm)	Initial a_0 (mm)
1	23.32	3.70	48
2	25.42	3.71	48.4
3	25.43	3.73	48
4	25.34	3.76	47

Table 13. Dimensions of DCB specimens from Plate F

5.3.4 Results

Sample No.	G_{IC} (J/m^2)
1	972
2	855
3	1444
4	1429

Table 14. Mode I fracture toughness result

The graphs below shows the force displacement curve for the experiment for all the 4 samples tested.

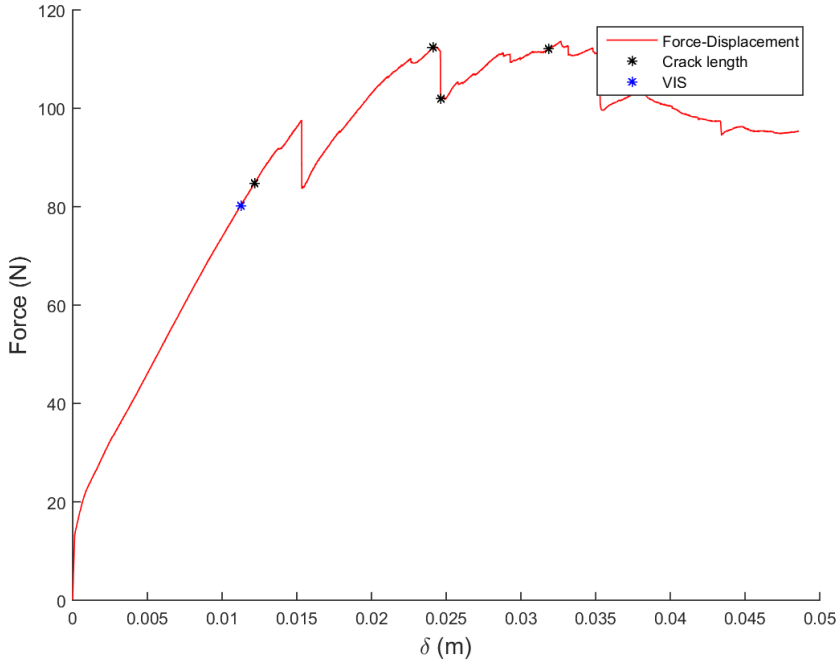

Figure 25. Force Displacement graph for sample 1

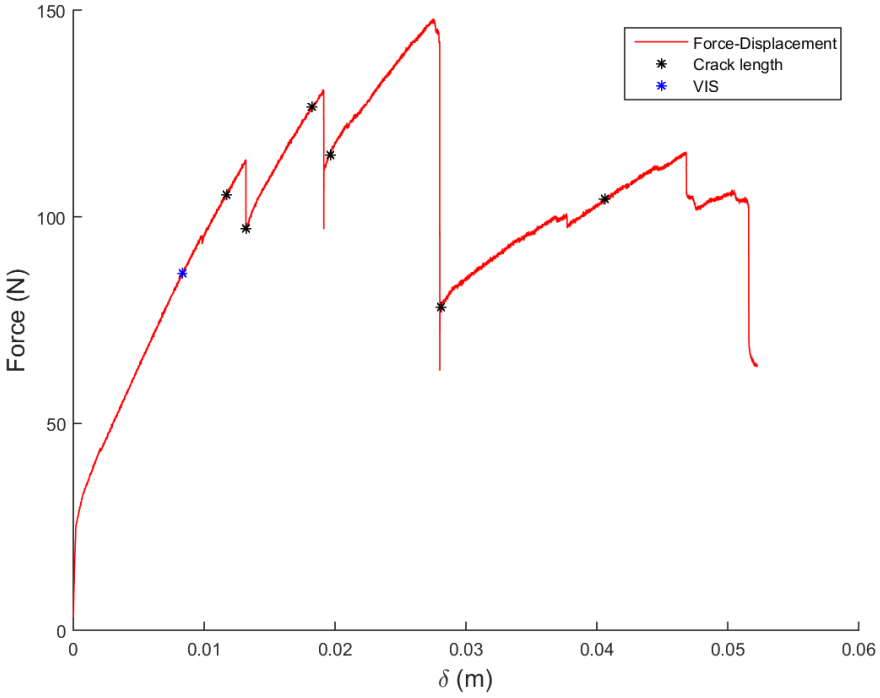

Figure 26. Force Displacement graph for sample 2

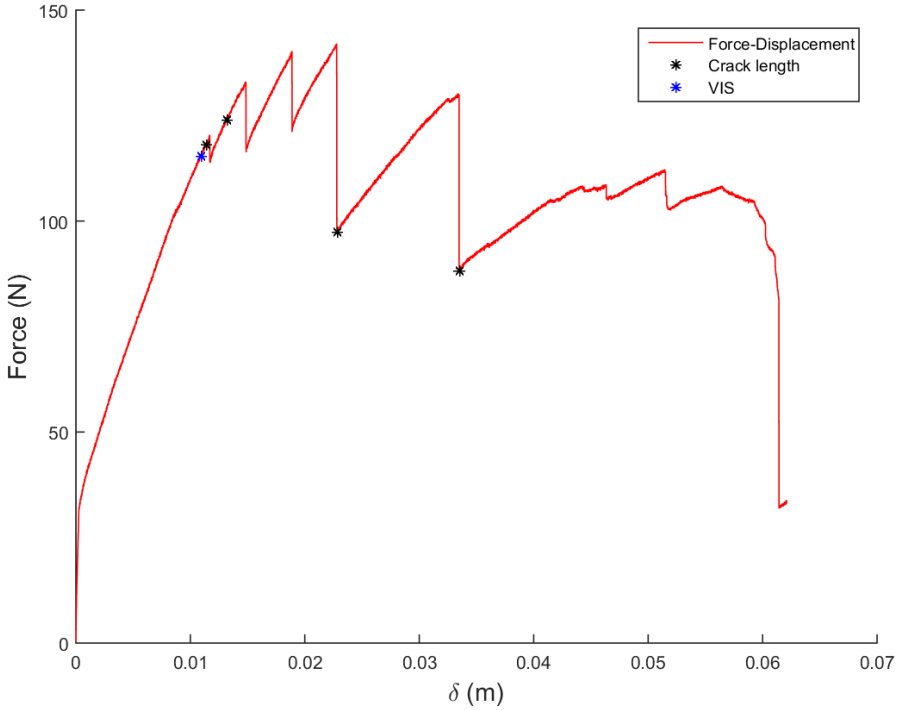

Figure 27. Force Displacement graph for sample 3

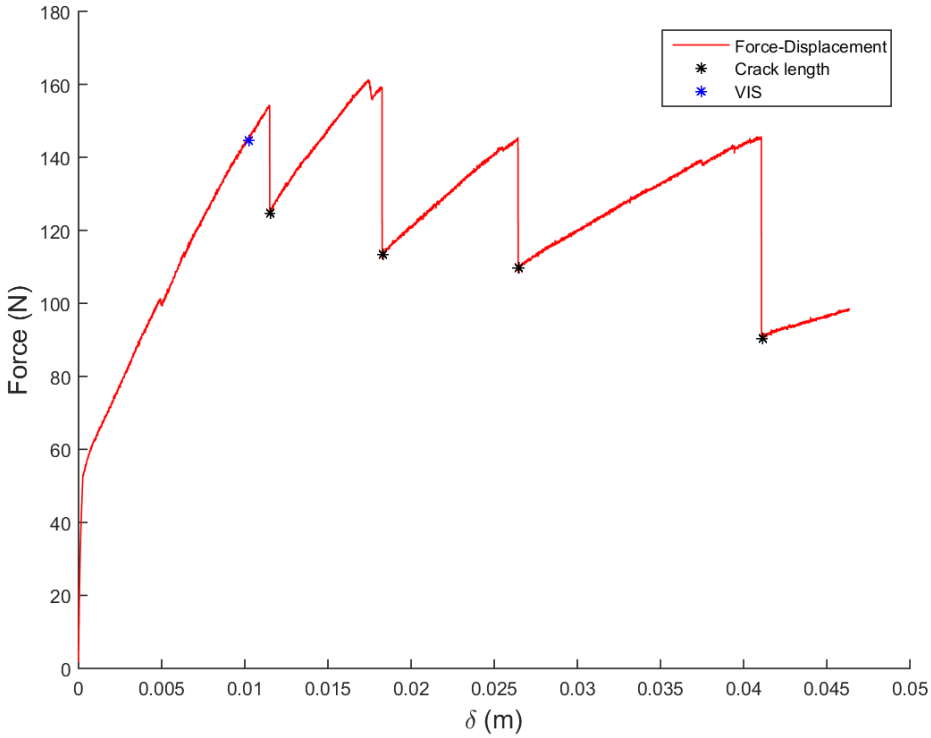

Figure 28. Force Displacement graph for sample 4

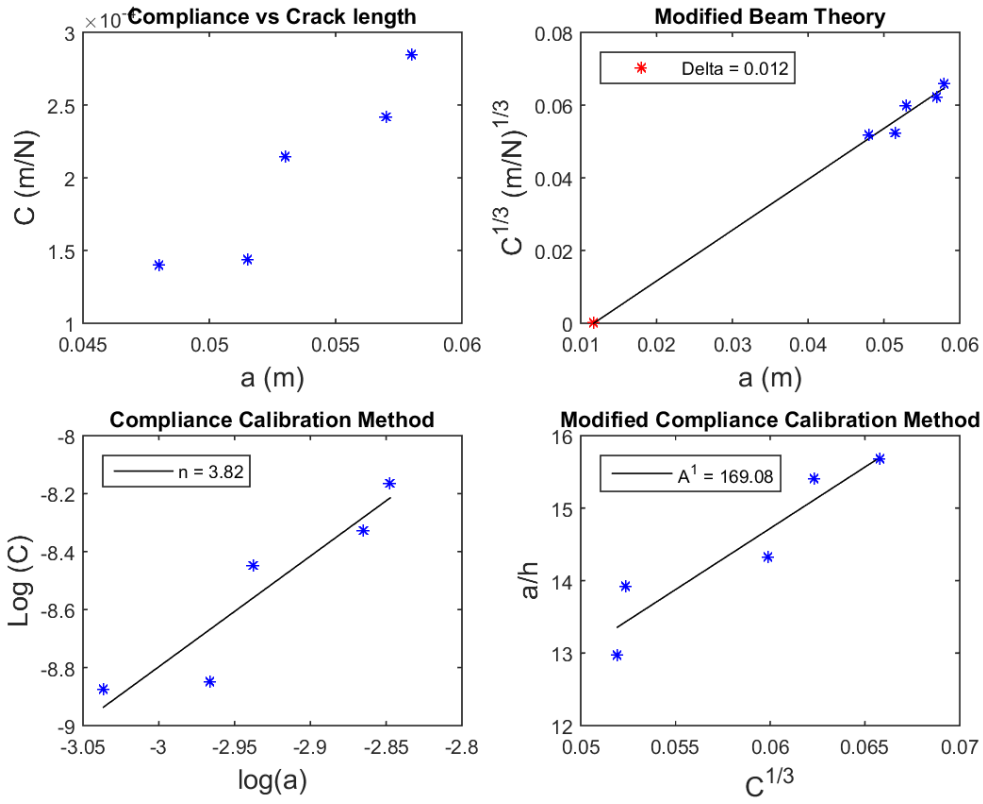

Figure 29. Data Reduction for sample 1

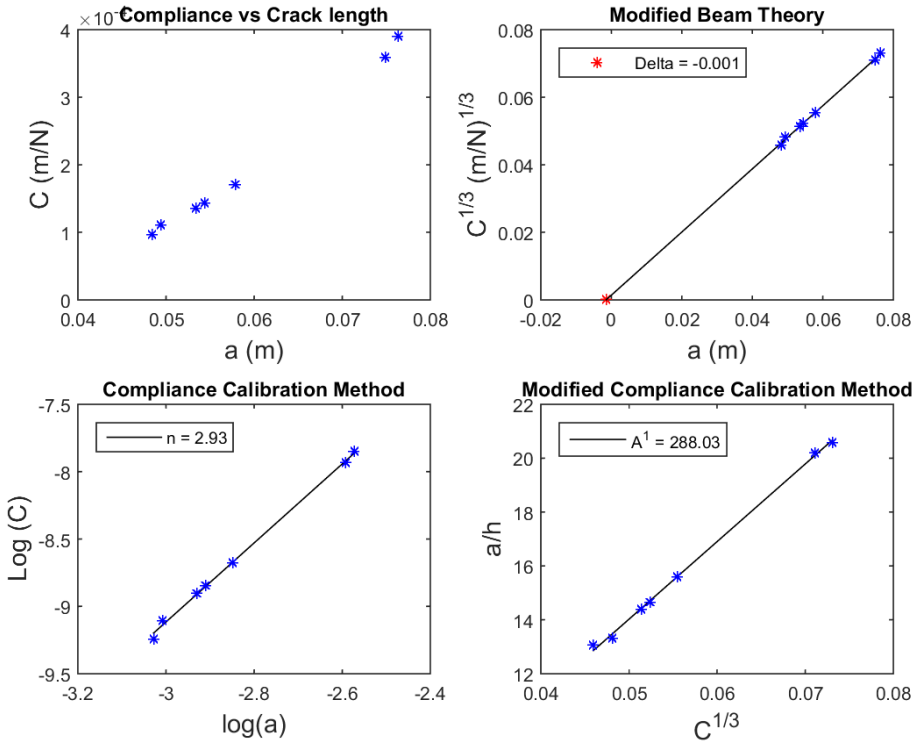

Figure 30. Data Reduction for sample 2

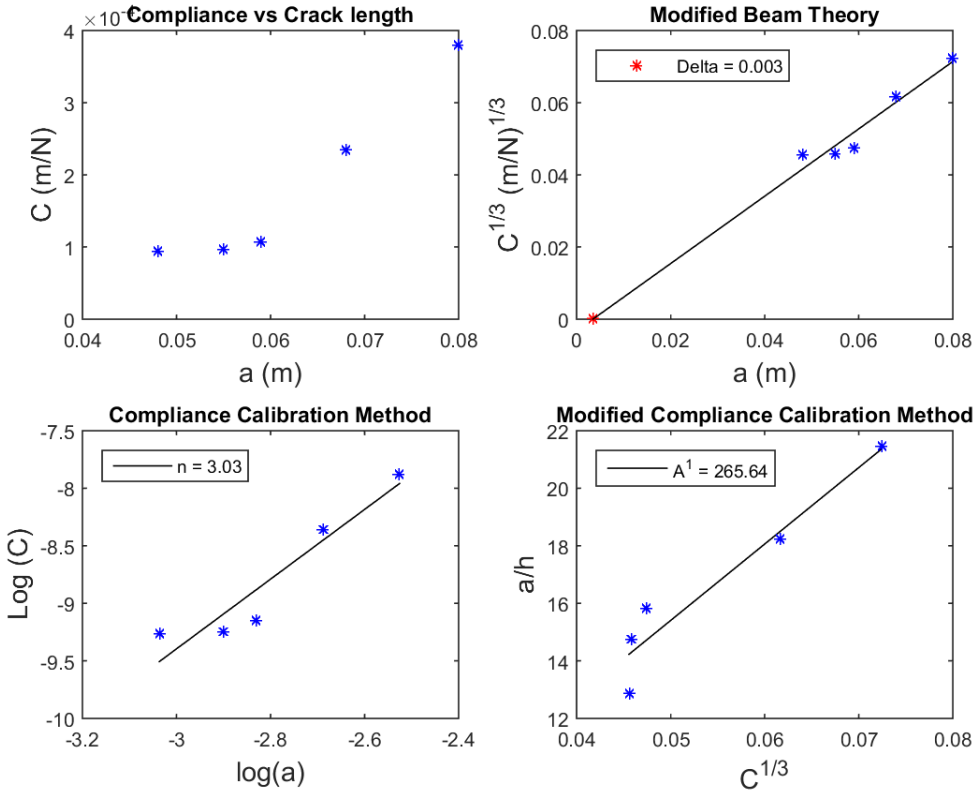

Figure 31. Date Reduction for sample 3

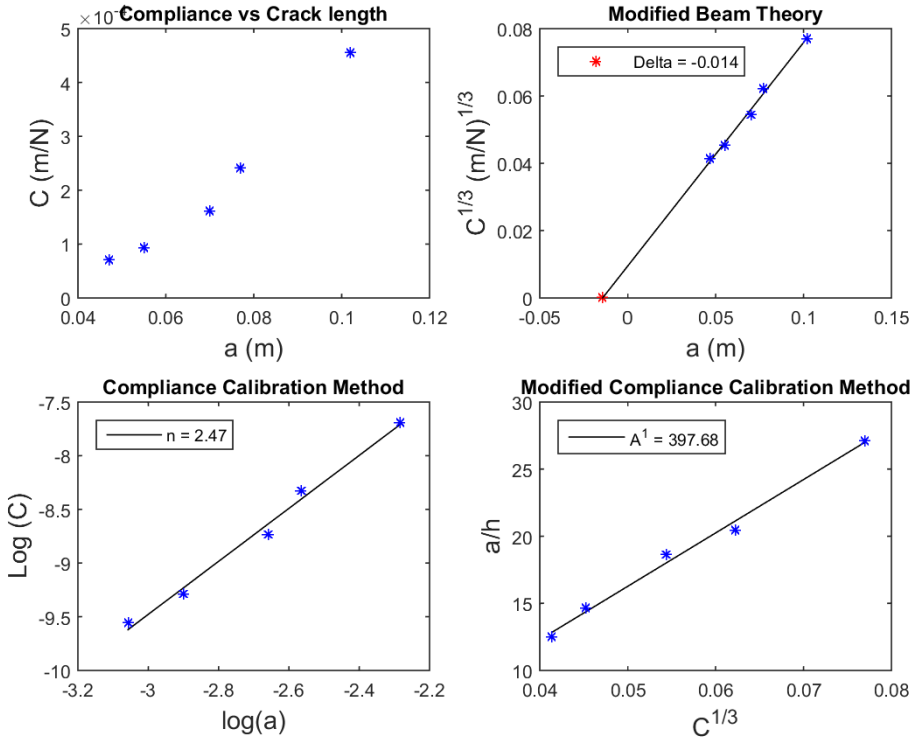

Figure 32. Date Reduction for sample 4

5.3.5 Images

The images below show the crack propagation surface and some of the specimens failing in bending instead of further crack propagation. Also, for some specimens bending failure was observed before any crack propagation and no data could be obtained from them. Hence, only 4 samples gave good results.

Figure 33. Crack surface to the right of white line

Figure 34. Specimen failing in bending before crack propagation

5.4 Compression Testing

5.4.1 Summary

Two sets of compression testing were done to find the compression modulus and the compressive strength due to high standard deviation in compressive strength in the first set due to tab sliding. Strain gauges were attached on both sides of the sample to check for any kind of buckling behavior and buckling was observed before the samples failed. Due to covered field of view from the compression fixtures DIC was not used to measure the strain but instead strain gauges were used to measure the strain in the samples. The gauge length was kept at 1 in to eradicate tab end effects. The thin samples were from Plate C from DuPont, and in addition, the coupons that failed in bending from the DCB testing were recycled in the compression tests as these samples were thicker than the plate C.

We first thought that the coupons from DCB testing would have enough thickness to avoid buckling behavior, but still buckling behavior was observed. Nonetheless, buckling behavior was observed for the coupons from plate C.

5.4.2 Test apparatus

IITRI fixture for compression testing was used to perform the test. The sample was mounted between the shear grips and checked for parallelism with the grips. The grips were then loaded into the loading blocks and the fixture was then placed in the MTS machine for the compression testing.

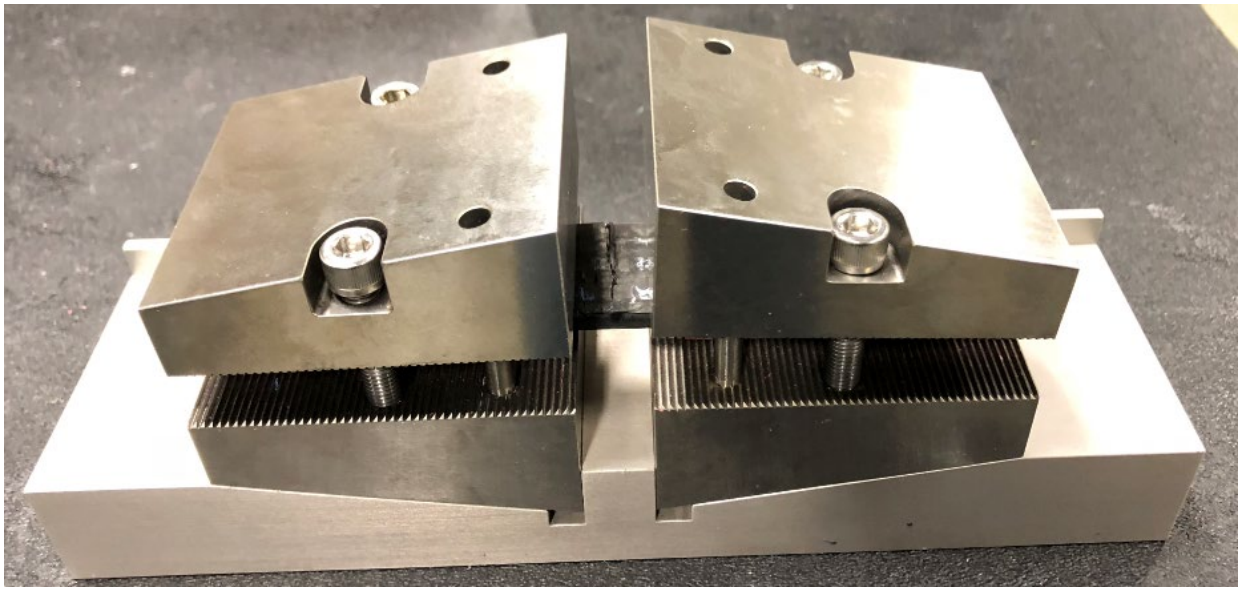

Figure 35. IITRI Fixture used to align sample

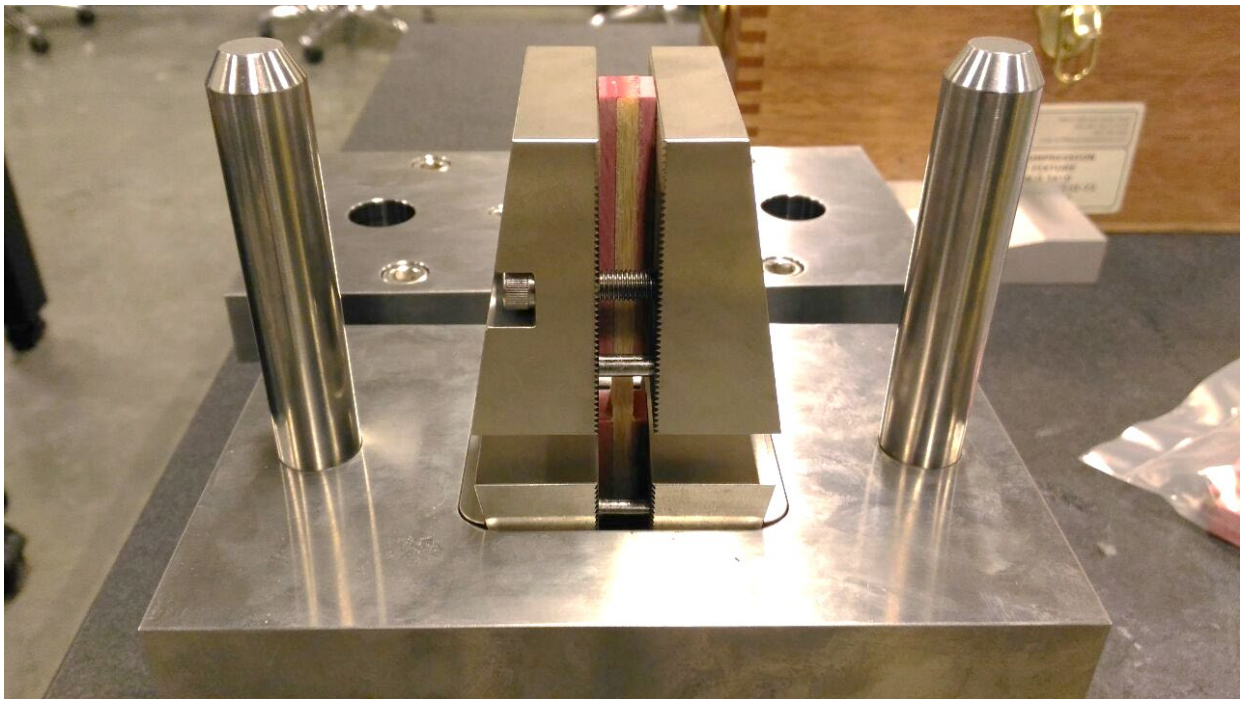

Figure 36. IITRI Fixture before loading

Figure 37. IITRI Fixture used in compression testing

5.4.3 Dimensions

	Sample Number.	**Width** [mm]	**Thickness** [mm)	**Gauge length** [in]
Thick	1	25.35	3.70	1.0
	2	25.21	3.72	1.0
	3	25.21	3.71	1.0
	4	25.2	3.78	1.0
	5	25.2	3.71	1.0
	6	25.07	3.78	1.0
Thin	7	25.55	1.9	0.5
	8	24.81	1.88	0.5
	9	25.38	1.9	0.5

Table 15. Dimensions for Compression testing specimens

5.4.4 Results

Samples 1, 2, 7, 8, and 9 are tested first, but there was tab sliding observed with sample 2 and 7. This could be because the urethane adhesive has been past expiration date, so new urethane adhesive is used to prepare samples 3 through 6 and also coarser grit is used to roughen up the surface touching the tabs. Lastly, more clamps are used to apply equal pressure over the tabs. These extra processes successfully prevented the tabs from sliding.

1 inch gauge length was chosen in order to avoid the End-effects where the strain gauge can touch the edge of the tabs if the gauge length is small. However, this led to the samples often buckling right before fracture. Although the modulus $\boldsymbol{E_{1c}}$ can be calculated, the maximum strength might not properly represent the actual strength of the specimens.

Sample Number	**Strength** [MPa]	$\boldsymbol{E_{1c}}$**(SG1)** [GPa]	$\boldsymbol{E_{1c}}$**(SG2)** [GPa]	**Avg.** $\boldsymbol{E_{1c}}$ [GPa]
1	256.1	45.55	54.43	49.99
2	272.0	47.40	68.70	58.05
3	227.0	54.65	46.08	50.36
4	240.0	59.99	67.14	63.06
5	248.0	60.30	50.55	55.42
6	242.0	67.20	55.69	61.44
7	195.6	47.11	48.18	47.65
8	340.7	49.26	52.11	50.69
9	259.5	53.53	NA	NA

Table 16. Compressive Modulus

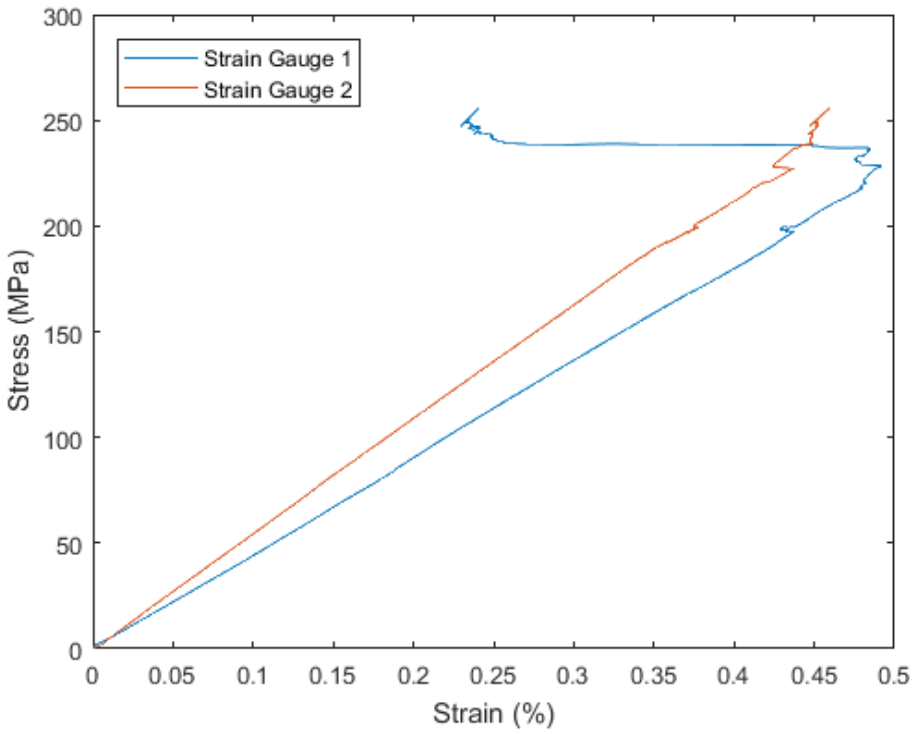

Figure 38. Sample 1 – Buckling observed / fractured

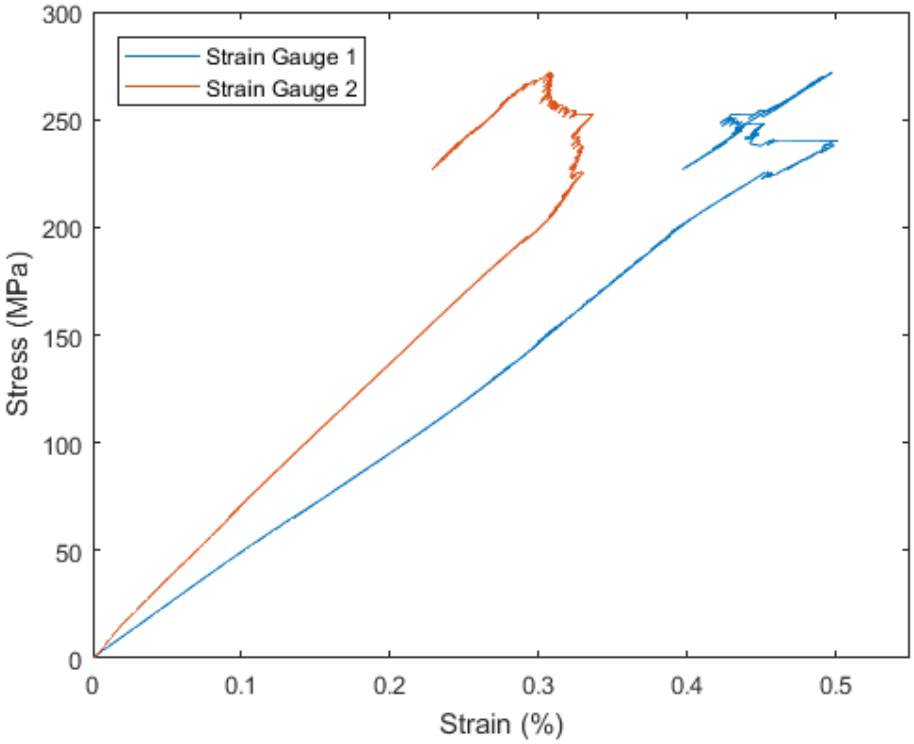

Figure 39. Sample 2 – Tab sliding / Not fracture

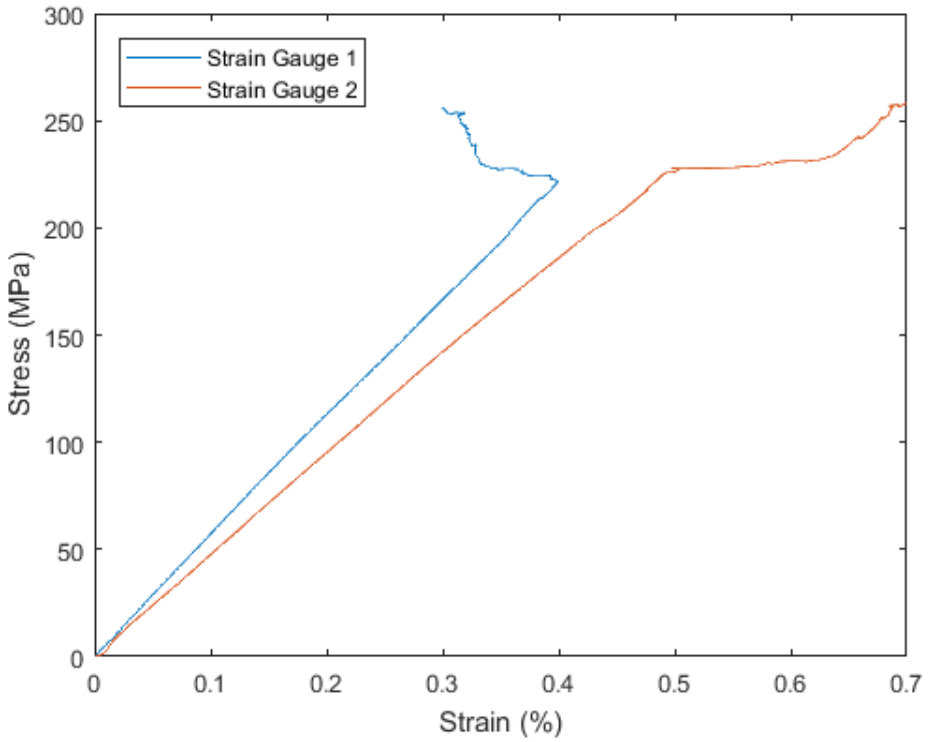

Figure 40. Sample 3 – Buckling / Fractured

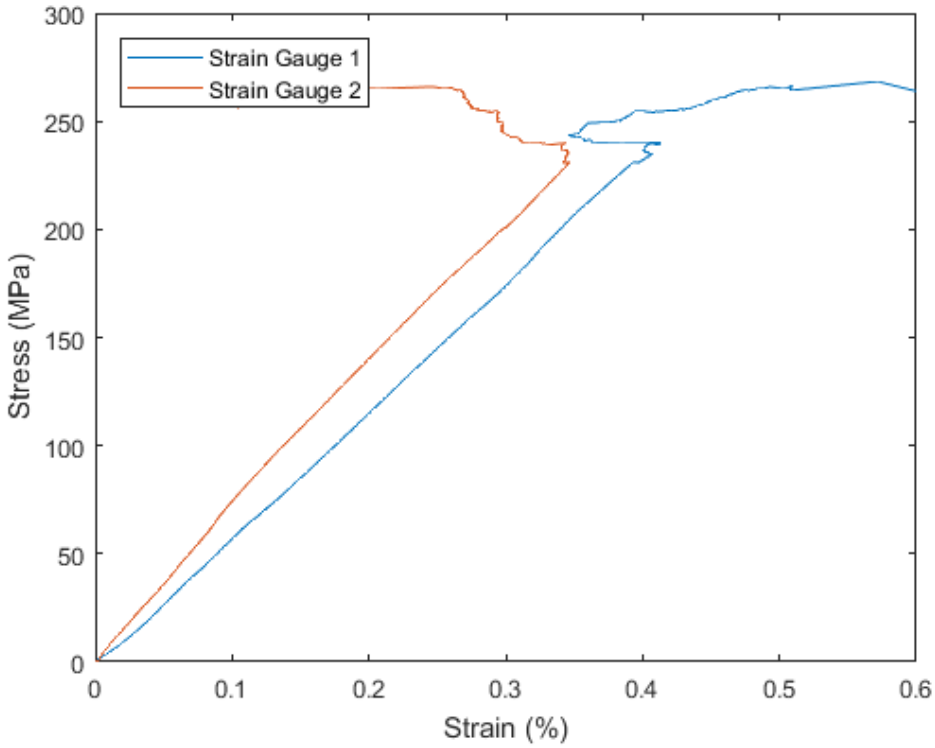

Figure 41. Sample 4 – Buckling / Fractured

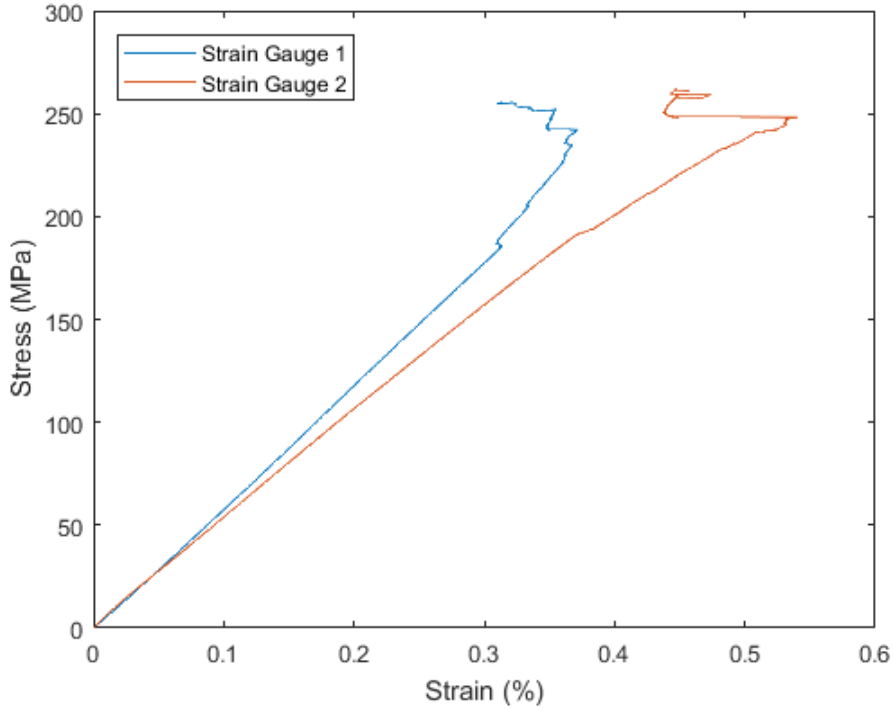

Figure 42. Sample 5 – Buckling / Fractured

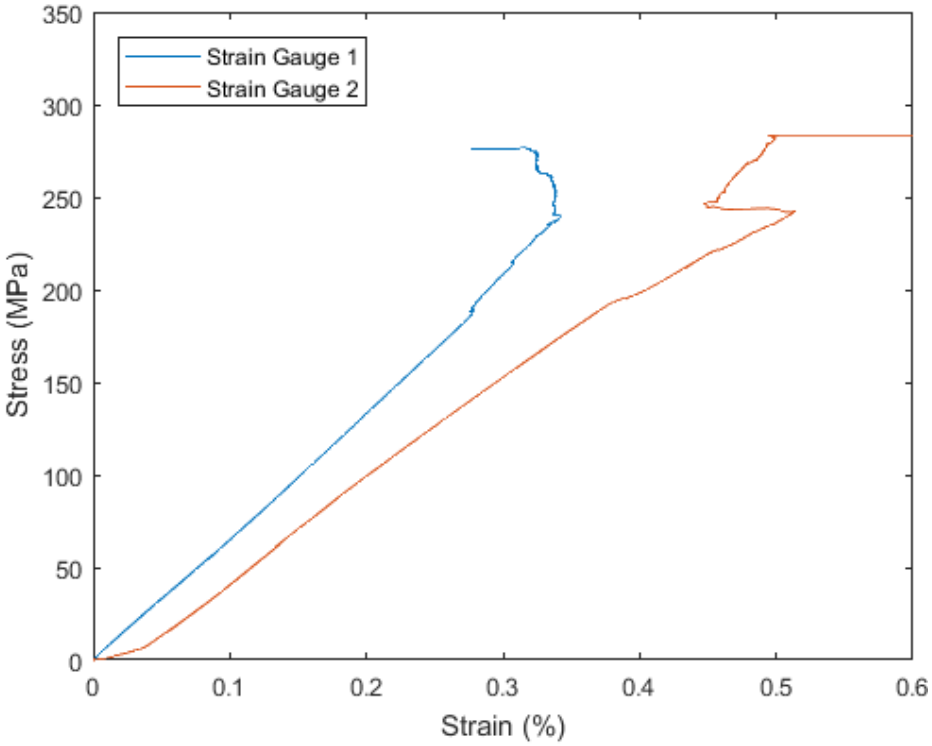

Figure 43. Sample 6 – Buckling / Fractured

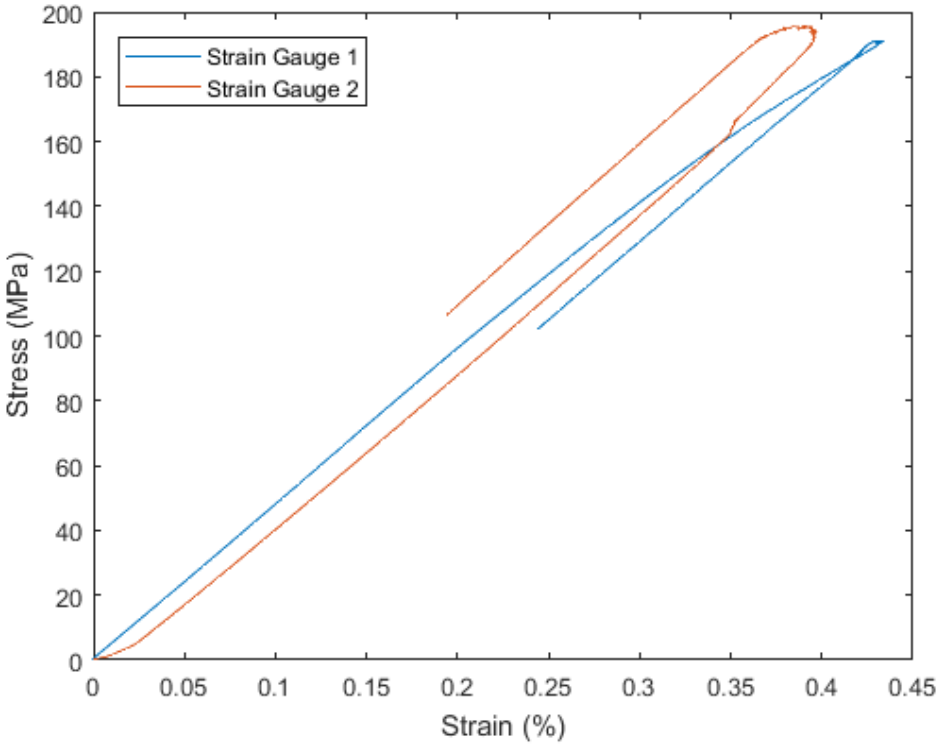

Figure 44. Sample 7 - Tab Sliding / Not Fractured

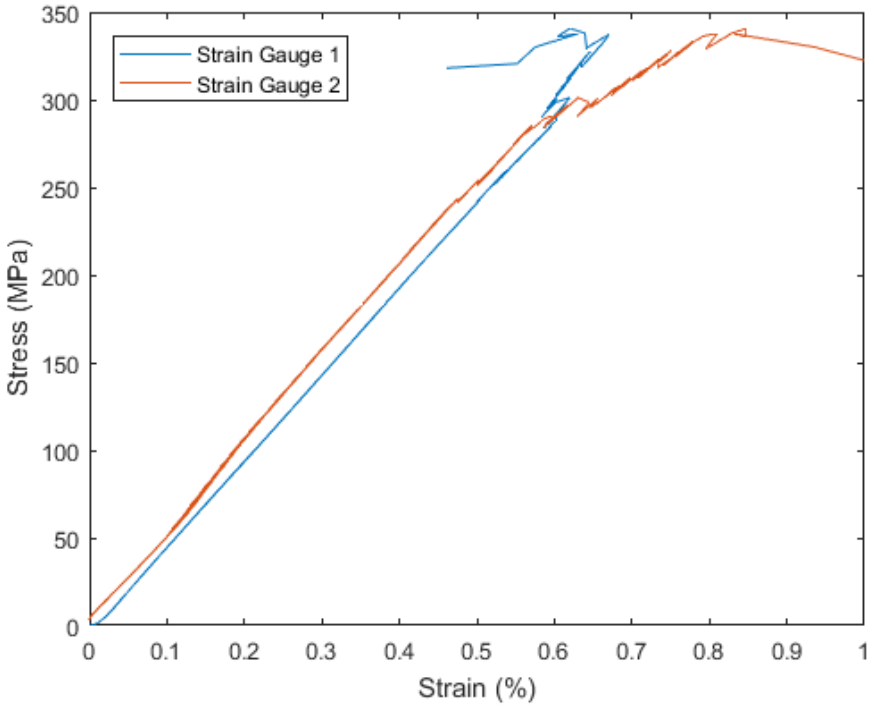

Figure 45. Sample 8 – No Buckling / Fractured

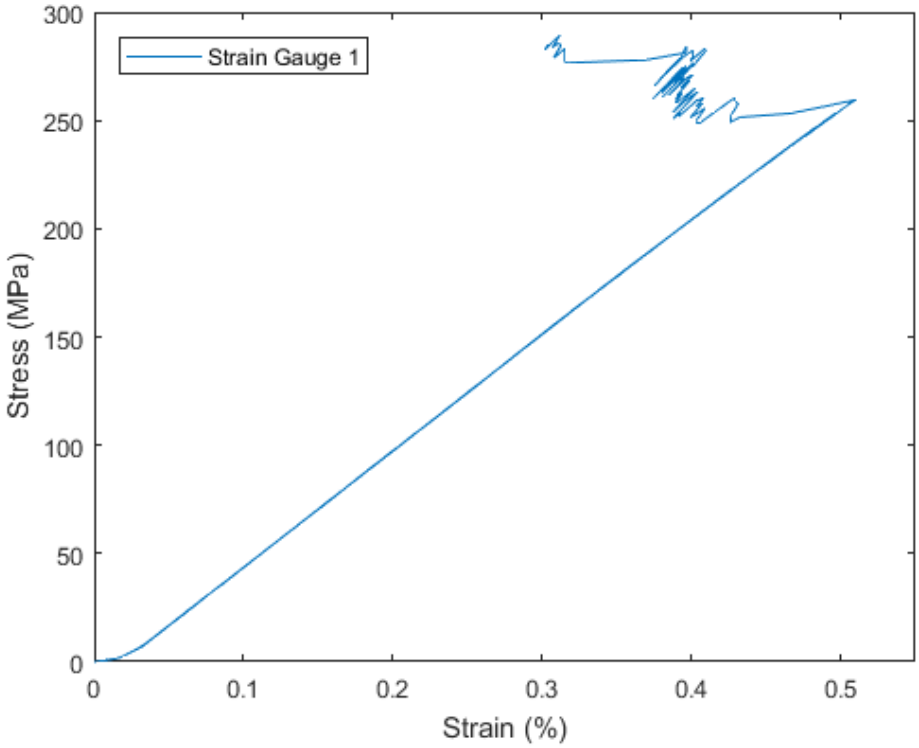

Figure 46. Sample 9 – Buckling / Fractured – strain gauge fell off while mounting

5.4.5 Fractured Images

Figure 47. Fractured Compression 1 inch gauge length samples from 1 to 6 respectively

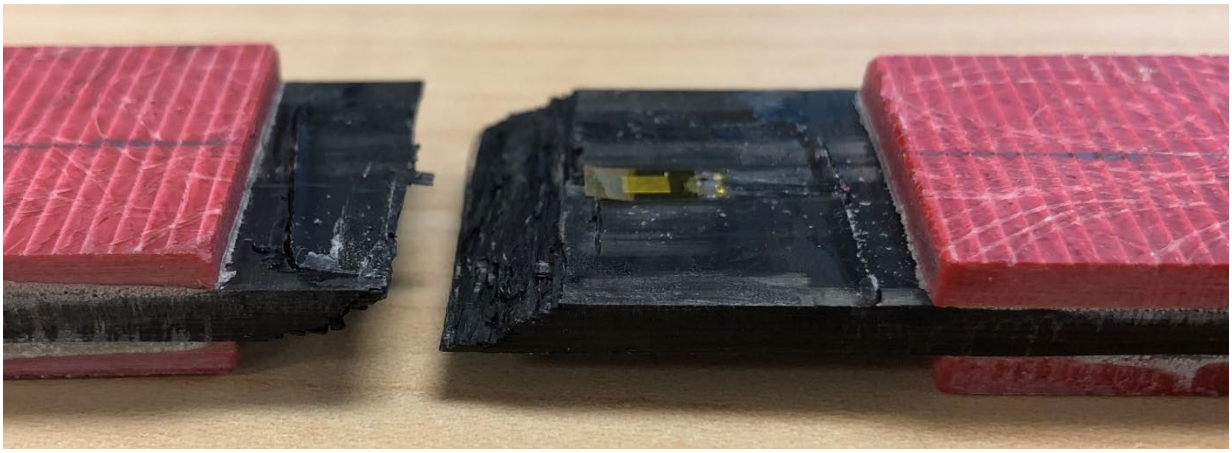

Figure 48. Sample 1 Fractured image

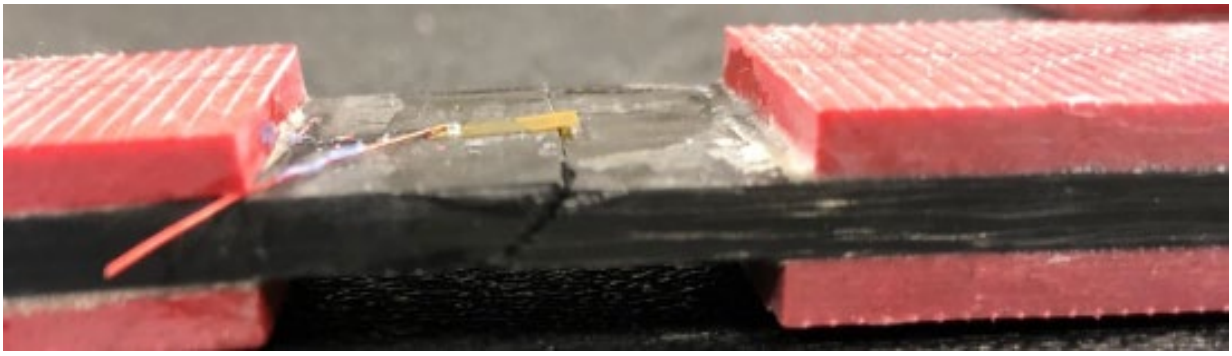

Figure 49. Sample 3 Fractured

Figure 50. Sample 4 Fractured Image

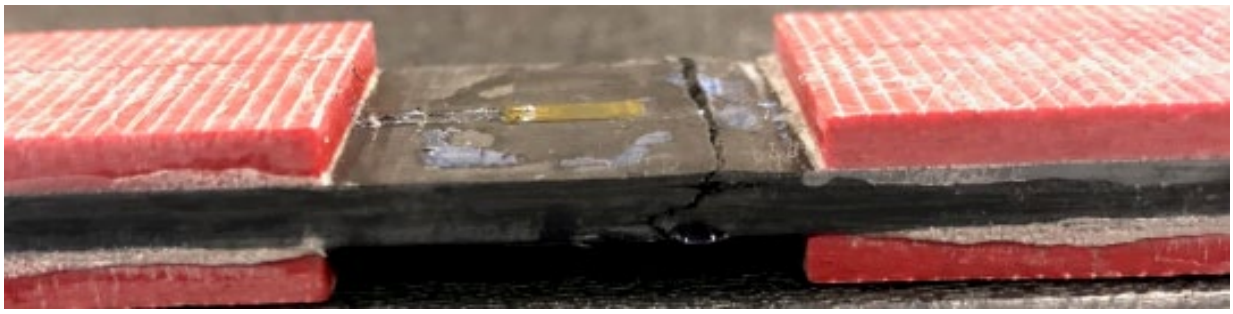

Figure 51. Sample 5 Fractured Image

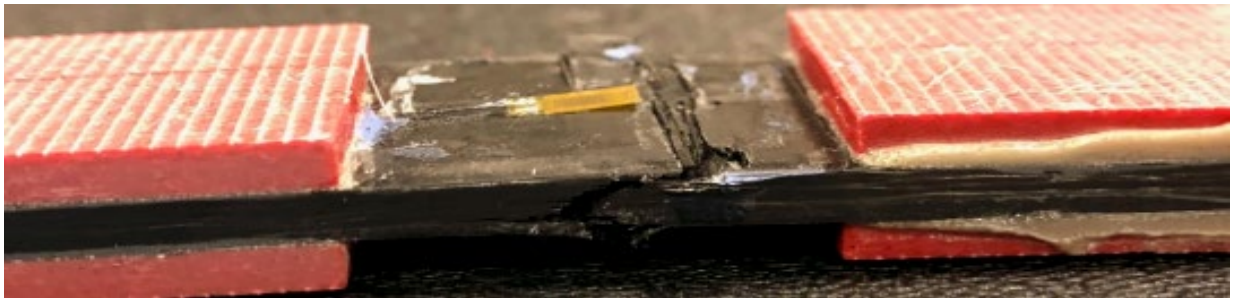

Figure 52. Sample 6 Fractured Image

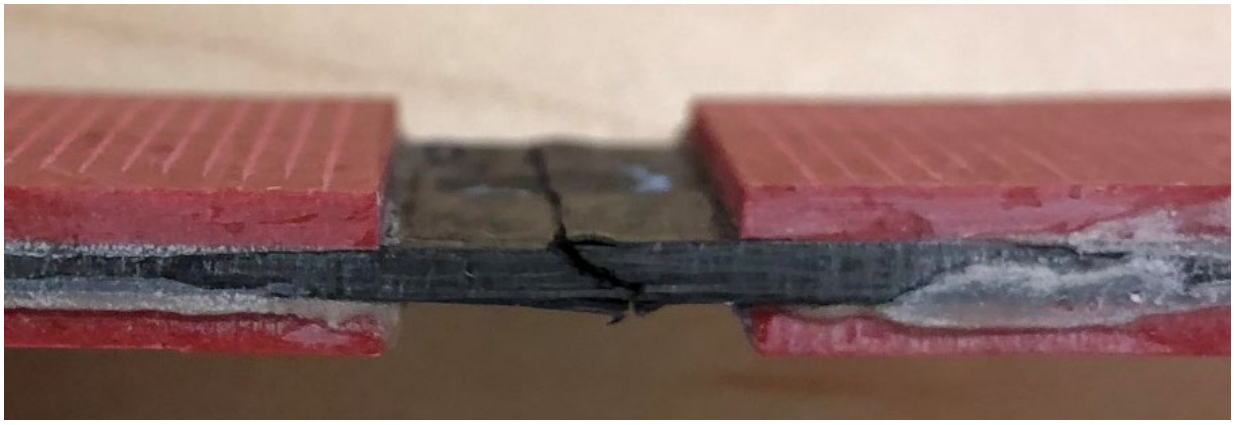

Figure 53. Sample 8 Fractured Image

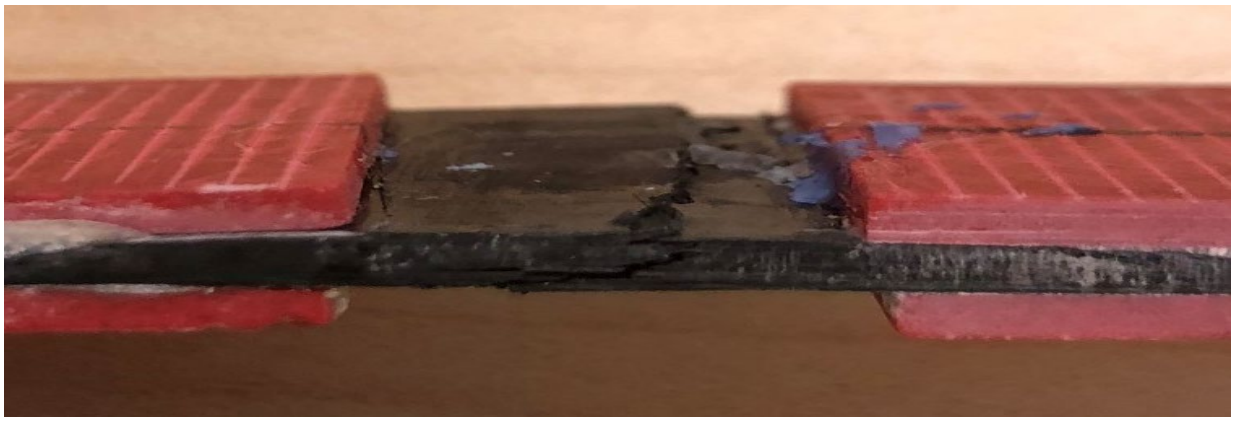

Figure 54. Sample 9 Fractured Image

5.5 End Notched Flexure Testing

5.5.1 Summary

Because we observed that the interlaminar stiffness is higher than bending stiffness from DCB testing, we were not confident that the End Notch Flexure testing would be successful. So, from plate G, we cut out 4 of 1 inch coupons and tested them first. Although sample 1 crack successfully propagated interlaminarly, the rest 2~4 samples did not and failed in bending at the loading pin. This was following the ASTM standard to load 20, 30, and 40mm from the crack tip. 5 More samples from the same plate was cut and this time, the loading was applied on 10, 20, and 30 mm from the crack tip. The procedure is load a certain amount, up to 500 N for our case, for the first and last measurements, then load until fracture for the middle measurement. The first and third measurements are to find the compliance of the material, and then the second measurement is to find the fracture toughness of Mode II. If the crack propagates, then new 10, 20, and 30 mm marks are made and loaded again in the pre-cracked condition.

Even after changing the measurements down to 10, 20, and 30 mm, the crack did not propagate. Specimen 5 failed in bending this time as well. So, next solution was to decrease the span length, the distance between the two pins on the bottom. Originally, 4 inches span length is recommended by the ASTM standard, but since this does not work, we decreased the span length to 3 inches. After making two modifications, the interlaminar crack finally started to propagate, so the non-pre-cracked and pre-cracked fracture toughness could be found.

5.5.2 Dimensions

Sample Number.	**Avg Width** [mm]	**Avg Thickness** [mm]	**Cross sectional Area** $[mm]^2$
6	3.64	25.36	92.31
7	3.73	25.40	94.65
8	3.74	25.33	94.73
9	3.75	25.36	95.17

Table 17. Dimensions of ENF testing coupons from Plate G

5.5.3 Results

Sample ID	Non-PreCrack G_{IIc} $[J/m^2)$	PreCrack G_{IIc} $[J/m^2]$
6	2192	2790
7	1977	4415
8	2353	2830
9	2763	4348

Table 18. Mode II Fracture Toughness, Non Pre-cracked and Pre-cracked

5.5.4 Fractured Images

The first 5 specimens were used to find out the correct testing conditions due to the failure in bending of the RFF coupons. So, data were collected and post processed for only coupons 6 through 9.

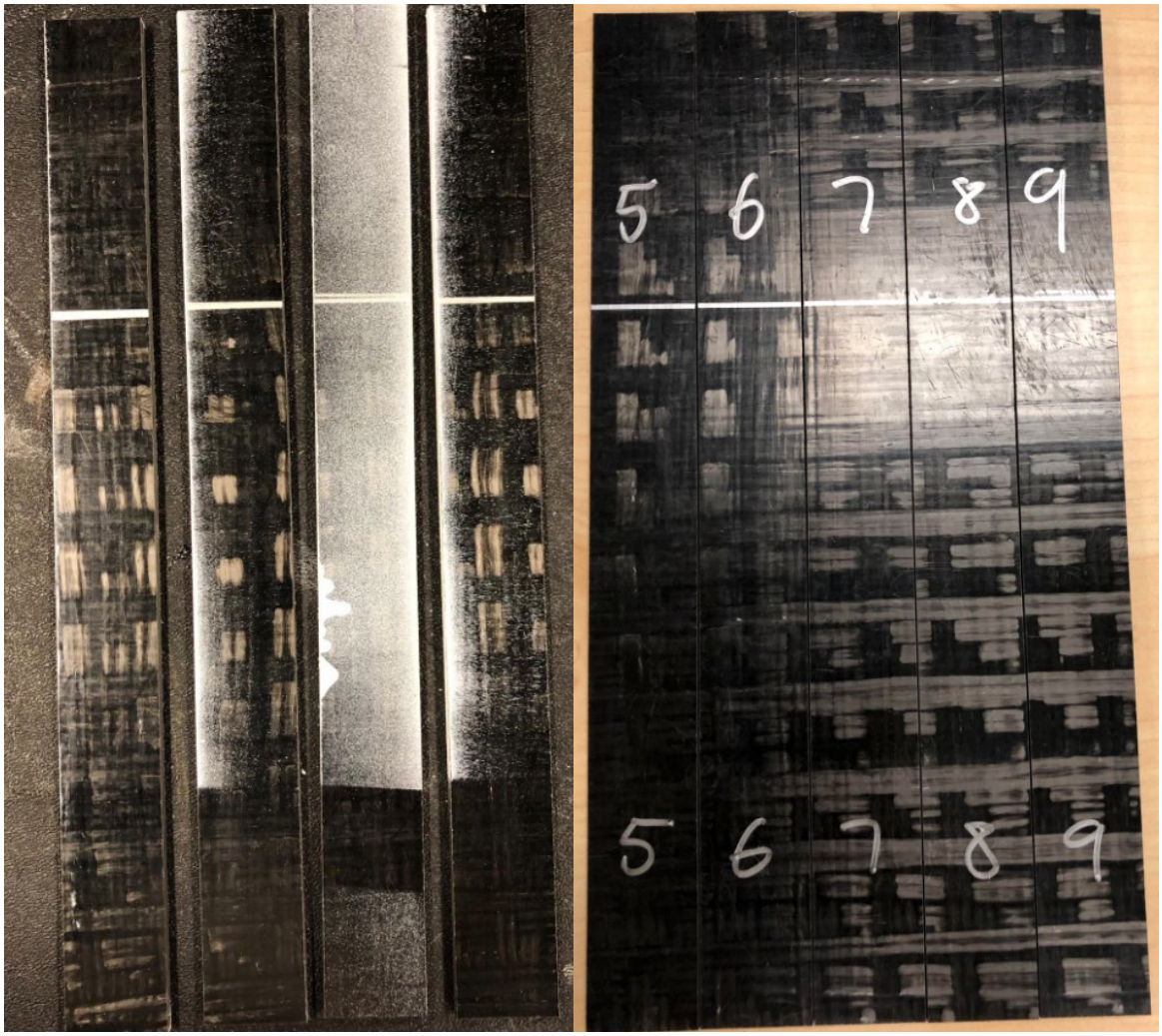

Figure 55. 9 Coupons cut from Plate G.

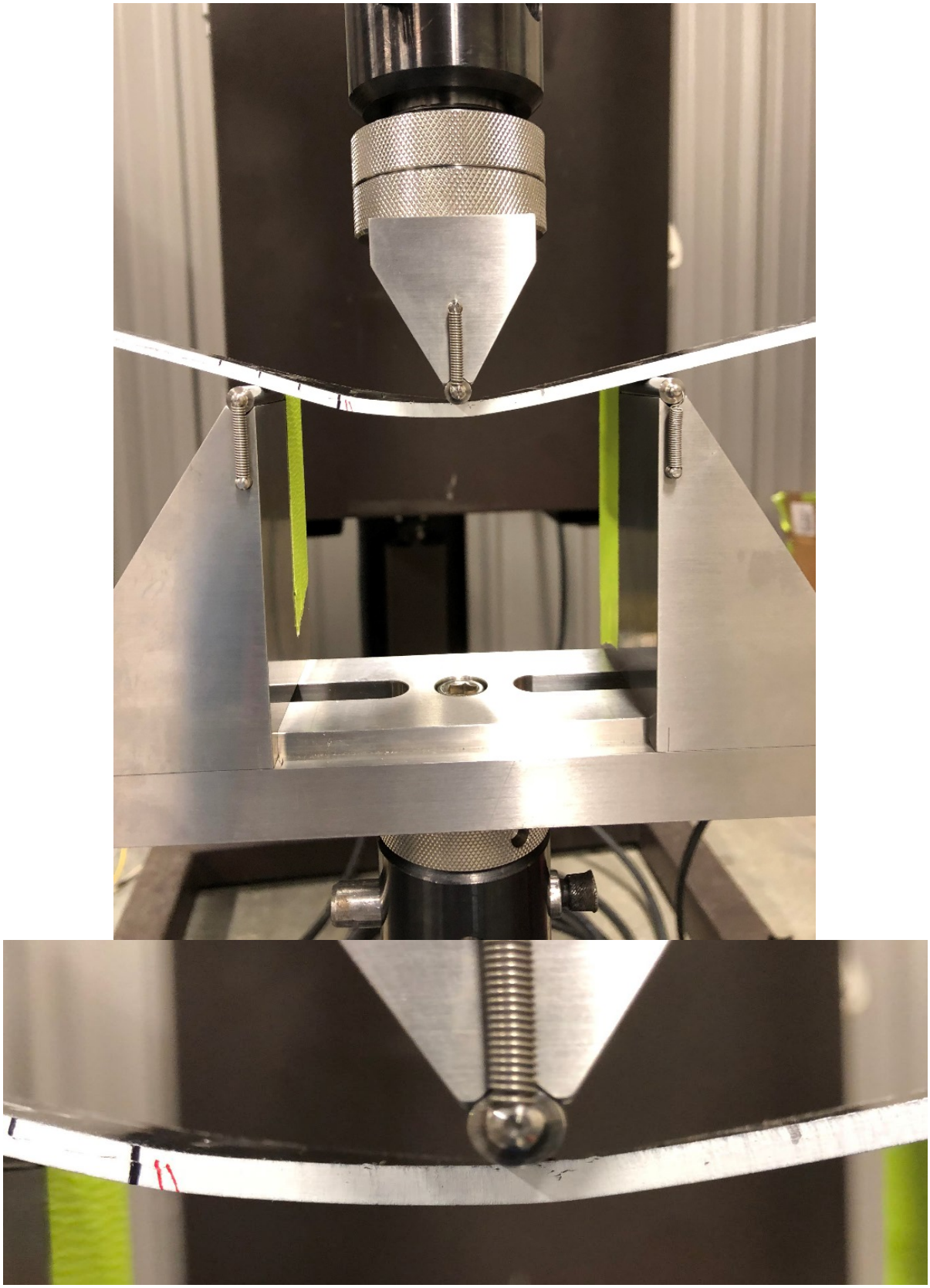

Figure 56. Specimen 2 failing in bending at the top loading pin + Magnified failure view

Figure 57. Magnified view of failure by bending

The formation of the crack happens at about 45 degrees from the pin. This behavior indicates that the crack is generated by mixture of failing in shear and compression.

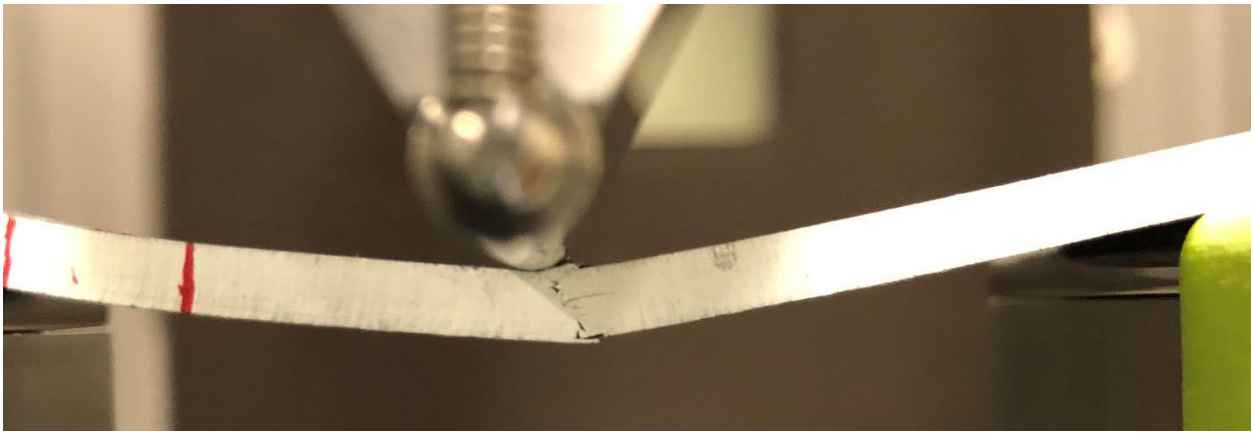

Figure 58. Failing in bending in pre-cracked loading case

The above figure shows failing in bending for the pre-cracked loading case. The pre-cracked loading is when the first non-pre-cracked loading is successful such that the specimen's new crack tip is marked and then loaded in the same manner. For the pre-cracked loading cases, finding the new compliance was successful, but sample 6 failed by bending without crack propagation. Samples 7 through 9 successfully propagated interlaminar cracks.

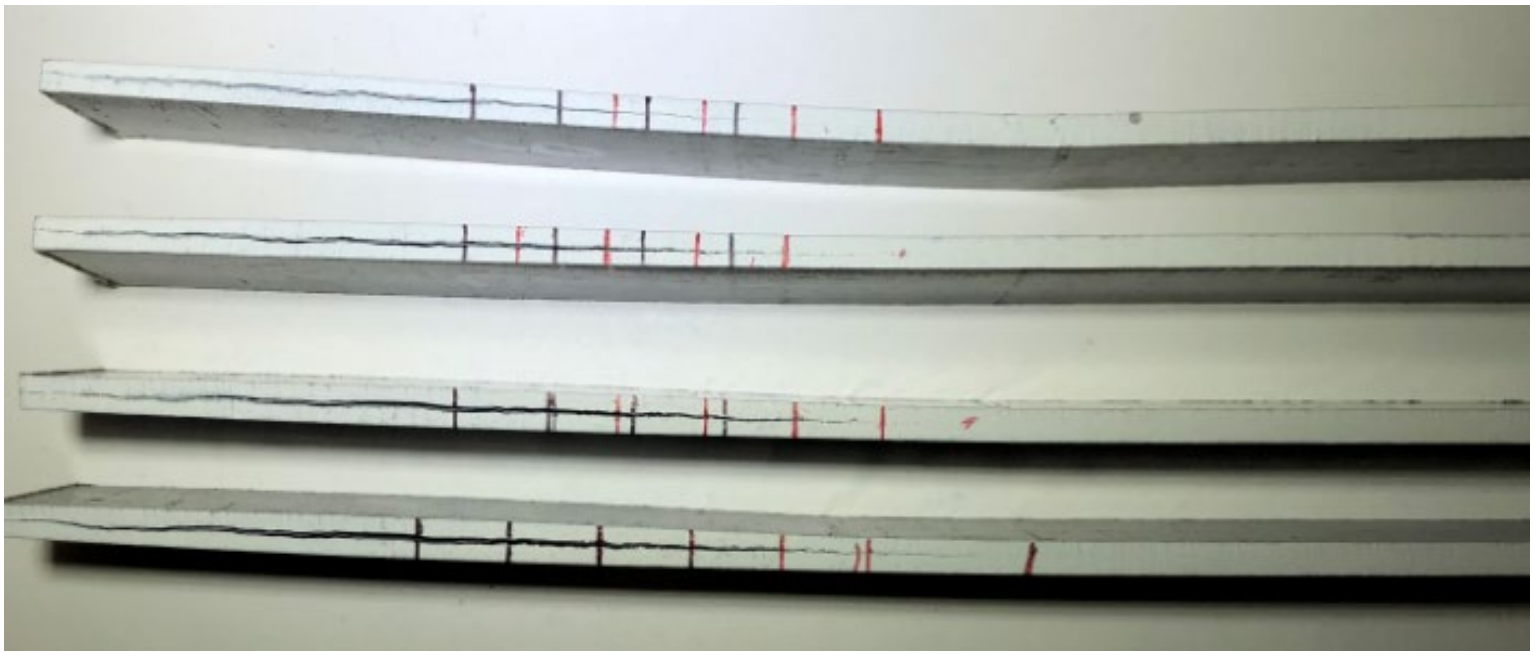

Figure 59. Samples 6 through 9 after testing

The black markings indicate the non-pre-cracked state testing and the 30, 20, 10mm, and the crack tip from the left respectively. Then, since the crack propagated a certain amount, the new crack tip is marked with red line and same 30, 20, 10mm, and the crack tip are marked from the left respectively. After the pre-cracked loading propagated an interlaminar crack, the crack tip was marked in the end.

5.6 Tensile Test [0/45]

5.6.1 Summary

As various tow orientations are being explored in order to meet the control arm strength requirements, the first change of two layup to be tested is 4 plies thick 0-45 tows. There were two plates received named plate 'H' and 'I'. Plate I was cut by waterjet to 1 inch width specimens for simple tensile testing to find modulus and strength. Total of 9 specimens were prepared. Because the tows are aligned in 0 and 45 degrees instead of 0-90 orientation, there is huge warping in the overall plate and the fibers moved significantly while being pressed. The images following shows the plate's condition.

First, two coupons are tested using surfalloy grips without emery cloth. However, failure occurred where the surfalloy grips are gripping, which was unexpected. This could be because of the fiber washing occurring where the tows are far from the center. To prevent this early failure, emery cloth was used. For sample 3, failure occurred near the gripping area again, but from sample 4 through 9, all of the failures occurred around the center, creating consistent results. Figure 55 shows that the tows moved a lot while curing due to the fact that RFF does not 'fix' the fibers together. Compared to samples 4~9, samples 1~3 have not exactly straight 0 degree tows and also experiences lots of plate warping even after cutting the four sides using waterjet cutter.

5.6.2 Dimensions

Sample Number.	**Avg Width** [mm]	**Avg Thickness** [mm]	**Cross sectional Area** $[mm]^2$
1	25.21	0.97	24.45
2	25.16	0.99	24.83
3	25.23	1.00	25.23
4	25.20	1.02	25.79
5	25.22	1.03	26.06
6	25.21	1.02	25.71
7	25.18	1.01	25.52
8	25.19	1.00	25.27
9	25.23	1.00	25.31

Table 19. Dimensions of [0/45] plat specimens from Plate I

5.6.3 Results

Sample ID	**Young's Modulus** [GPa]	**Strength** [MPa]
1	50.29	528.8
2	46.63	396.4
3	47.12	594.6
4	50.84	674.1
5	51.82	631.6
6	51.64	617.8
7	45.23	563.8
8	48.72	559.1
9	44.19	586.4

Table 20. Properties of 0-45 plate

5.6.4 Fractured Images

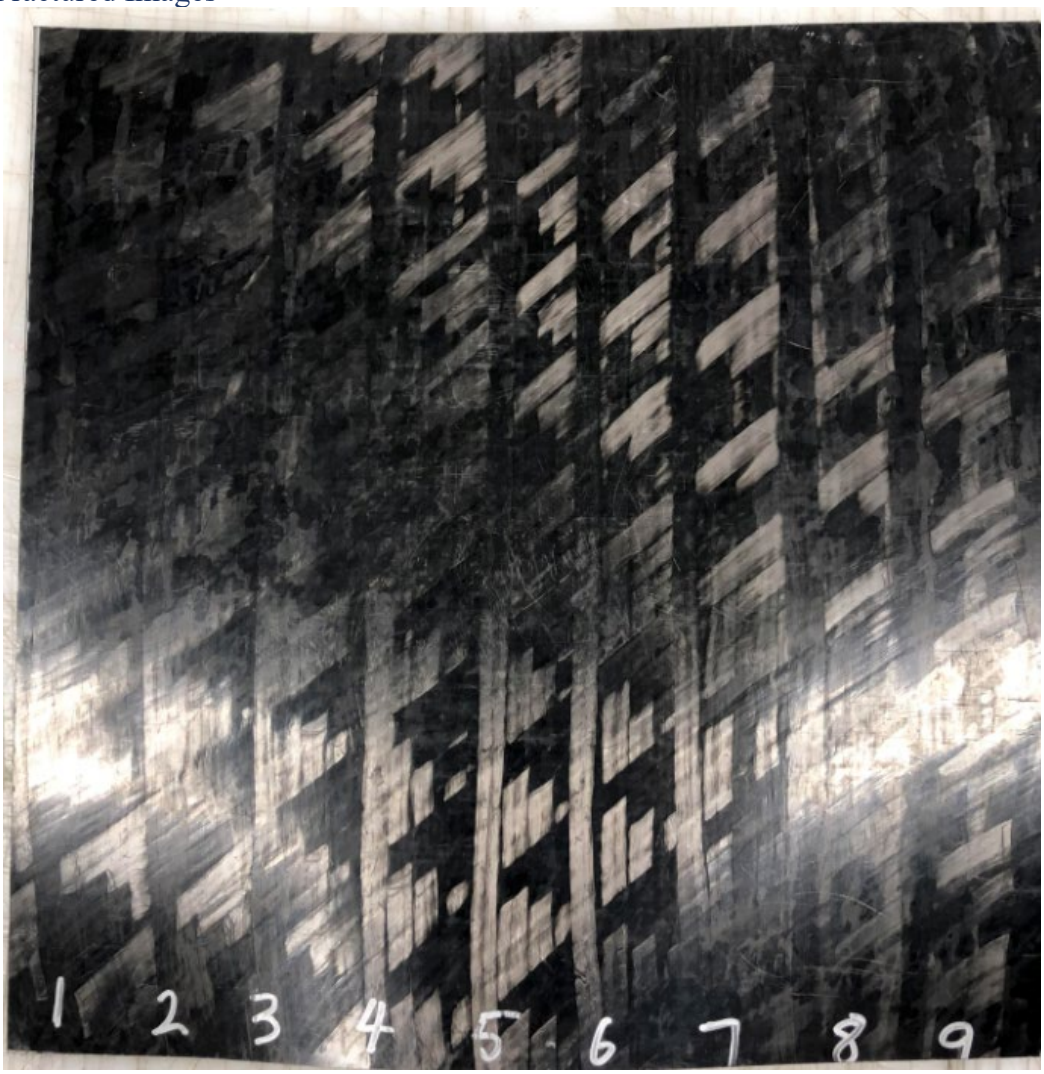

Figure 60. 0-45 plate I. Before Waterjet

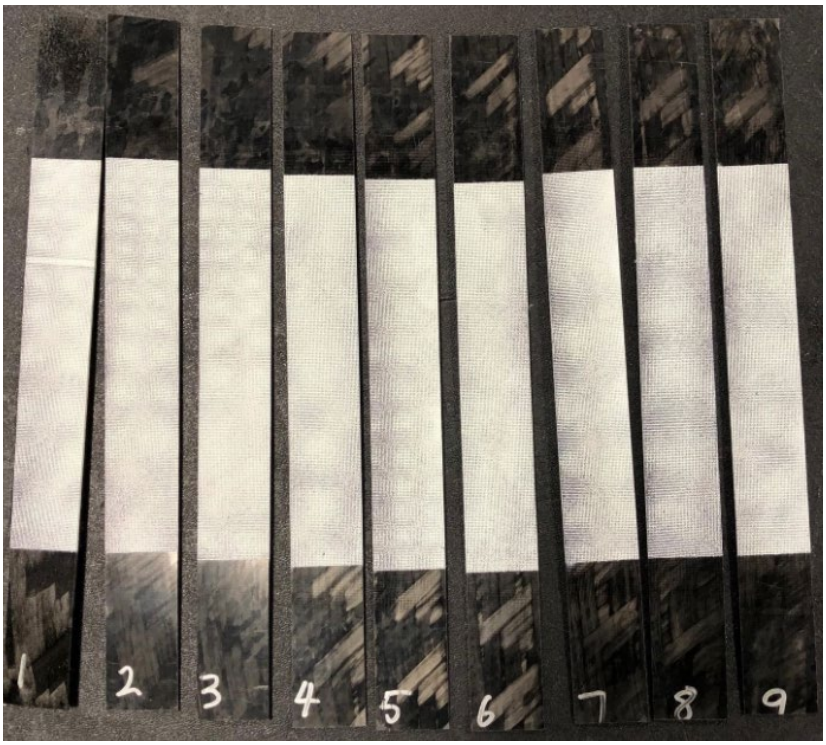

Figure 61. 0-45 plate I. After cut and speckle pattern

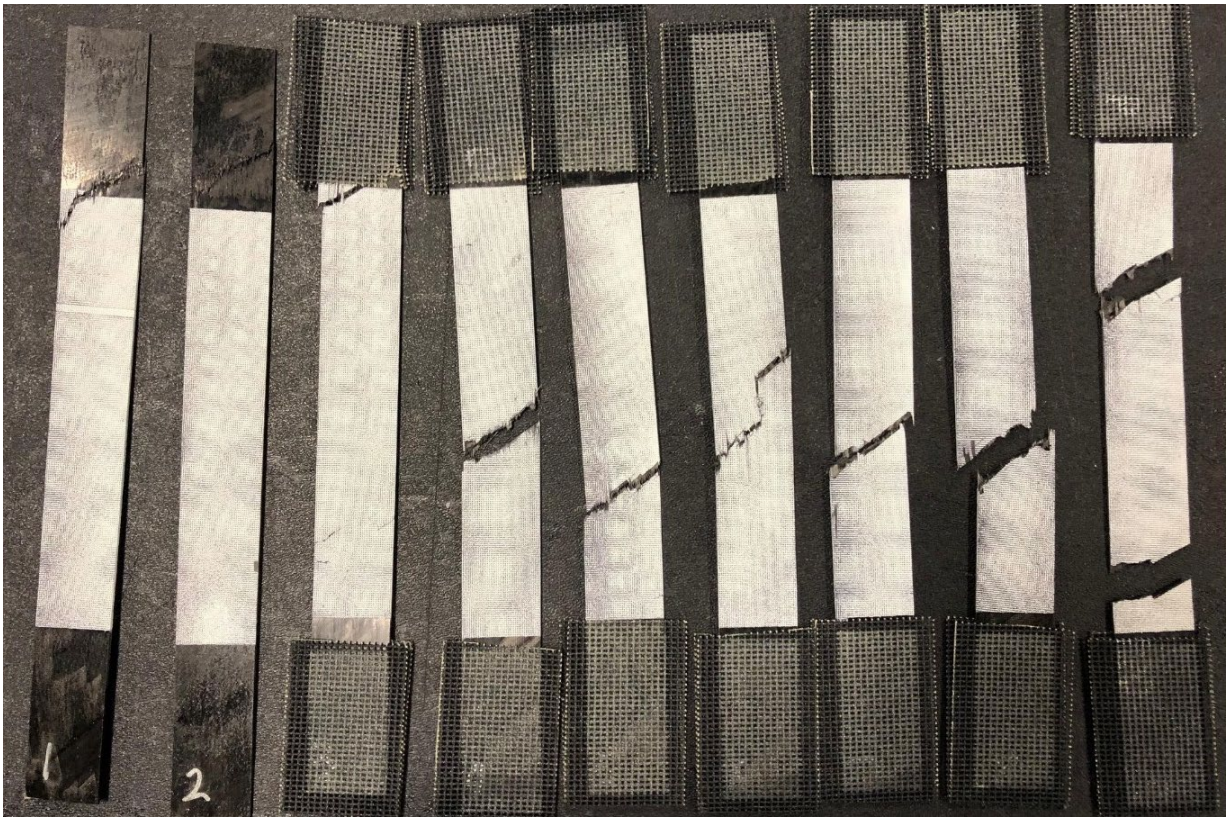

Figure 62. 0-45 Plate I. After fracture

5.7 Shear Modulus using Tows in ±45

5.7.1 Summary

RFF structure was tested using tensile testing to find shear strength and shear modulus. The strain data was collected using DIC analysis to find strain overall instead of at a specific point like strain gauge does.

Loading ramp rate of 2 mm/min was used as the standard says, and the testing went on until fracture. The samples took about 12~ 15 minutes to fracture as the fibers in the tows changed with application of load and was no longer 45 degrees. Also, due to the elongation, the coupons seemed to have necking behavior. It is shown on the following figure.

After the testing, the shear strength and shear moduli are calculated using DIC analysis. Because sample 1, 2, 8, and 9 were too short, only samples from 3 through 7 were able to be tested. The shear modulus and strength results are then post processed.

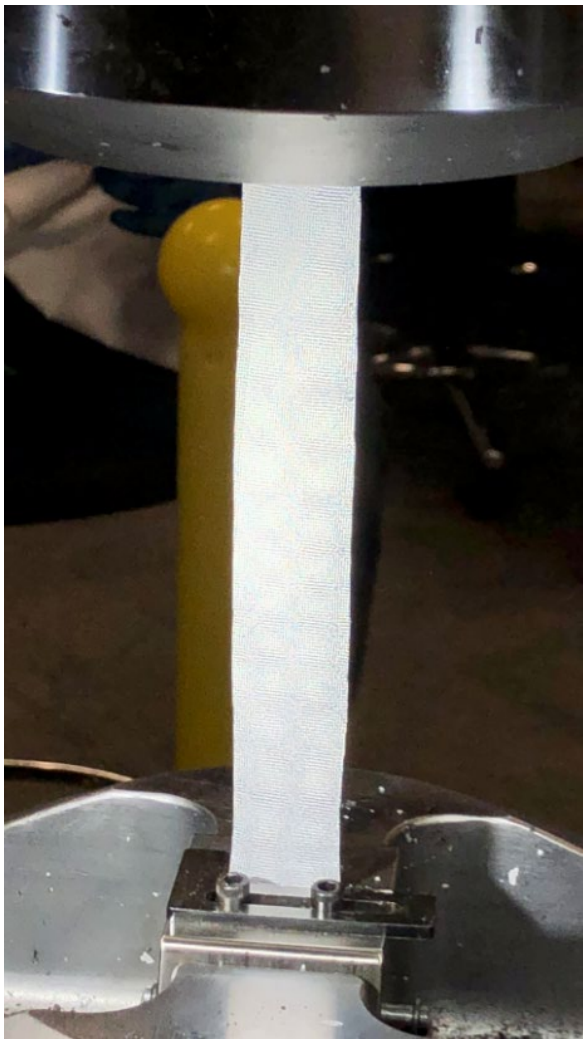

Figure 63. Coupons showing Necking behavior

5.7.2 Dimensions

Sample Number.	**Avg Width** [mm]	**Avg Thickness** [mm]	**Cross sectional Area** $[mm]^2$
1	25.23	1.08	27.16
2	25.21	1.08	27.31
3	25.23	1.12	28.26
4	25.22	1.10	27.83
5	25.24	1.11	27.93
6	25.25	1.12	28.36
7	25.24	1.13	28.52
8	25.27	1.12	28.38
9	25.26	1.12	28.20

Table 21. Dimensions of [45/-45] coupons

5.7.3 Results

Finding the modulus was done by using strain values from 0.002 strain to 0.006 strain as the standard recommended. For shear strength, we used 0.2% offset of the line found to calculate shear modulus from 0 strain point. Then, where the line and original stress strain plot intersects, the strength is recorded. The following figures shows how this process is done. The ultimate strength is the maximum strength before fracture.

Sample ID	**Shear Modulus** [GPa]	**Shear Strength** [MPa]	**Ultimate Strength** [MPa]
3	1.47	20.1	103.6
4	1.41	16.5	104.6
5	1.37	18.5	108.2
6	1.37	18.9	103.0
7	1.28	15.6	95.1

Table 22. Shear Modulus and strength results

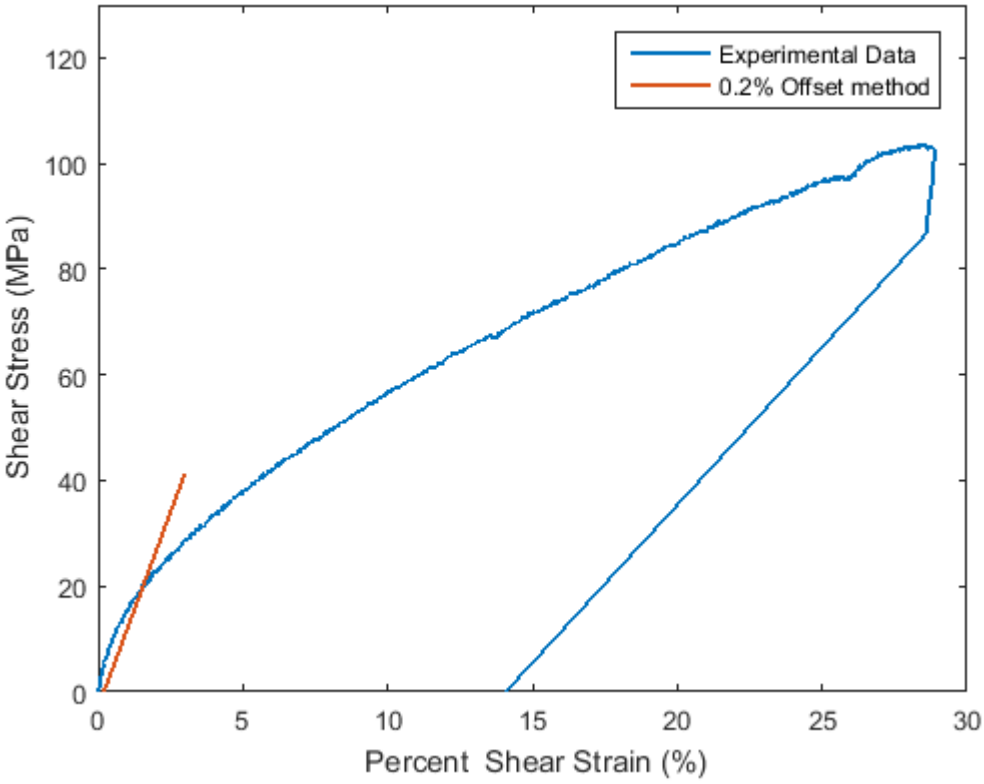

Figure 64. Shear stress vs. shear strain for sample 3

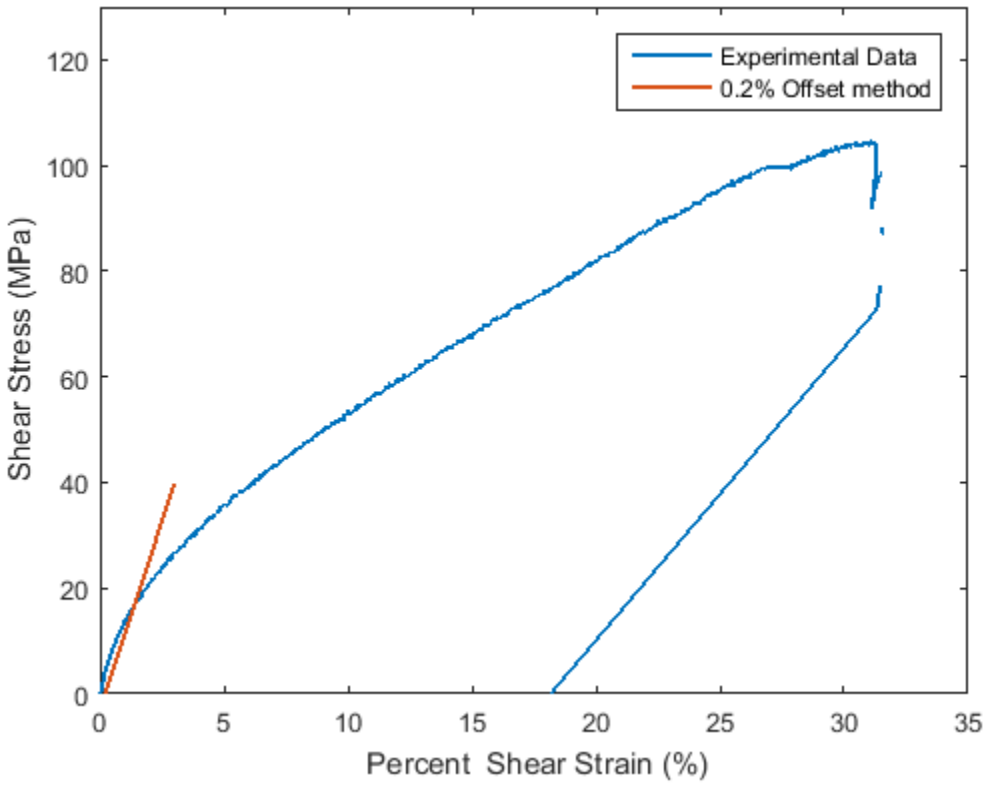

Figure 65. Shear stress vs. shear strain for sample 4

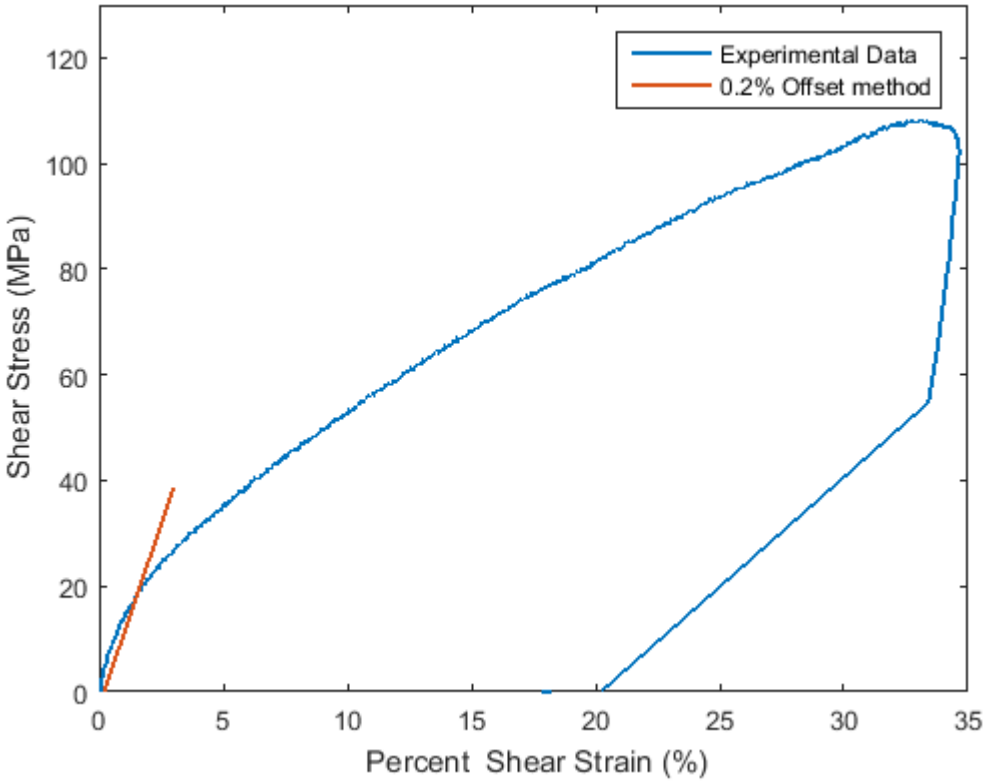

Figure 66. Shear stress vs. shear strain for sample 5

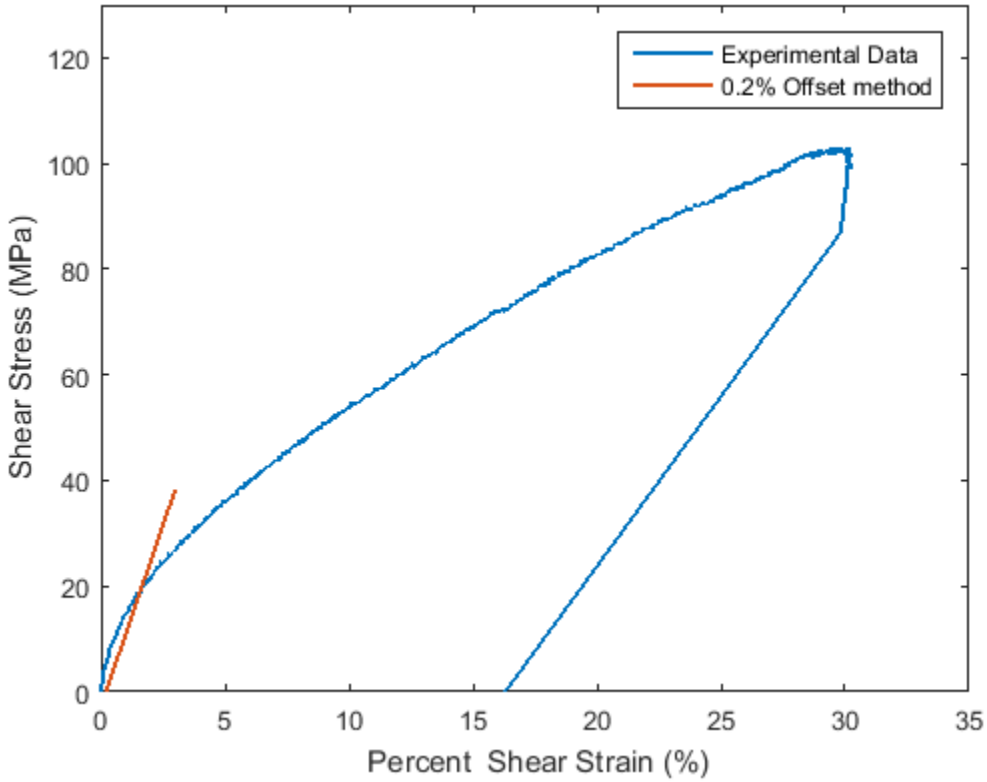

Figure 67. Shear stress vs. shear strain for sample 6

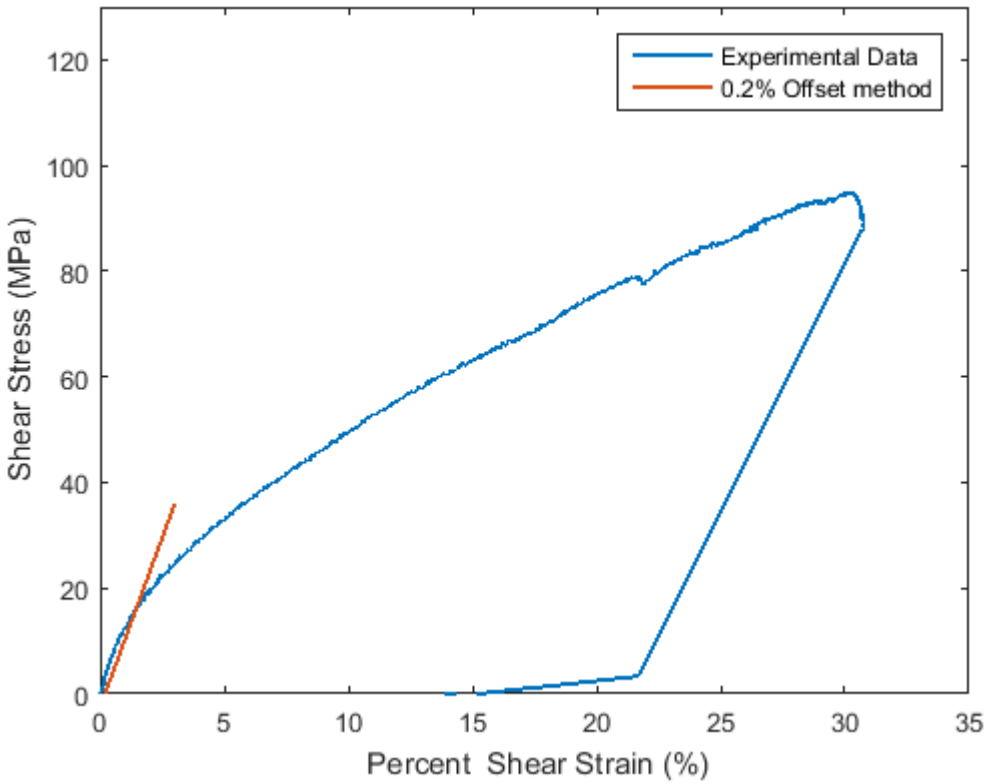

Figure 68. Shear stress vs. shear strain for sample 7

5.7.4 Fractured Images

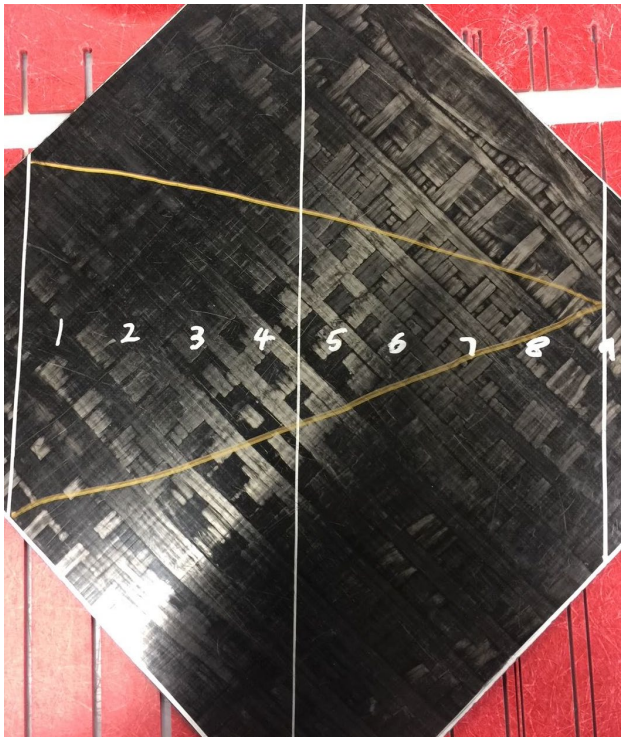

Figure 69. Plate B before waterjet cutting

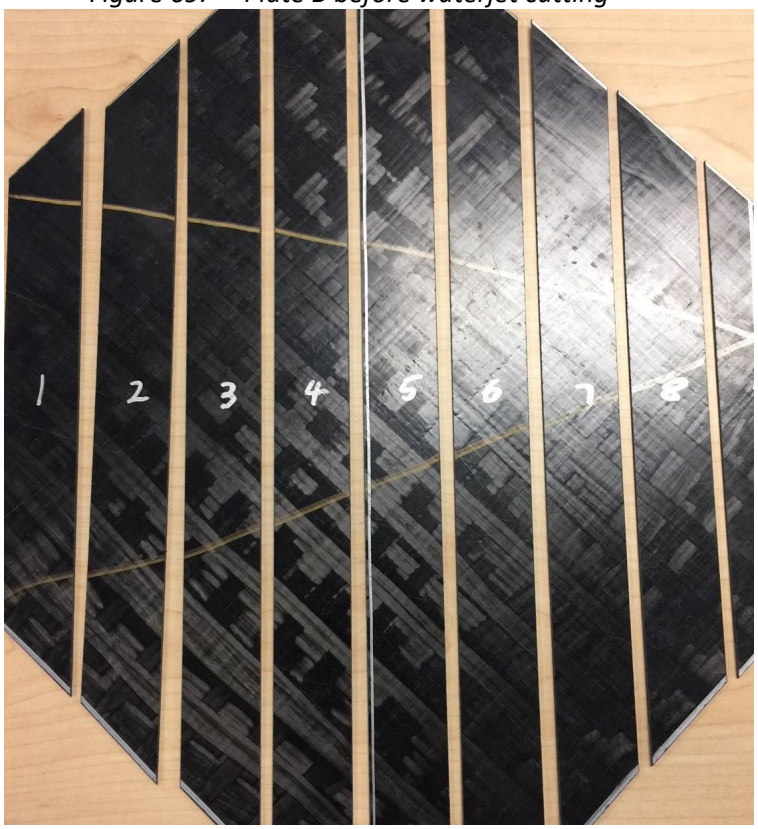

Figure 70. Plate B after waterjet cutting

Figure 71. Sample 4 after fracture

Figure 72. Samples 3, 4, 5, 6, and 7 after testing accordingly

6 DISCUSSION

6.1 Problems Occurred

6.1.1 Adhesive

There were some problems due to the application of the urethane adhesive. The piano hinges and the fiberglass tabs attached to the RFF coupons sometimes failed before the coupons fail, so some changes are made to the testing setup or the adhesive is applied again with more roughened up surfaces with higher grits. Usually the problem was fixed after one new trial. Tab sliding problem was handled by using emery cloth.

6.1.2 Plate Thickness

There were some problems occurring during testing mainly due to the thickness of the sample specimens as well. During DCB testing, the specimens sometimes failed in bending before there is crack propagation, meaning that the specimen's interlaminar property is lower than bending property. The problem can be solved by decreasing the initial crack length by moving the piano hinges closer to the edge of the crack. Also, having a thicker coupon increases bending stiffness such that the interlaminar crack propagation may occur before failing in bending. Another problem of requiring thicker sample occurred when testing compression samples. Because strain gauges had to be used in order to gain strain data, the gauge length had to be larger than the length of the strain gauge. Also, to be able to attach the strain gauges with some gap from the tabs in order to avoid the end effect, the gauge length had to be above 0.5 inch. For thicker samples, 1 inch gauge length was used. Due to long gauge length, the compression samples showed buckling behavior, indicating that the gauge length needs to be decreased or thicker sample is needed. Last problem occurred when testing ENF coupons. Similar to DCB samples, the coupons sometimes failed in bending before crack propagation, so the span length was decreased from 4 inches to 3 inches. At this point, the crack propagation occurred once followed by failing in bending at the top loading pin in the second testing.

6.1.3 Teflon Thickness

The recommended thickness of the Teflon is no more than 30 microns. However, the inserted Teflon's thickness was about 70 microns. This implies that the crack tip may be dull such that interlaminar crack propagation may be difficult.

7 CONCLUSION

Material characterization testing were done on 13 different materials to experimentally determine material properties. During the testing, there were some difficulties when not knowing how the material will behave not only in preparing the specimens but also during the testing. After getting advices from experienced personnel in CMSC, new approaches and solutions were used to find proper method of testing in addition to the standard. Testing with thicker plates of RFF could be considered to reduce problems and to find more consistent result.